Proximity-induced superconductivity in single-layer and bilayer graphene

Zur Erlangung des akademischen Grades eines
DOKTORS DER NATURWISSENSCHAFTEN
durch die Fakultät für Physik
des Karlsruher Institut für Technologie

genehmigte

DISSERTATION

von

MPhys. Julien Bordaz

aus Saint-Vallier, Frankreich

Tag der mündlichen Prüfung:	07.02.2014
Referent:	Prof. Dr. Hilbert von Löhneysen
Korreferent:	Prof. Dr. Wulf Wulfhekel

Abstract

In this work, the properties of proximity-induced superconductivity in graphene and bilayer graphene are investigated. First, we present the study of a junction consisting of a graphene sheet connected with superconducting electrodes spaced by 120 nm. The sample is produced on top a Si/SiO_2 wafer playing the role of a back gate and the low distance between the contacts is achieved by shadow evaporation. The sample is characterised at 50 mK and exhibits a dissipationless current on the whole range of Fermi energy accessed.

We report then the realisation and study of a double-gated bilayer graphene sheet connected with superconducting electrodes. The device is produced on top of a sapphire wafer by using transfer techniques. The bilayer is sandwiched between two atomically flat hexagonal boron nitride sheets used as substrate and gate dielectric. Our measurements at 7 mK show that the induced supercurrent vanishes around the charge neutrality point, while a large product of critical current and normal-state resistance is measured at high charge carrier density. High resistance peaks which cannot be explained by the presence of multiple Andreev reflection are present in the differential resistance, and at any gate voltage. A small magnetic field suppresses those peaks, highlighting an apparent link with the superconductivity. The amplitude of the critical current as well as the normal-state resistance can be tuned by the displacement field induced by the two gates. These measurements show that the bilayer presents a spontaneous asymmetry which can be compensated by the induced displacement field. A finite critical current is then observable even at the charge neutrality point.

Kurzzusammenfassung

Die vorliegende Arbeit befasst sich mit den Eigenschaften von durch den Proximity-Effekt induzierter Supraleitung in ein- und zweilagigem Graphen. Zunächst betrachten wir einen Josephson-Kontakt bestehend aus einer Graphen-Lage, die mit zwei supraleitenden Elektroden im Abstand von 120nm kontaktiert wurde. Die Probe wurde auf einem Si/SiO_2-Wafer hergestellt, der als Backgate verwendet wird, die geringe Entfernung der Kontakte wurde mittels Schattenbedampfung erreicht. Die Probe wurde bei 50mK charakterisiert, sie zeigt über den gesamten betrachteten Bereich der Fermi-Energie verlustfreien Stromfluss.

Wir berichten des Weiteren von der Herstellung und Untersuchung einer Probe mit supraleitenden Elektroden, die aus einer zweilagigen Graphenschicht besteht und mit zwei Gates versehen wurde. Diese Probe wurde unter Nutzung von Transfer-Techniken auf einem Saphir-Wafer hergestellt. Die Graphen-Doppellage wird von zwei atomar glatten Schichten aus hexagonalem Bornitrid eingeschlossen, die als Substrat und Gate-Dielektrika dienen. Unsere Messungen bei 7mK zeigen, dass die induzierte Supraleitung im Bereich der minimalen Ladungsträgerkonzentration verschwindet, während das Produkt aus kritischer Stromstärke und Widerstand im normalleitenden Zustand in den Bereichen hoher Ladungsträgerkonzentration große Werte annimmt. Der differentielle

Widerstand weist Peaks auf, die sich nicht durch vielfache Andreev-Reflexion erklären lassen, und das bei jeder Gate-Spannung. Das Anlegen eines schwachen Magnetfeldes unterdrückt diese Peaks, was auf eine Verbindung zur Supraleitung hinweist. Die Amplitude der kritischen Stromstärke, sowie der Widerstand im normalleitenden Zustand können mit den zwei Gates durch das Anlegen eines Verschiebungsfeldes variiert werden. Diese Messungen zeigen, dass die Graphen-Doppellage eine spontane Asymmetrie aufweist, die durch das Verschiebungsfeld kompensiert werden kann. In diesem Fall lässt sich selbst am Punkt der Ladungsträgerneutralität eine endliche kritische Stromstärke beobachten.

Contents

Introduction

Carbon is the sixth atom of the periodic table. With its valency, is can form several allotropes such as diamond and graphite, that have been known for centuries. In more recent decades, carbon nanotubes and fullerene molecules were synthesized, adding respectively zero-dimensional and one-dimensional materials to the carbon allotropes family. For their stability, their low dimensionality and their ability to carry a large current, those materials raised a large interest in the scientific community. Until recently, the two-dimensional carbon allotrope named graphene was still missing. The fundamental properties of this one-atomic-thick material were already investigated though. In 1947, graphene was used by P. Wallace as a starting point to study the electronic properties of graphite.

It was only in 2005 that graphene had been isolated by A. Geim and K. Novoselov from Manchester University. The interest for this material rose immediately in the scientific community, as graphene presents some spectacular properties. Among them, at low energy the charge carriers can be described with an equation formally analogous to the Dirac one and thus behave like relativistic massless Dirac fermions. Graphene is so far the only material in which this can be observed. In addition to its novel physical properties, graphene is a candidate of choice for potential electronic applications due to the large carrier mean free paths and mobilities observed in this material. In addition, the charge carrier density is easily tunable by the field effect.

A more specific domain of interest concerns the physical effects occurring when graphene is connected to a superconductor. When a non-superconducting material is connected to closely spaced superconducting electrodes (on a submicron scale), it can carry a dissipationless current as if it was superconducting itself. A large amount of work both theoretical and experimental has already been done on such junctions with graphene as the non-superconducting material. Unlike similar junctions using metals, the possibility to tune the charge carrier density gives a direct control of the maximum supercurrent (or critical current) that can flow through the device. The usual electron-to-hole conversion process named Andreev reflection occurring in metal-superconductor interfaces shows important differences as well. A new spectacular effect, the specular Andreev reflection, has been theoretically predicted in graphene-superconductor interfaces.

So far, proximity-induced superconductivity in bilayer graphene (the material consisting of two layers of graphene) raised much less interest. A large part of this thesis focuses on this topic. At first sight, no significantly different properties from the monolayer case are expected. A particularity of bilayer graphene is the possibility to open a gap in its band structure by breaking the symmetry between the two layers. This is usually achieved experimentally by sandwiching the bilayer between two gates. In a dual-gated bilayer graphene sheet connected with close superconducting electrodes, it should be then theoretically possible to observe a transition from a superconducting state to a resistive and, finally, insulating state.

Outline of this thesis

The basic properties of graphene (monolayer and bilayer) are presented in chapter 1. Chapter 2 focuses on the theory behind the proximity induced superconductivity, in the general case and more specifically with graphene as the non-superconducting material.

The experimental part starts with the description of the sample preparation techniques in chapter 3. The standard ways to isolate, identify and connect graphene sheets are detailed. We focus especially on the transfer process, that opened the way to the design of the so-called van der Waals heterostructures. This technique is employed here to produce dual-gated samples using hexagonal boron nitride as an atomically flat substrate. Chapter 4 details the measurement setups used. A particular attention is given to the home-made filtering devices that are necessary to perform measurements at cryogenic temperatures.

Chapter 5 presents a first measurement performed on a superconductor-graphene-superconductor junction. The sample has been designed to be as short as possible and on silicon dioxide. The possibility to reach the ballistic regime in such a junction is discussed. Chapter 6 details the study of a dual-gated bilayer graphene sheet, connected with superconducting electrodes. The device is built on top of a sapphire wafer and two hexagonal boron nitride sheets play the role of substrate and gate dielectrics. With the two gates, both the Fermi energy and the displacement field in the bilayer graphene can be tuned. The device combines then the possibility to observe an induced supercurrent and the ability to open a gap in the band structure of the bilayer graphene.

Chapter 1

Introduction to graphene

Here we present a short introduction to the basic properties of graphene. This chapter is divided in two parts, a first one based on monolayer followed by a second part on bilayer graphene, with a focus on the possibility to open a gap.

1.1 Monolayer graphene

1.1.1 Crystallographic structure

Graphene is a two dimensional (2D) crystal made of carbon atoms in hexagonal lattice. It was isolated for the first time in 2004 by the Manchester Group led by K. S. Novoselov and A. K. Geim, opening the way to a large amount of theoretical and experimental work on this material [1, 2, 3, 4]. Detailed reviews of graphene's basic properties can be found in references [5] or [6].

Graphene is the elementary sheet composing graphite, which can be itself considered as a stack of graphene sheets linked by van der Waals force. The distance between two carbon atoms is $a = 1.42$ Å. Each atom is bound to its three nearest neighbours by a covalent sp^2 bond. The primitive cell of graphene is composed of two atoms, A and B, and the complete lattice can be built with the two fundamental vectors $\vec{a_1}$ and $\vec{a_2}$:

$$\vec{a_1} = \frac{a}{2}(3, \sqrt{3}), \vec{a_2} = \frac{a}{2}(3, -\sqrt{3}) \tag{1.1}$$

The nearest-neighbour vectors are:

$$\vec{\delta_1} = \frac{a}{2}(1, \sqrt{3}), \vec{\delta_2} = \frac{a}{2}(1, -\sqrt{3}), \vec{\delta_3} = -a(1, 0) \tag{1.2}$$

The construction of the complete graphene lattice leads to the generation of two sublattices, each corresponding to one of the initial atoms. Those sublattices will be referred to as A and B later (figure 1.1a). It is not possible to reach an atom of the B lattice from an atom from the A lattice by using the $\vec{a_1}$ and $\vec{a_2}$ vectors (and reciprocally).

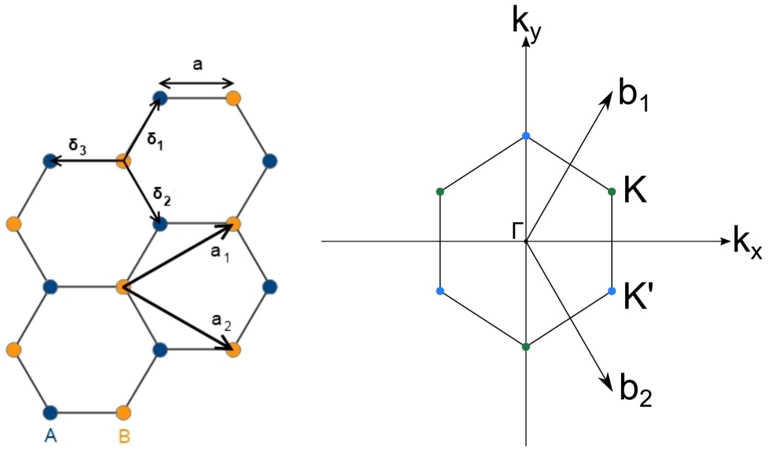

(a) (b)

Figure 1.1: (a) Atomic lattice of graphene. The lattice vectors $\vec{a_1}$, $\vec{a_2}$, the nearest neighbor vectors and the two sub-lattices formed by the A and B atoms are highlighted. (b) First Brillouin Zone of graphene, with the reciprocal lattice vectors $\vec{b_1}$, $\vec{b_2}$ and the points Γ, K, K'.

1.1.2 Reciprocal lattice

The two fundamental vectors generating the reciprocal lattice of graphene can be calculated from the real space ones:

$$\vec{b_1} = \frac{2\pi}{3a}(1, \sqrt{3}), \vec{b_2} = \frac{2\pi}{3a}(1, -\sqrt{3}) \tag{1.3}$$

The graphene reciprocal lattice forms a honeycomb structure as well, rotated by 90° with respect to the real-space structure (figure 1.1b). The first Brillouin zone has a hexagonal structure and two inequivalent types of corner points: K and K'. Their coordinates are:

$$K(\frac{2\pi}{3a}, \frac{2\pi}{3\sqrt{3}a}), K'(\frac{2\pi}{3a}, -\frac{2\pi}{3\sqrt{3}a}) \tag{1.4}$$

Every point of the reciprocal lattice can be reached from those points and with the $\vec{b_1}$ and $\vec{b_2}$ lattice vectors, but no K point can be reached from a K' and reciprocally (analogously to the atoms A and B in the real space). The point Γ is defined as the center of the first Brillouin zone.

1.1.3 Band structure

The graphene band structure has been calculated for the first time by P.R. Wallace in 1947 [7]. To find the electronic states $|\Psi\rangle$ and the corresponding energies $E_{\vec{k}}$ of a system, one has to solve the Schrödinger equation:

$$H\,|\Psi\rangle = E_{\vec{k}}\,|\Psi\rangle \tag{1.5}$$

With H the Hamiltonian of the system. Graphene being a periodic crystal, Bloch's theorem is satisfied (with $\vec{r'} = n\vec{a_1} + m\vec{a_2}$, n and m being integers):

$$\Psi(\vec{r} + \vec{r'}) = e^{i\vec{k}.\vec{r'}}\Psi(\vec{r}) \tag{1.6}$$

The graphene Hamiltonian has been determined in the tight-binding approximation, and by considering that the electrons can hop to the nearest and next-nearest neighbour atoms. The resulting H is then [5]:

$$H = -t\sum_{i,j,\sigma}(a^{+}_{\sigma,i}b_{\sigma,j} + Hc.) - t'\sum_{i,j,\sigma}(a^{+}_{\sigma,i}a_{\sigma,j} + b^{+}_{\sigma,i}b_{\sigma,j} + Hc.) \tag{1.7}$$

$a^{+}_{\sigma,i}$, $a_{\sigma,i}$, $b^{+}_{\sigma,i}$, $b_{\sigma,i}$ are respectively the creation and annihilation operator of an electron at site R_i with spin σ, on the sub-lattice A or B. Hc is the hermitian conjugation of the precedent terms. t, t' are respectively the hopping energies in the other sublattice (corresponding to the nearest neighbors) and in the same sublattice (corresponding to the next-nearest neightbors). Their values determined by *ab initio* calculations are $t \simeq 2.8eV$ and $t' \simeq 0.1$ eV [5].

Solving this Hamiltonian leads to the energy dispersion relation for a wave vector $\vec{k}(k_x, k_y)$ [5]:

$$E(\vec{k}) = \pm t\sqrt{3 + f(\vec{k})} - t'f(\vec{k}) \tag{1.8}$$

with $\vec{k}$ inside the Brillouin zone and

$$f(\vec{k}) = 2\cos(\sqrt{3}k_y a) + 4\cos(\frac{\sqrt{3}}{2}k_y a)\cos(\frac{3}{2}k_x a) \tag{1.9}$$

Figure 1.2 represents the calculated band structure. We notice that the resulting upper (π^*) and lower bands (π) touch each other at the K and K' points located at each corner of the Brillouin zone, where the energy is zero. Because the density of states cancels at these points, graphene can be considered as a semi-metal. Undoped graphene having the unusual band structure of a filled valence band, an empty conduction band and no gap between the two, it can be considered as a gapless semiconductor too.

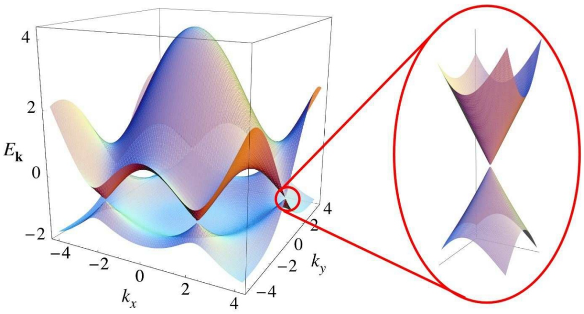

Figure 1.2: Band structure of graphene, with a zoom at one of the Dirac point. The absence of gap between the conduction and valence bands and the linear dependence of the energy relatively to the $\vec{k}$ vector can be observed. Adapted from [5].

The conic structures around the two inequivalent K and K' points are called the valleys. An electron of low energy (-1 eV $< E_F <$ +1 eV) will belong to one of the two.

The valley label is often called isospin. It must not be confused with the real electron spin.

Around the K (or K') point, it is possible to simplify the dispersion relation by introducing the vector $\vec{\delta k}$ defined by $\vec{k} = \Gamma\vec{K} + \vec{\delta k}$. We have then $E(\vec{k}) = E(\Gamma\vec{K}) + \delta E(\vec{\delta k}) = \delta E(\vec{\delta k})$. If $\vec{\delta k}$ is small enough the energy dispersion becomes isotropic and linear instead of quadratic as in most crystals:

$$E(\vec{k}) = E(\vec{\delta k}) \approx \pm\hbar v_F|\vec{\delta k}| \tag{1.10}$$

With $\vec{k}$ around the Dirac point and v_F the Fermi velocity ($v_F = 3ta/2\hbar \simeq 10^6$ m.s^{-1}). This linearity is one of the most important properties of graphene. Linear energy dispersions are a property of relativistic massless particles. Around the K and K' points, charge carriers in graphene behave formally thus like massless relativistic Dirac fermions moving in two dimensions with the Fermi velocity v_F. This property has been demonstrated first by Semenoff [8]. The K and K' points are therefore called the Dirac points, and from now on $\vec{k}$ will refer to the vector $\vec{\delta k}$ defined from these points. At low energy around the K point the charge carriers can be described by the Dirac Hamiltonian:

$$H_K = \hbar v_F \begin{pmatrix} \Delta & k_x - ik_y \\ k_x + ik_y & \Delta \end{pmatrix} \tag{1.11}$$

with Δ the difference in on-site potential for the sublattices. If $\Delta = 0$, then:

$$H_K = \hbar v_F \vec{\sigma}.\vec{k} \qquad H_{K'} = \hbar v_F \vec{\sigma^*}.\vec{k} \tag{1.12}$$

with $\vec{\sigma} = (\sigma_x, \sigma_y)$ the vector of Pauli matrices. These effective Hamiltonians lead to two-component wavefunctions for each valley:

$$\psi_{\pm,K}(\vec{k}) = \frac{1}{\sqrt{2}}\begin{pmatrix} e^{-i\theta_{\vec{k}}/2} \\ \pm e^{i\theta_{\vec{k}}/2} \end{pmatrix}, \psi_{\pm,K'}(\vec{k}) = \frac{1}{\sqrt{2}}\begin{pmatrix} e^{i\theta_{\vec{k}}/2} \\ \pm e^{-i\theta_{\vec{k}}/2} \end{pmatrix} \tag{1.13}$$

with $\theta_{\vec{k}} = \arctan(k_x/k_y)$ and ± corresponding to the energies $E(\vec{k}) = \pm\hbar v_F|\vec{k}|$. The two components describe the repartition of the wavefunction over the two sublattices A and B of the graphene sheet. The wavefunctions share the properties of a two-component spinor (as a 2π rotation of θ around a K point changes their sign) and are therefore called pseudospinors. $\psi_{\pm,K'}(\vec{k})$ and $\psi_{\pm,K'}(\vec{k})$ are eigenfunctions of the chirality operator defined by the projection of the pseudospin on the wavevector:

$$\hat{h} = \vec{\sigma}.\frac{\vec{k}}{||\vec{k}||} \tag{1.14}$$

The two eigenvalues of $\hat{h}$ are ±1, depending on the alignment of the pseudospin with the $\vec{k}$ vector. Around the K and K' points electrons and holes have then a well-defined chirality, as these values are good quantum numbers as long as the effective Hamiltonien 1.12 is valid. The analogy with the Dirac equation is now complete: the Fermi velocity replaces the speed of light and the pseudospin plays the role of the real spin.

The density of states $D(E)$ can be derived from equation 1.8. By neglecting the hopping energy term t', the density of states is proportional to the energy too and is given around the Dirac point by the equation:

$$D(E) = \frac{2}{\pi}\frac{|E|}{\hbar^2 v_F^2} \tag{1.15}$$

1.1.4 Electronic transport

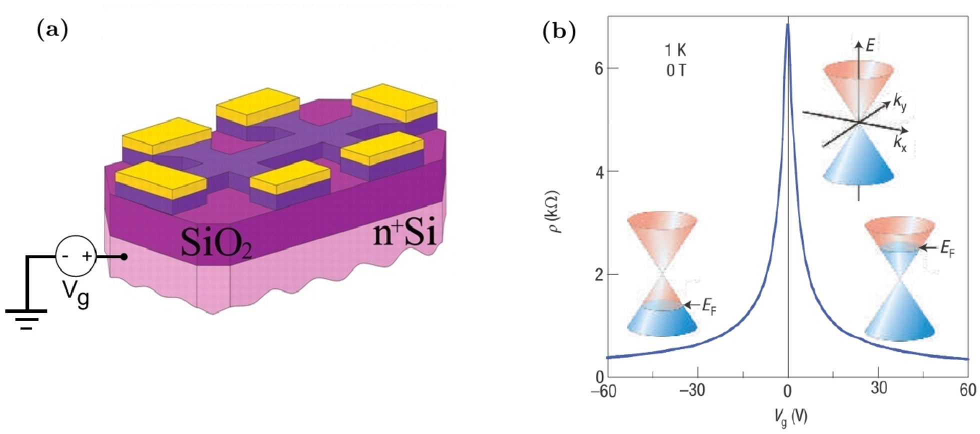

Figure 1.3: (a) Graphene Hall-bar structure on a Si/SiO$_2$ substrate. Changing the gate voltage tunes the Fermi level position in the band structure and the charge carrier density in the graphene sheet. The resistance of the sample can be measured through the electrodes. Adapted from [1] (b) Resistance versus gate voltage sweep for a graphene sheet, adapted from [4]. On the left side of the maximum resistance the charge carriers are holes, and on the right side the current is carried by electrons. A maximum finite resistance is observed at the Dirac point.

The transport properties of mesoscopic structures can be described in a rough first approximation by the classical Drude model. In this model, electrons are considered as free classical particles moving in a lattice of fixed ions. The electron-electron interactions are neglected and all interactions with the lattice are described by the mean scattering time τ between two elastic scattering processes. In the absence of an electric field, the average velocity of the electrons is zero. When an external field $\vec{E}$ is applied, the mean electrons velocity reaches the limit value $\langle\vec{v}\rangle = -e\vec{E}\tau/m_e$. The average current density is then $\langle\vec{j}\rangle = -ne\langle\vec{v}\rangle$. We get then:

$$\langle\vec{j}\rangle = \sigma\langle\vec{E}\rangle \tag{1.16}$$

with the conductivity σ expressed by:

$$\sigma = \frac{ne^2\tau}{m_e} \tag{1.17}$$

It is possible to introduce the mobility defined by $\mu = \frac{e\tau}{m_e}$. We have then:

$$\langle \vec{j} \rangle = en\mu \langle \vec{E} \rangle \tag{1.18}$$

The relation between the conductivity and the mobility is: $\mu = \sigma / en$.

To take into account the scattering processes in a more accurate way, the electronic transport in graphene can be described with the Boltzmann model. In the presence of a weak electric field and randomly distributed Coulomb impurity charges, the conductivity reads [9]:

$$\sigma = \frac{e^2}{2} \int dE D(E) v^2 \tau(E) \left(-\frac{\partial f}{\partial E} \right) \tag{1.19}$$

with f the Fermi distribution at equilibrium, $D(E)$ the density of states, v the velocity of the carrier and $\tau(E)$ the scattering time (which is dependent of the energy in this model). At $T = 0$, f is a step function at $E = E_F$ so the expression can be simplified:

$$\sigma = \frac{e^2 v_F^2}{2} D(E_F) \tau(E_F) \tag{1.20}$$

The scattering time is given by:

$$\frac{1}{\tau(\epsilon_{\vec{k}})} = \frac{2\pi}{\hbar} \sum_a \int dz n_i^{(a)}(z) \int \frac{d^2 k'}{(2\pi)^2} |\langle V_{\vec{k},\vec{k}'}(z) \rangle|^2 (1 - cos\theta_{\vec{k},\vec{k}'}) \delta(\epsilon_{\vec{k}} - \epsilon_{\vec{k}'}) \tag{1.21}$$

with $n_i^{(a)}(z)$ the concentration of each impurity type, $\theta_{kk'}$ the scattering angle and $|\langle V_{\vec{k},\vec{k}'}(z) \rangle|^2$ the scattering potential. Calculating τ for randomly distributed charged centers leads to a $\tau \propto \sqrt{n}$ dependency at high charge carrier density [10]. In addition to the density of state proportional to $\sqrt{n}$ as well, this leads to $\sigma \propto n$.

In graphene, the charge carrier density n and the Fermi energy can be tuned by the field effect. This can be achieved in practice by designing a gate under (or on top of) the graphene sheet. By applying a potential difference between this gate and the sample, charges are attracted to or repelled from the graphene sheet thanks to the electrodes playing the role of charge reservoirs (figures 1.3a).

If we consider the standard case of a graphene sheet deposited on top of a silicon dioxide (with d the oxide thickness and ϵ_r its relative permeability), the charge carrier concentration is $n = \alpha V_g$, with $\alpha = \frac{1}{e}\frac{\epsilon_0 \epsilon_r}{d}$. In practice, due to the presence of a residual doping the Dirac point is usually not located at exactly $V_g = 0$. We have to use then $V_g' = V_g - V_D$, with V_D the gate voltage corresponding to the position of the Dirac point. The additional doping can come from the adsorption of molecules on top of the graphene sheet, from interaction with the substrate or from the contacts themselves.

When the Fermi level is above the Dirac point ($V_g' > 0$), the charge carriers are electrons (and holes when below). Moving the Fermi level away from the Dirac point increases the carrier concentration and reduces the resistivity.

At the Dirac point, even though the charge carrier density is theoretically zero, the resistivity does not diverge (figures 1.3b). This result cannot be explained with the classical Drude model. Theoretical predictions taking in account the properties of Dirac fermions in 2D systems show that electronic transport can still occur through evanescent waves. When the Fermi level is located at the Dirac point a minimum conductivity of $\frac{4e^2}{\pi h}$ is expected [11, 12, 13]. Experimentally, minimum conductivities of $\frac{4e^2}{h}$ are reported on relatively large sample [2]. This topic is still under debate.

1.2 Bilayer graphene

1.2.1 Crystallographic structure

Bilayer graphene consists of two layers of graphene. The two main stackings are the A-B and the A-A one. An infinite number of stackings can actually exist as one of the layers can be twisted by a certain angle relatively to the other. Because the A-B stacking (figure 1.4a) is energetically favourable, the other ones occur rarely and will not be considered in this thesis.

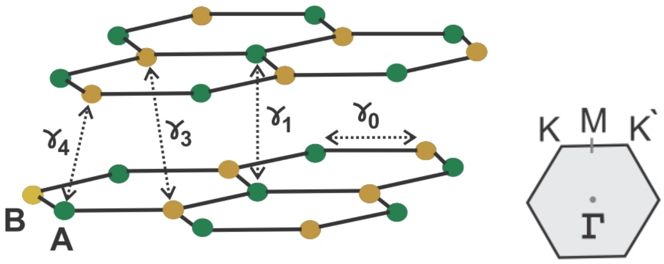

(a) (b)

Figure 1.4: (a) Lattice structure of a bilayer graphene sheet. As in the monolayer case each layer has its own two sub-lattices. The different hopping energies γ_i between neighbours atoms are represented. (b) First Brillouin zone of bilayer graphene. Adapted from [5]

1.2.2 Band structure

The tight-binding model leads to the Hamiltonian [5]:

$$\begin{aligned} H = -\gamma_0 \sum_{<i,j>,m,\sigma} (a^{+}_{\sigma,m,i} b_{\sigma,m,j} + Hc.) - \gamma_1 \sum_{j,\sigma} (a^{+}_{\sigma,1,j} a_{\sigma,2,j} + Hc.) \\ -\gamma_3 \sum_{j,\sigma} (a^{+}_{\sigma,1,j} b_{\sigma,2,j} + a^{+}_{\sigma,2,j} b_{\sigma,1,j} + Hc.) - \gamma_4 \sum_{j,\sigma} (b^{+}_{\sigma,1,j} b_{\sigma,2,j} + Hc.) \end{aligned} \tag{1.22}$$

where $a^{+}_{\sigma,m,i}$, $a_{\sigma,m,i}$, $b^{+}_{\sigma,m,i}$, $b_{\sigma,m,i}$ are respectively the creation and annihilation operator of an electron on site R_i with spin σ, on the sublattice A or B, on the layer m (m =1 or 2 for the bilayer), and γ_i are the different hopping parameters between the carbon atoms (see figure 1.4a).

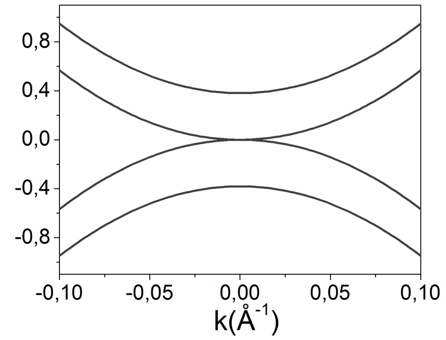

Figure 1.5: Band structure of bilayer graphene in the low-energy limit (γ_3 and γ_4 neglected) and without any potential difference between the two layers. As in monolayer graphene there is no gap between the conductance and valence bands.

Like in the monolayer case, the band structure of bilayer graphene consists of two valence and conduction bands touching each other on two inequivalent points K and K' in the first Brillouin zone. The Hamiltonian can be simplified in the valleys around these points. In the low-energy limit, it is possible to consider only the in-plane nearest-neighbour coupling γ_0, and the interlayer coupling γ_1. γ_3 and γ_4 are neglected. The Hamiltonian operates on $\Psi = (\psi_{A1}, \psi_{B2}, \psi_{A2}, \psi_{B1})$ for the valley at K, and on $\Psi = (\psi_{B2}, \psi_{A1}, \psi_{B1}, \psi_{A2})$ for that at K' [14]:

$$H = \pm \begin{pmatrix} -V & 0 & 0 & v(k_x - ik_y) \\ 0 & V & v(k_x + ik_y) & 0 \\ 0 & v(k_x - ik_y) & V & \pm\gamma_1 \\ v(k_x + ik_y) & 0 & \pm\gamma_1 & -V \end{pmatrix} \tag{1.23}$$

Here $v = 3\gamma_0 a/2\hbar$ (the in-plane velocity in bilayer graphene is the Fermi velocity in monolayer graphene) and V is half of the chemical potential difference between the two layers. The ± sign depends on the valley considered (+ for the K-valley, − for the K').

Let us consider first the $V = 0$ case. The effective Hamiltonian for the K valley (acting on the spinor (ψ_{B1}, ψ_{A2})) can be simplified to:

$$H_K = \begin{pmatrix} 0 & -\frac{\hbar^2}{2m^*}(k_x - ik_y)^2 \\ -\frac{\hbar^2}{2m^*}(k_x + ik_y)^2 & 0 \end{pmatrix} \tag{1.24}$$

with $m^* = \gamma_1/2v^2$. This effective Hamiltonian leads to two parabolic bands (unlike the linear bands in the case of a monolayer graphene sheet), following the dispersion relation:

$$E(\vec{k})_\pm = \pm\frac{\hbar^2\vec{k}^2}{2m^*} \tag{1.25}$$

The electrons behave then like massive chiral particles [5]. The electron-hole symmetry is preserved. Two additional bands with a coupling energy γ_1 are present. Figure 1.5 shows the calculated band structure in this low-energy limit. Unlike the monolayer case, the Fermi velocity depends on $\vec{k}$ with $v_F = \hbar k_F/m^*$, and the density of states $D = m^*/2\pi\hbar^2$ per valley and spin is constant.

1.2.3 Gap opening

If $V \neq 0$ the energy dispersion relation becomes:

$$E^2(\vec{k}) = V^2 + \hbar^2 v^2 \vec{k}^2 + \frac{\gamma_1^2}{2} \pm \sqrt{4V^2\hbar^2 v^2 \vec{k}^2 + \gamma_1^2 \hbar^2 v^2 \vec{k}^2 + \frac{\gamma_1^4}{4}} \tag{1.26}$$

For small momentum and $V \ll \gamma_0$, the relation is simplified to:

$$E(\vec{k}) \simeq V - (2V\hbar^2 v^2 \vec{k}^2)/\gamma_1 + (\hbar^4 v^4 \vec{k}^4)/(2\gamma_1^2 V) \tag{1.27}$$

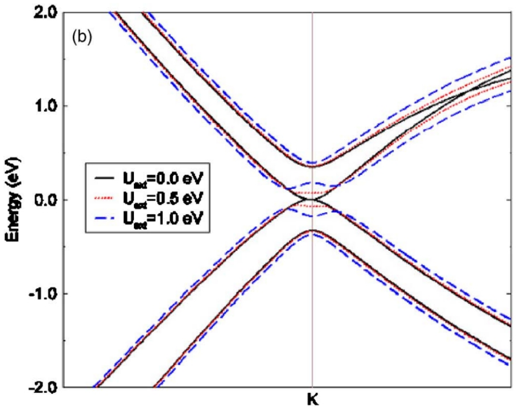

Figure 1.6: Band structure of bilayer graphene with the presence of an induced gap. The band-structure for three different potential difference between the two layers are represented. The band-structure shape for the higher one is sometime referred to as the "Mexican hat" one. Taken from [15]

Unlike the monolayer case, it is possible to open an energy gap by inducing a potential difference between the two layers (figure 1.6) [14]. This is usually achieved experimentally by positioning a top gate on the bilayer graphene sheet in addition to the usual back gate. By tuning the two gates, a displacement field is induced to the sample, leading to a breaking of the symmetry between the two graphene layers and the opening of a gap. Such bilayer graphene devices could be suitable for electronic applications, where limiting the conductivity is needed. Calculations showed that inducing mechanical strain to a bilayer graphene sheet can be an alternative way to break the symmetry between the two layers and open a gap [16, 17, 18].

Oostinga *et al.* designed in 2007 a sample consisting of a connected bilayer graphene sheet with two gates. By inducing an electric field through the sample, the authors measured a high resistivity state that is explained by the opening of the gap (figure 1.7) [19]. This result has been reproduced several times, notably by Taychatanapat *et al.* at higher displacement fields [20], and Zhang *et al.* who additionally measured the gap by infrared microspectroscopy [21] (however, the optical gap does not correspond to the one measured by transport). The opening of a gap has been observed through transport measurements in suspended bilayer graphene sheets, too [22, 23].

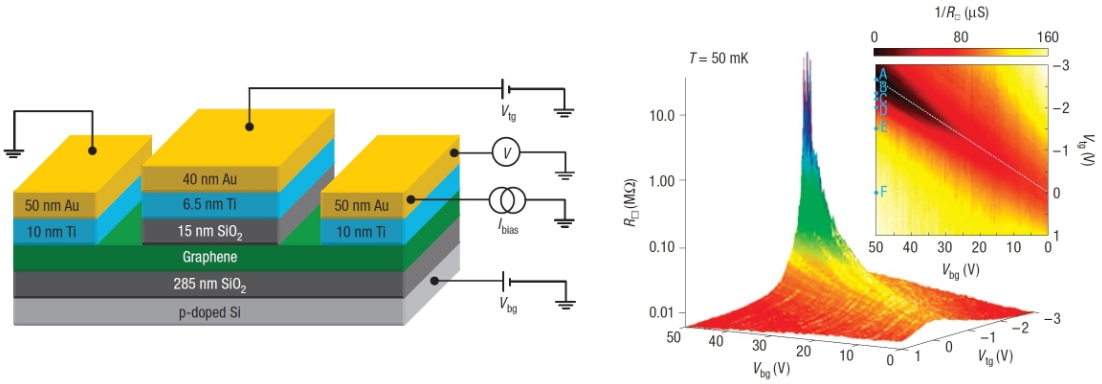

Figure 1.7: Left: scheme of a double-gated bilayer graphene sheet sample. Right: square resistance of the sample at 50 mK and as a function of the gate voltages. A high resistivity state is observed when inducing an electric field through the bilayer sheet. Adapted from [19].

Chapter 2

Proximity-induced superconductivity

This chapter presents the physical effects that can occur over a mesoscopic distance when a non-superconducting material is in contact with one or between several superconducting electrodes. A first section treats the general situation, and a second focuses on the case where graphene is used as the non-superconducting material.

2.1 Basics of superconductivity

In the next sections, we use the notations and results of the BCS theory of superconductivity. This theory was proposed by John Bardeen, Leon Neil Cooper, and John Robert Schrieffer in 1957, and considers that the origin of superconductivity is the condensation of electrons of opposite spins into pairs (called Cooper pairs) having then a boson-like behavior. This pairing comes from interactions with the crystal lattice. The electron pairs do not have to obey the Pauli exclusion principle anymore, and can condensate into the same energy level. The superconductivity is thus characterised by a mesoscopic wavefunction with a well-defined phase φ. Because the energy of an electron pair is slightly lower than the energy of two separated electrons, an energy gap emerges. The dissipationless nature of the current comes from the fact that at sufficiently low temperature the interactions with the lattice are not able to affect the condensate of Cooper pairs as a whole, which as a consequence does not experience resistance.

The important characteristics of superconductors used in the next sections are the superconducting gap Δ, the critical temperature T_c up to which we can observe the phenomenon described previously, the superconducting coherence length ξ characterising the distance up to which Cooper pairs can spread, and the London penetration depth λ defining the distance up to which a magnetic field can penetrate into a superconductor.

If a superconductor is in contact with a non-superconducting material, the Cooper pairs can diffuse into this material up to a short distance. This effect is called the proximity effect. If this material is connected with closely spaced superconducting electrodes (with a distance below the superconducting coherence length ξ), it is possible to observe an induced supercurrent flowing as if the material was superconducting itself. This effect is called proximity induced superconductivity.

2.2 General case

2.2.1 Induced supercurrent

2.2.1.1 Josephson effect

Brian David Josephson predicted in 1962 that a supercurrent can flow through a thin insulating barrier connected with two superconducting electrodes [24]. While the original prediction is based on quantum tunnelling calculations, this effect actually occurs whenever two superconducting electrodes are separated by a so-called weak link (figure 2.1). The presence of a supercurrent is a manifestation of the quantum coupling between the two superconductors. Even if the weak link was an insulator in the original prediction, it can be a non-superconducting (or "normal") metal or a physical constriction as well.

Theoretical calculations lead to two main equations, corresponding to the DC and AC Josephson effects. When the voltage difference between the superconductors is zero, the supercurrent through the junction depends on $\Delta\varphi(t)$ the phase difference between the two superconductors:

$$I(t) = I_c sin(\Delta\varphi(t)) \tag{2.1}$$

with I_c the maximum supercurrent, also called the critical current. Equation 2.1 corresponds to the DC Josephson effect.

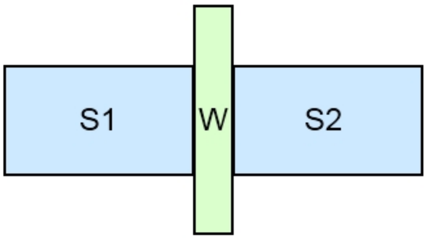

Figure 2.1: General diagram of a Josephson junction, with the two superconducting materials $S1$ and $S2$, and the weak link W. This weak leak can be an insulator, a non-superconducting material or a physical constriction.

When a potential difference V is applied to the junction, the system is described by the AC Josephson equation:

$$\frac{d(\Delta\varphi(t))}{dt} = \frac{2eV}{\hbar} \tag{2.2}$$

A non-zero potential V, by virtue of equation 2.1, induces an alternative supercurrent of frequency $f_J = 2eV/h$.

2.2.1.2 RCSJ model

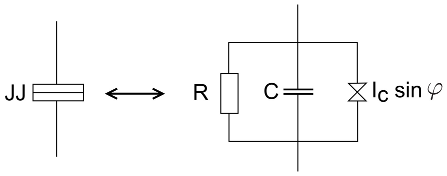

Figure 2.2: Electrical scheme of the resistively and capacitively shunted Josephson junctions model.

Real Josephson junctions are usually described by the resistively and capacitively shunted Josephson junctions model (RCSJ model), shown in picture 2.2. As suggested by the name, it consists of an ideal Josephson junction in parallel with a resistor R and a capacitor C. The total current going through the junction is:

$$I = I_c sin\varphi + \frac{\hbar}{2eR}\frac{d\varphi}{dt} + \frac{\hbar C}{2e}\frac{d^2\varphi}{dt^2} \tag{2.3}$$

Here φ denotes the phase difference between the two superconductors. By defining the plasma frequency of the junction $\omega_p = \sqrt{2eI_c/\hbar C}$, $\tau = \omega_p t$ and the quality factor $Q = \omega_p RC$, we get:

$$\frac{I}{Ic} = sin\varphi + \frac{1}{Q}\frac{d\varphi}{d\tau} + \frac{d^2\varphi}{d\tau^2} \tag{2.4}$$

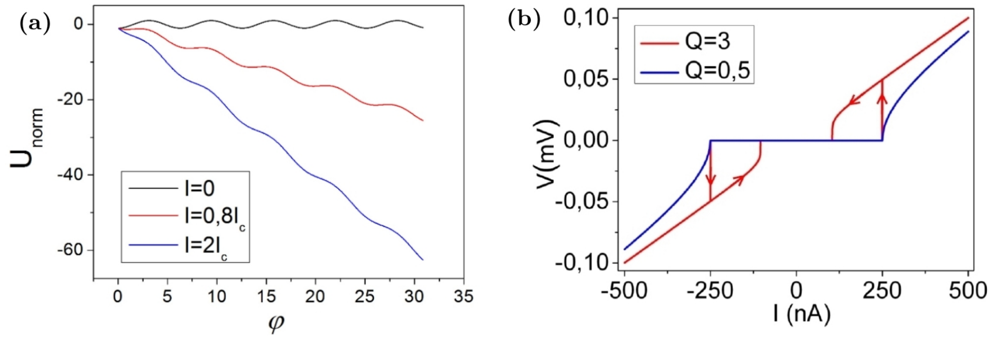

Figure 2.3: (a) Representation of the normalized potential in which the equivalent classical particle described in text is moving, for various currents I. The DC Josephson effect will occur only if the particle gets stuck inside a low-potential valley, and the AC Josephson effect will occur otherwise. If $|I| > I_c$, the particle will "fall". By reducing I (from $I > I_c$), the particle might keep falling even if I gets smaller than I_c: this is the origin of the hysteresis visible on figure 2.3b. (b) Numerical simulations of the RCSJ model for two junctions with the same critical current $I_c = 250$ nA and resistance $R = 200\ \Omega$, but with two different values $Q = 3$ and $Q = 1/2$ for the quality factor. The corresponding plasma frequencies are $5,06.10^{10}$ Hz and $3,04.10^{11}$ Hz. The source code of the program used to generate this curve is presented in appendix B.

This equation is analogous to the movement of a classical particle with mass $(\hbar/2e)^2C$ in a potential $U(\varphi) = -\frac{\hbar I_c}{2e}\cos\varphi - \frac{\hbar I}{2e}\varphi$. The periodic term of this potential might leads to the presence of a hysteresis: if we consider the analogous classical particle, depending on its velocity the particle can be retained or not in the low-potential valleys (figure 2.3a). The value of the quality factor Q determines the shape of the current-voltage curves around $I = I_c$ and the presence or absence of this hysteresis. Two regimes are observable (figure 2.3b):

- $Q < 1/2$, the junction is overdamped, the transition from the superconducting state to the normal state is smooth, no hysteresis is present.
- $Q > 1/2$, the junction is underdamped, the transition from the superconducting state and the normal state is straight, and an hysteresis effect can be observed.

2.2.1.3 Shapiro steps

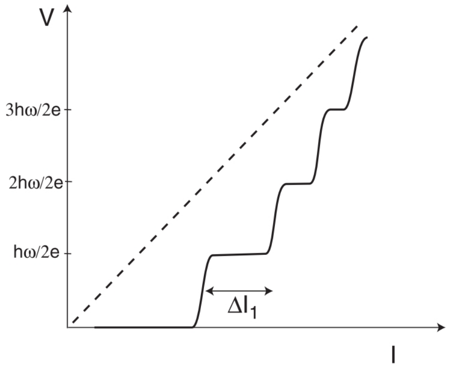

Figure 2.4: Shapiro steps visible on the current-voltage characteristic of a Josephson junction. Adapted from [25].

If a Josephson junction is driven by an AC voltage of frequency ω (or subjected to a radio-frequency field), the current-voltage curve exhibits voltage steps of amplitude $\hbar\omega/2e$ [26]. Let us consider the voltage applied to the junction:

$$V = V_0 + V_1\cos(\omega t) \tag{2.5}$$

By replacing this expression in equation 2.2 and by integrating, we determine the phase difference:

$$\varphi = \varphi_0 + \omega_J t + (2eV_1/\hbar\omega)\sin(\omega t) \tag{2.6}$$

with φ_0 a constant and $\omega_J = 2eV_0/\hbar$ the Josephson pulsation. By replacing 2.6 into 2.1 and after some mathematical transformations, we get an expression of the current using Bessel functions:

$$I = I_c\sin(\varphi) = I_c\sum_{k=-\infty}^{\infty}(-1)^k J_k(2eV_1/\hbar\omega)\sin(\varphi_0 + \omega_J t - k\omega t) \tag{2.7}$$

When V reaches $n\hbar\omega/2e$, with n an integer, then $\omega_J = n\omega$ and a component $I_n = I_c J_n(2eV_1/\hbar\omega)\sin(\varphi_0 + n\pi)$ is added to the total DC current. This leads to the presence of steps of width $\Delta I_n = 2I_c J_k(2eV_1/\hbar w)$ in the current-voltage characteristic, visible on figure 2.4. The junction acts as a frequency to voltage converter. To observe Shapiro steps experimentally, high enough frequencies must be employed. As an example, a frequency of 5 GHz leads to voltage steps of roughly $\Delta V = 10.3$ µV.

2.2.1.4 Magnetic field dependence and Fraunhofer pattern

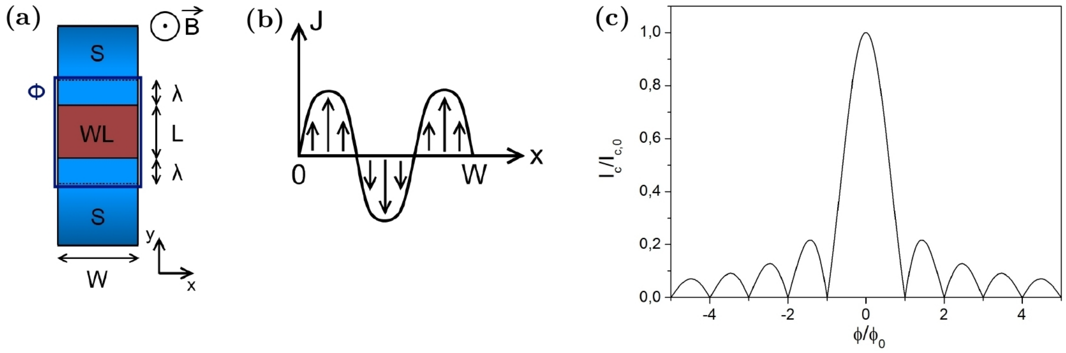

Figure 2.5: (a) Josephson junction under a perpendicular $\vec{B}$ magnetic field. (b) Representation of the current density along the $\vec{x}$ direction in the case $\Phi = \frac{3}{2}\Phi_0$. (c) The total critical current as a function of the flux Φ.

In the presence of a magnetic field $\vec{B}$ perpendicular to the supercurrent (figure 2.5a), the phases of electrons are affected by the vector potential and the phase difference across a Josephson junction is not homogeneous anymore. The magnetic flux through the junction (electrodes and weak link) is:

$$\Phi = \iint \vec{B}.\vec{dS} \tag{2.8}$$

with the integration area defined by the weak link surface and the parts of the electrodes covered by the London penetration depth λ. For a rectangular Josephson junction of length L and width W, and with a homogeneous and perpendicularly applied magnetic field $\vec{B}$ (figure 2.5a), we have $\Phi = BW(L + 2\lambda)$.

By exploiting the gauge invariance condition in the superconducting electrodes $\vec{\nabla}\varphi = \frac{2\pi}{\Phi_0}\vec{A}$ (with $\vec{A}$ the magnetic vector potential), one can determine the phase difference between two points of the junction [27]. Still in the case of a rectangular junction, integrating the phase difference along the direction of the current leads to an oscillating current density, with the period depending on the ratio Φ/Φ_0, with $\Phi_0 = h/2e$ the magnetic flux quantum. Figure 2.5b illustrates the case where $\Phi = \frac{3}{2}\Phi_0$.

By integrating the current along the complete junction, the expression of the total supercurrent is given by:

$$I_c = I_{c0}\left|\frac{sin(\pi\Phi/\Phi_0)}{(\pi\Phi/\Phi_0)}\right| \tag{2.9}$$

with I_{c0} the critical current without any magnetic field. The resulting critical current as a function of the flux Φ is plotted on figure 2.5c. The obtained pattern is similar to the one obtain by the optical diffraction of light passing through a thin slit: consequently it is usually referred to as the Fraunhofer pattern as well.

2.2.1.5 Critical current and temperature dependence

There is no simple and universal expression of the critical current I_c. Depending on the properties of the considered Josephson junction, several models exist. Generally, the critical current is a function of the normal state resistance of the junction R_N and the superconducting gap Δ (or Δ_1 and Δ_2 if the junction is made with two different materials). As one could expect, in any case the critical current will vanishes at $T = T_c$.

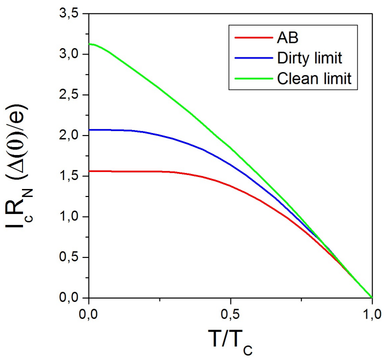

Figure 2.6: Temperature dependence of the product of normal-state resistance and critical current for three different types of weak links: the tunnel junction theory (Ambegaokar and Baratoff, equation 2.10), the Kulik and Omel'yanchuk models in the dirty limit (equation 2.11) and in the clean limit (equation 2.12).

A simple way to describe a Josephson junction is to consider it as a tunnel junction. The expression of the critical current has been calculated by Ambegaokar and Baratoff [28]:

$$I_cR_N(AB) = \frac{\pi\Delta}{2e}\tanh\frac{\Delta}{2k_BT} \tag{2.10}$$

This result is valid only for diffusive junctions and near T_c. Kulik and Omel'yanchuk used a more sophisticated theory based on Usadel's equations [29]. Their results are valid from $T = 0$ to T_c. Here l is the electronic mean free path, L the length of the junction and ξ the superconducting coherence length. At $T = 0$, their results give $I_cR_N = 2,07\Delta/e$ in the dirty case $l \ll L \ll \xi$, and $I_cR_N = \pi\Delta/e$ in the clean case $L \ll l, \xi$. Both results are higher than the one given by the tunnel junction theory ($I_cR_N = \pi\Delta/2e$). The expressions for non-zero temperature are:

$$(I_cR_N)_{dirty} = \frac{4\pi k_BT}{e}\sum_{w>0}\frac{\Delta\cos(\varphi/2)}{\delta}\arctan\frac{\Delta\sin(\varphi/2)}{\delta} \tag{2.11}$$

with $\delta = \sqrt{\Delta^2 \cos^2(\varphi/2) + \omega^2}$, $w = \pi T(2n+1)$, and:

$$(I_c R_N)_{clean} = \frac{\pi\Delta}{e} \sin(\varphi/2) \tanh \frac{\Delta \cos(\varphi/2)}{2k_B T} \tag{2.12}$$

The results of the three previous models are presented on figure 2.6. The normal state resistance R_N can be measured experimentally by adding a small magnetic field, high enough to suppress superconductivity in the bulk electrodes.

2.2.2 Andreev reflection

Andreev reflection occurs at normal metal-superconductor interfaces. Due to the existence of a gap Δ around the Fermi energy in the density of states of the superconductor, a single electron of energy $|\epsilon| < \Delta$ (with $|\epsilon| = E - E_f$ the excitation energy) coming from the normal metal cannot enter the superconductor. Andreev showed that such an electron can still flow through the superconductor by forming a Cooper pair with a second electron extracted from the metal [30]. The missing $-e$ charge is retro-reflected as a hole in the metal (figure 2.7a and 2.7b). The energy, momentum and spin conservation lead to the following conditions (the indices e and h design respectively the incident electron and the reflected hole):

- $\epsilon_h = E_h - E_F = -\epsilon_e = -(E_e - E_F)$.
- $\vec{k_h} = \vec{k_F} - \vec{\delta k}$, with $\vec{\delta k}$ defined by $\vec{k_e} = \vec{k_F} + \vec{\delta k}$.
- The spin of the reflected hole is the opposite one of the incident electron.

The difference between the two wave vectors is $2\delta k = 2\epsilon/\hbar v_F$. In addition, the reflection induces a phase change to the reflected hole:

$$\delta\phi = \varphi - \arccos\frac{\epsilon}{\Delta} \tag{2.13}$$

With φ the phase in the superconductor. If $\epsilon = 0$, the reflected hole tracks the very same path of the incident electron.

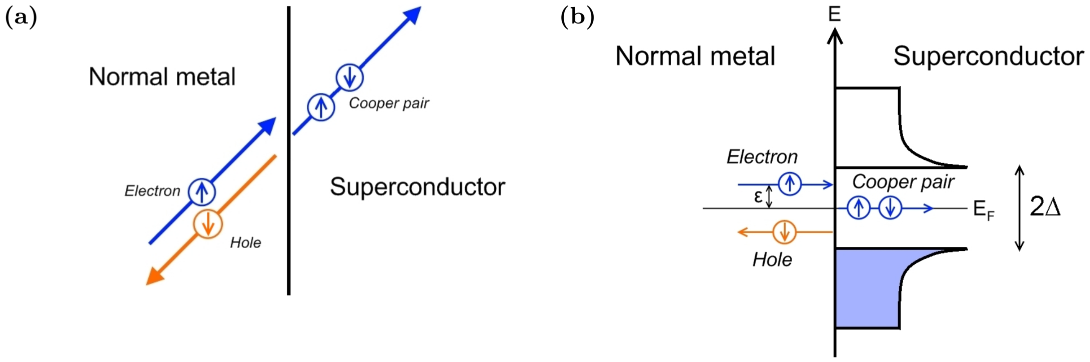

Figure 2.7: Andreev reflection in a normal metal-supraconductor interface in real space (a), and the corresponding energy diagram (b).

The phenomenon is time-reversible: one obtains a comparable reflection when a hole reaches the metal-superconductor interface. A Cooper pair is removed from the superconductor, and an electron is reflected.

2.2.2.1 Multiple Andreev reflection

When a metal is connected between two closely spaced superconductor metals, we can observe multiple Andreev reflection (MAR) states. Indeed, any electron or hole (with a low enough energy) might be reflected several times when reaching the metal-superconductor interfaces, leading to some visible features in the differential resistance. This effect has been explained by Klapwijk *et al.* in 1982 [31] [32]. Let us consider the case of an electron of energy E_0 coming from the left electrode of a SNS junction (figure 2.8a). A voltage V is applied to the system. While crossing the normal metal, the electron will gain the energy eV. The reflected hole will lose the energy eV by crossing the normal section, and due to the sign change of the energy the reflected electron will have the energy $E_0 + 2eV$. The reflections will continue until the energy acquired exceeds Δ and the electron can enter the quasiparticle continuum. Increasing the voltage V will make the charge carriers reach this limit in fewer steps. Every time that eV reaches $2\Delta/n$, the reflection process is modified. This leads to a subharmonic gap structure visible in the differential resistance versus applied voltage, see figure 2.8b. Experimentally, only the few first n features are usually observable (figure 2.8b).

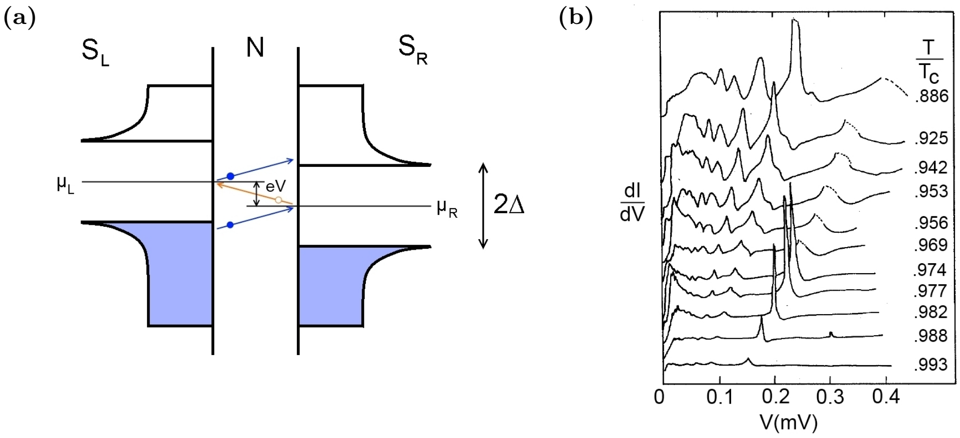

Figure 2.8: (a) Energy diagram of a multiple Andreev reflection process. The particle entering from the left electrode gain eV energy at each reflection. When the energy is higher than 2Δ, the particle leave the non-superconducting area. (b) Differential conductance measurement over a tin microbridge and at several temperatures, performed by Octavio *et al.* [33]. The features follow the $2\Delta/n$ pattern and have been attributed to multiple Andreev reflection [27].

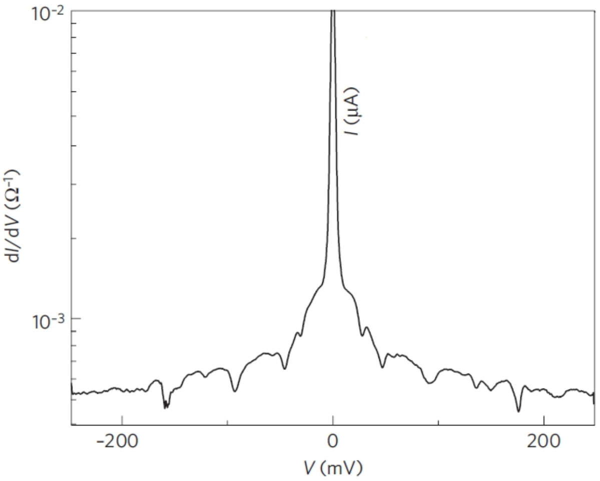

Figure 2.9: Differential conductance of a superconductor ($YBa_2Cu_3O_7$) / ferromagnetic ($La_{0.7}Ca_{0.3}MnO_3$) / superconductor junction ($YBa_2Cu_3O_7$), exhibiting a set of McMillan-Rowell and Tomasch oscillations mixed. Adapted from [34].

2.2.2.2 Tomasch and McMillan-Rowell oscillations

Under certain conditions, Andreev reflection leads to resonance peaks in the differential resistance curve of a SNS junction that cannot be explained by the MAR states.

McMillan-Rowell oscillations originate from interferences in the normal-state area of a SNS junction [35]. The easiest way to illustrate the phenomenon is to consider an asymmetric SNS junction where Andreev reflection is predominant on one side and normal reflection is predominant on the other one. An electron in the normal-state area coming to the side where Andreev reflection is predominant will be reflected as a hole. This hole will cross the normal-state area two times (the second time after a normal reflection on the second side) and will be reflected as an electron in the original energy state. This electron can interfere with the first incident electron. This leads to conductance oscillations with resistance peaks at voltages given by:

$$eV_m = eV_0 + \frac{mhv_F^N}{4L_N} \tag{2.14}$$

with m an integer, v_F^N the Fermi velocity in the normal area, and L_N its length.

Tomasch oscillations, on the contrary, are due to interferences occurring in the superconducting part of the junction. In usual superconductors, quasiparticles combine the properties of electron and hole, but with one type dominating. Due to possible local perturbations of the energy gap at the normal-superconductor interface, an electron-like quasiparticle can be Andreev-reflected as a hole-like one, leading to an interference [36] [37]. Those interferences lead to resistance peaks at voltages given by:

$$eV_m = \pm\sqrt{\Delta^2 + \left(\frac{mhv_F^S}{2L_S}\right)^2} \tag{2.15}$$

with m an integer, v_F^N the Fermi velocity in the superconducting area, and L_S its length.

2.3 Proximity-induced superconductivity in graphene

2.3.1 Induced supercurrent

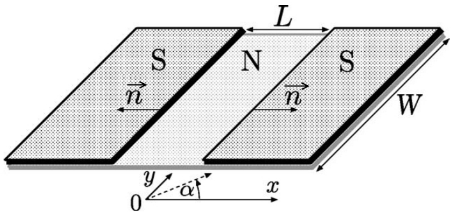

Figure 2.10: Diagram of a superconductor-graphene-superconductor junction, of length L and width W. The normalized vector $\vec{n}$ points from the graphene sheet to the superconducting electrode of the associated interface. Adapted from [38]

The critical current of a short ballistic superconductor-graphene-superconductor (SGS) junction has been calculated by Titov and Beenakker [38]. The junction can be modeled as shown in the picture 2.10, with a graphene sheet in the $x - y$ plane of width W covered by two superconducting electrodes (of superconducting gap Δ_0) in the regions $x < -L/2$ and $x > L/2$. To determine the supercurrent, the Bogoliubov-De Gennes equation is used. This equation can describe coherent mixtures of electrons and holes in superconductors in which the pairing potential is not constant:

$$\begin{pmatrix} H - E_F & \Delta \\ \Delta^* & E_F - H \end{pmatrix} \begin{pmatrix} \Psi_e \\ \Psi_h \end{pmatrix} = \epsilon \begin{pmatrix} \Psi_e \\ \Psi_h \end{pmatrix} \tag{2.16}$$

with Ψ_e and Ψ_h the wave functions of electrons and holes respectively, ϵ the excitation energy, H the Hamiltonian for one particle and Δ the Cooper-pair potential. In the graphene (non-superconducting) area, the Cooper-pair potential is zero, and the charge carriers are described by the Dirac Hamiltonian. Equation 2.16 becomes the so-called Dirac-Bogoliubov-De Gennes equation:

$$\begin{pmatrix} H_0 - E_F & 0 \\ 0 & E_F - H_0 \end{pmatrix} \begin{pmatrix} \Psi_e \\ \Psi_h \end{pmatrix} = \epsilon \begin{pmatrix} \Psi_e \\ \Psi_h \end{pmatrix} \tag{2.17}$$

with $H_0 = -i\hbar\nu(\sigma_x\partial_x + \sigma_y\partial_y)$ the Dirac Hamiltonian, E_F the Femi level in the graphene area and σ_i the Pauli matrices. The boundary conditions read:

$$\Psi_h(\vec{r}) = U\Psi_e(\vec{r}) \tag{2.18}$$

$$U = \frac{1}{\Delta}(\epsilon - i\sqrt{|\Delta|^2 - \epsilon^2}\vec{n}.\vec{\sigma}) = e^{-i\Phi - i\beta\vec{n}.\vec{\sigma}} \tag{2.19}$$

with $\vec{r}$ a point located at one of the graphene-electrode interfaces, $\Delta = \Delta_0 e^{i\Phi}$ the pair potential in the superconductor, $\vec{\sigma} = (\sigma_x, \sigma_y)$ the vector of Pauli matrices, $\beta = \arccos(\epsilon/\Delta_0)$ (with $\beta \in [0, \pi/2]$) and $\vec{n}$ the unit vector pointing from the graphene to the superconductor.

This Hamiltonian has been solved in the short-junction regime ($L \ll \xi$”, $L \ll W$) [38]. Because there is no simple analytic equation of the resulting supercurrent, we will briefly describe the results in two different regimes depending on the position of the Fermi energy, one far away from the Dirac point and the second around it ($E_F \ll \hbar\nu/L$). In this latter case, the critical current is:

$$I_c = 1.33\frac{e\Delta_0}{\hbar}\frac{W}{\pi L} \tag{2.20}$$

Still in the short-junction regime, far away from the Dirac point the critical current depends linearly on E_F:

$$I_c = 1.22\frac{e\Delta_0}{\hbar}\frac{E_F W}{\pi\hbar\nu} \tag{2.21}$$

In the short-junction regime, the expected $I_c R_N$ product is $I_c R_N = 2.08\Delta_0/e$ around the Dirac point and $I_c R_N = 2.44\Delta_0/e$ far away from it, with R_N the junction's resistance in the normal state.

Unlike the usual metallic SNS junctions, it is possible to directly tune the critical current amplitude of a SGS junction through the Fermi level of the graphene sheet. Another interesting feature is the ability to handle a supercurrent even if the Fermi level is set to the Dirac point, where the charge carrier concentration is in principle zero.

The previous results are valid only at $T = 0$. For non-zero temperatures, calculations of the supercurrent specific to graphene have been made by Sarvestani and Jafari [39], with a relatively good agreement with experimental results. They pointed out two different regimes, depending on the length L of the junction compared to the superconducting coherence length ξ. They are presented on figure 2.11.

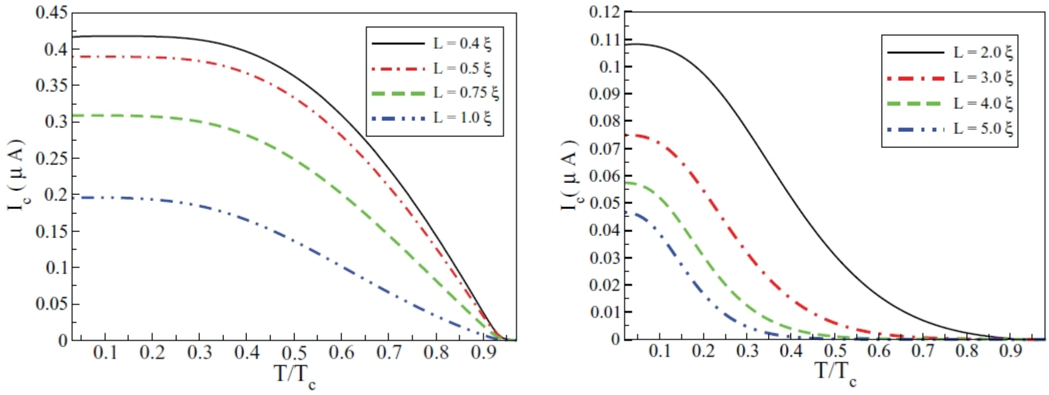

Figure 2.11: Expected temperature dependence of the supercurrent of a wide ($W \gg L, \xi$) SGS junction, for different L/ξ ratios. Adapted from [39].

2.3.2 Specular Andreev reflection in graphene

In graphene, the Andreev reflection process is different from the situation discussed in the previous section 2.2.2. Depending on the excitation energy $\epsilon = E - E_f$ of an indicent electron, two cases are possible [40]:

- $\epsilon < E_f$: intra-band reflection
- $\epsilon > E_f$: inter-band reflection

Andreev reflection does not occur the same way for the two situations. Let us consider the Bogoliubov-De Gennes equation for a graphene-superconductor junction, where the graphene occupies the $x > 0$ area:

$$\begin{pmatrix} H - E_f & \Delta \\ \Delta^* & E_f - H \end{pmatrix} \begin{pmatrix} \Psi_e \\ \Psi_h \end{pmatrix} = \epsilon \begin{pmatrix} \Psi_e \\ \Psi_h \end{pmatrix} \tag{2.22}$$

with Ψ_e and Ψ_h the wave functions of electrons and holes respectively, ϵ the excitation energy, H the Hamiltonian for one particle and Δ the Cooper-pair potential. This potential is described by:

$$\Delta = \begin{cases} 0 & \text{in the graphene sheet}(x > 0) \\ \Delta_0 e^{i\varphi} & \text{in the superconducting electrodes}(x < 0) \end{cases}$$

with Δ_0 the superconductor gap and φ the phase. By coupling this equation with the graphene Hamiltonian, we get:

$$\epsilon = \sqrt{|\Delta|^2 + (E_f - U \pm \hbar\nu|\vec{k}|)^2} \tag{2.23}$$

with + referring to the conduction band, − to the valence band, and U the electrostatic potential defined by:

$$U = \begin{cases} 0 & \text{in the graphene sheet}(x > 0) \\ -U_0 & \text{in the superconducting electrodes}(x < 0) \end{cases} \tag{2.24}$$

This result (using mean field theory) is correct if $\Delta_0 \ll E_f + U_0$ and if $\xi = \hbar v/\Delta_0 \gg \lambda'_f$, the Fermi wavelength in the superconducting area. In the graphene sheet, the dispersion relation becomes (with $U = \Delta = 0$):

$$\epsilon = |E_f \pm \hbar\nu\sqrt{\delta k_x^2 + \delta k_y^2}| \tag{2.25}$$

Let us consider that ϵ is slightly inferior to Δ_0. Because the superconductor-graphene interface is located on $x = 0$, δk_y is conserved during the transition. ϵ is conserved as well. We have then to determine δk_x. The derivative

$$v_x = \frac{1}{\hbar}\frac{\partial \epsilon}{\partial \delta k_x} \tag{2.26}$$

has to be positive (otherwise we would get a hole getting into the superconducting area). Only one of the remaining solutions corresponds to a reflected hole. This hole can belong to the conduction band (where it would move in the opposite direction of its wave vector) if $\epsilon < E_f$, or to the valence band (in which it would move in the same direction as its wave vector) if $\epsilon > E_f$ (figure 2.12a). Due to the conservation of

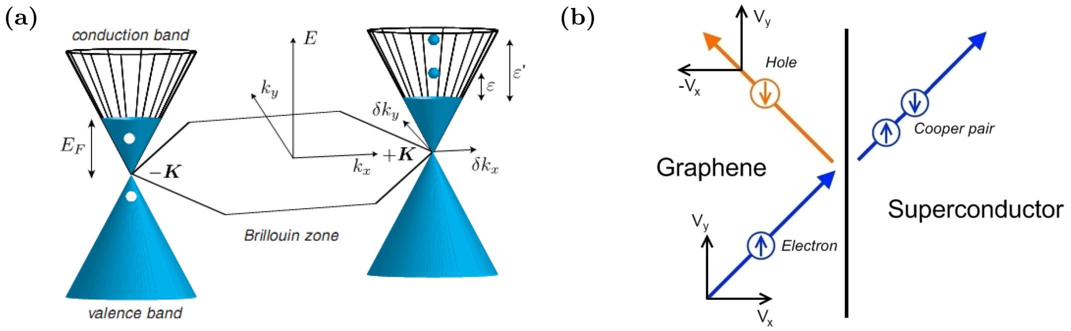

Figure 2.12: (a) The electrons and holes in the graphene band structure, for the two cases possible, corresponding to the excitation energies ϵ and ϵ'. For the electron of excitation energy $\epsilon < E_F$, the corresponding hole is located in the same band: we obtain a regular Andreev retro-reflection. For the second electron of excitation energy $\epsilon' > E_F$, the corresponding hole switches to the valence band: we obtain a specular Andreev reflection. Adapted from [41]. (b) Specular Andreev reflection in a graphene-supraconductor interface in real space. This reflection occurs when $\epsilon > E_F$.

δk_y, in the conduction-band case both v_y and v_x change their signs: we get a classic retro-reflection. In the valence-band case v_x changes sign but not v_y: we get a specular Andreev reflection (figure 2.12b).

The multiple Andreev reflection described in the previous section can occur in SGS junction, too. Analogously to the possibility to tune the critical current of such a junction, the shape of the $2\Delta/n$ peaks visible in the differential conductance will be affected by the position of the Fermi level in the graphene part of the junction. Cuevas *et al.* calculated the expected differential conductance of such junctions, presented in figure 2.13 [42].

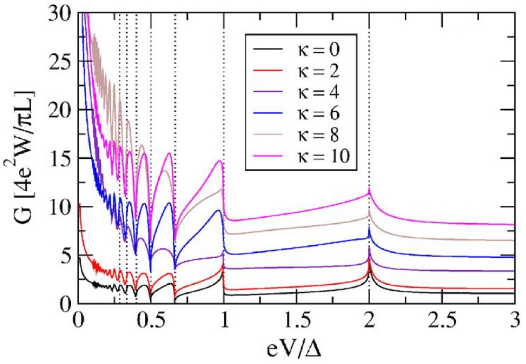

Figure 2.13: Expected differential conductance of a short ($L < \xi$) superconductor-graphene-superconductor junction for various normalised gate voltages κ. Due to the opening of new Andreev reflection processes, peaks are present at every $2\Delta/n$ voltages. Adapted from [42].

2.4 Overview of previous experimental results

The literature related to proximity induced superconductivity in graphene is already abundant. Here we present a short review of some important papers or results.

Heersche *et al.* reported the first measurement of an induced supercurrent (as well as multiple Andreev reflection) in a graphene sheet deposited on top of a Si/SiO$_2$ wafer and contacted with titanium/aluminium electrodes (figure 2.14) [43]. The critical current was tunable up to around 140 nA with the charge carrier density (controlled by the gate voltage), and was still finite at the Dirac point. The measured I_cR_N product range was from 50 to 120 µeV. This is lower than the expected theoretical value $I_cR_N = 2,44\Delta/e$ (305 µeV for this sample) for a short ballistic SGS junction, according to reference [38].

Several comparable results have been reported since then [44, 45, 46, 47]. Ojeda *et al.* did similar measurements with tantalum contacts [48]. At first no supercurrent was present. Several annealing steps performed by running a large current through the sample improved the quality of the graphene-superconductor interface and reduced the resistance, leading to the possibility to observe an induced supercurrent. Measurements of supercurrent in Pb-graphene-Pb junction have been reported by Jeong *et al.* [49] and Borzenets *et al.* [50]. Due to the high critical temperature of lead, in such devices the proximity-induced superconductivity can be observed up to $T \sim 4$ K.

Voutilainen *et al.* used superconductor-graphene-superconductor junctions to evaluate the energy relaxation in graphene [51]. The electron-electron relaxation times determined turned out to be much higher (up to 140 times) than the theoretical values.

Coskun *et al.* specifically studied the distribution of supercurrent switching as a function of temperature [52]. The authors found out that the standard deviation σ_{Ic} of the critical current is proportional to T^{α_G}, with α_G between 1/3 and 1/2. This result differs from the theoretical $\sigma \propto T^{\frac{2}{3}}$ relation in usual Josephson junctions, and is attributed to the temperature dependence of the critical current.

Measurements with electrodes that remain superconducting in high magnetic fields allowing the study of proximity effects in the quantum Hall regime have been performed by Katsuyoshi *et al.* [53] and Rickhaus *et al.* [54]. At zero magnetic field, a transition from superconductive to resistive state around the Dirac point has been reported in reference [53] and is attributed to the length of the junction. In the quantum Hall regime a conductivity enhancement of the plateaus has been noticed compared to the normal state. This is attributed to Andreev edge states, as Andreev reflection still occurs at the graphene-superconductor interfaces.

Choi *et al.* produced a dual gated graphene Josephson junction, in which a tunable potential barrier allows full control of the supercurrent and can turn it off completely [55]. Mizuno *et al.* reported in 2013 the design of a suspended graphene Josephson junction [56]. Due to the observed linear dependence of the critical current on the Fermi energy at high charge carrier density (in agreement to the theoretical predictions from reference [38]), the authors claimed that the transport was ballistic.

Those results demonstrated the possibility to realise SGS junctions with a variety of superconducting materials. The expected effects such as Andreev reflection or Shapiro

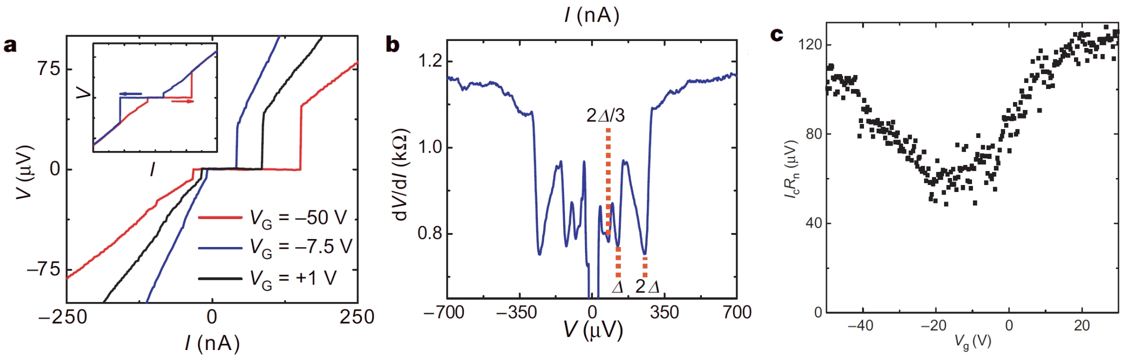

Figure 2.14: Measurements of a SGS junction at 30 mK, adapted from [43]. (a) IV curve of a SGS junction for various gate voltages, presenting a tunable supercurrent. (b) Differential resistance, showing resistance drops corresponding to the multiple Andreev reflections at $V = 2\Delta/n$. For this sample, the superconductor's gap is estimated at $\Delta = 125\ \mu eV$. (c) Variation of the I_cR_N product as a function of the gate voltage, lower than the expected theoretical value $I_cR_N = 305\ \mu eV$ for a short ballistic SGS junction.

steps have been observed. The possibility to tune the critical current with a gate is an additional feature compared to the usual SNS junctions using a metal as the non-superconducting material. The specular Andreev reflection has not been observed so far. No measurement relative to proximity-induced superconductivity in bilayer graphene sheets has been reported as well.

Chapter 3

Sample preparation techniques

In order to study its transport properties, graphene must first be properly isolated, identified and connected. This chapter presents the techniques used in this thesis to produce graphene samples. A first part details the standard process to produce graphene samples on top of Si/SiO$_2$ wafers. The next parts present more advanced techniques: the shadow evaporations to design short junctions, the transfer technique to use hexagonal boron nitride as a substrate for graphene, and the different possibilities to design an additional top-gate on our samples. These two last techniques are employed to produce dual-gated bilayer graphene sheets samples.

3.1 Standard samples on Si/SiO$_2$ wafers

3.1.1 Substrate preparation

The easiest way to produce graphene samples is to use Si/SiO$_2$ wafers as a substrate. To be able to use it like a gate, the silicon is highly doped with boron atoms (p-doping). The resulting resistivity is smaller than 0.005 Ω cm. The thickness of the oxide is about 300 nm. In order to easily localize the samples and to facilitate alignments in further lithography steps, metal markers are added to the wafer with standard lithography and metal deposition technique described in section 3.1.5. Palladium and gold were preferred, in order to make the markers visible during the lithography process, even with one or several layer of resist on top of them. The wafer is then cleaned (especially from the resist residues) with a rather soft oxygen plasma etching step. The wafer is then split into several usable individual ones, large enough (around 1 cm^2 size) to avoid accumulations on the edges when spin-coating thick layers of resist.

3.1.2 Graphene deposition

Graphene samples are prepared by mechanical exfoliation of a piece of graphite. This production technique has been reported by Novolesov *et al.* in 2005 [2]. Using highly pure natural graphite is a better choice than HOPG (highly oriented pyrolitic graphite), because HOPG has smaller monocristal domains. A little piece of graphite is put on a scotch tape. The tape is then pressed on itself several times, peeling the graphite. Given the structure of this material (consisting of layers linked mainly by Van der Waals interactions that can easily be broken mechanically), thinner and thinner parts of the initial graphite piece are disposed on the tape. The tape is then pressed onto the previously prepared wafers. Graphite sheets of different thicknesses are randomly distributed on the wafer.

3.1.3 Optical identification

With the used technique, graphene sheets are randomly deposited across the whole wafer and have to be searched with an optical microscope at high magnification. Even if graphene is only one-atom thick, it can still be seen on Si/SiO_2 substrates (figure 3.1), and the high contrast dependence on the graphite thickness allow to have a first idea of the nature of the sheet. For our purposes, an ideal graphene sheet would verify the following conditions:

- the sheet should be large enough to be connected with electrodes, at least a few µm^2.
- it should be homogeneous enough, so that the areas between the contacts have the same number of layers.
- the sheet should be somehow isolated, so that the future different electrodes do not get accidentally linked to each other by surrounding graphite sheets.

Monolayer, bilayer and multilayer sheets are then more clearly identified with Raman spectroscopy.

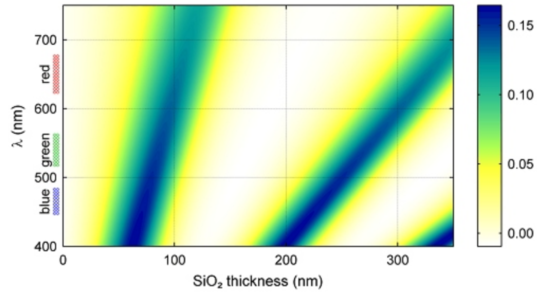

Figure 3.1: Optical contrast of a graphene sheet deposited on top of a Si/SiO_2 wafer as a function of wavelength and oxide thickness. Graphene is easier to see on a 100 nm oxide layer, but the oxide is more likely to break, leading to a leak. 300 nm is a good compromise. Adapted from [57].

3.1.4 Raman spectroscopy

Raman spectroscopy consists of measuring the shift in photon energy between an emitted signal (usually a monochromatic light from a laser) and its reflection. The energy

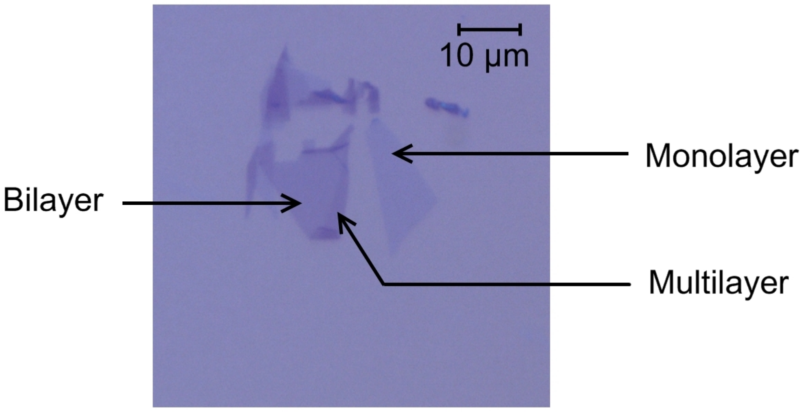

Figure 3.2: Optical picture of graphene deposited on a Si/SiO$_2$ wafer. Sheets of various thicknesses (monolayer, bilayer, multilayer) are indicated.

difference is usually due to interactions with phonons or plasmons present in the target sample. The situations where the re-emitted photon has a lower energy or higher energy are respectively called Stokes and anti-Stokes shifts. Raman spectroscopy can be used as a rather fast and non-invasive way to identify graphene. The first report of graphene Raman spectrums came from Ferrari *et al.* in 2006 [58], and Raman spectroscopy has quickly become the main way to identify graphene. In the Raman spectrum of a graphene sheet (mono-, bi-, or multi-layer), three peaks are important: the G peak (located at around 1580 cm^{-1}), the D peak, and the G'(or 2D) peak. The locations of the two last peaks depend on the wavelength of the used laser. Those three peaks can be used to determine the number of layers and to detect the presence of defects in the sample. They can be interpreted as follows (figure 3.3):

- The G peak corresponds to a normal first-order Raman scattering process. The incident photon excites one electron and creates an electron-hole pair. The electron interacts with an in-plane or longitudinal optical phonon and then recombines.

- The 2D peak corresponds to a second-order double-resonance Raman scattering process. This time the excited electron interacts twice with in-plane optical phonons before recombining. This process is highly dependent on the electronic band structure around the Dirac point. Especially, the presence of the supplementary energy bands in the bilayer graphene case leads to an easily recognisable shape. The 2D peak is therefore the most useful to determine the nature of the sheet.

- The D peak corresponds to a second-order double-resonance Raman scattering process involving a defect in the graphene.

Typical Raman spectrums for monolayer, bilayer, and multilayer graphene sheets are shown on figure 3.4. On most of our samples, the D peak was not at all or only barely visible. This peak is mainly observable at the edges of a graphene sheet, on graphene nanoribbons or after a chemical reaction.

On monolayer spectrums, the G and 2D peaks can be fitted by a Lorentz curve. The integrated area of the 2D peak is four times that of the G peak, and its intensity is higher.

In bilayer graphene sheet, the G peak is still fitted by a Lorentz curve. Because bilayer graphene has two energy bands around the Dirac point, the 2D peak needs the summation of four Lorentz curves to be fitted properly. Each Lorentz curve correspond to one of the possible Raman scattering process. A small step, characteristic of bilayer graphene sheets, is visible. The integrated area of the 2D peak is two times the one of the G peak. Their maximum intensity are comparable.

When more than two layers are present, the 2D peak stretches, looses intensity and gets closer to the usual graphite 2D peak.

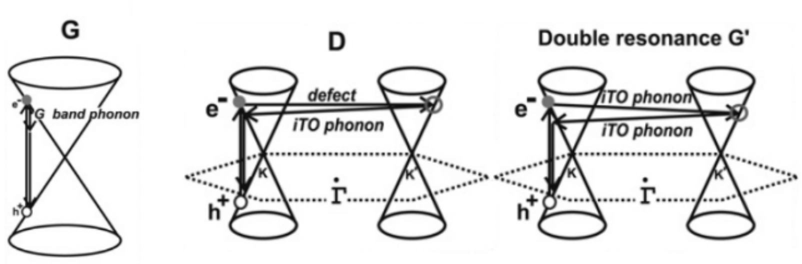

Figure 3.3: The different mechanisms at the origin of the main peaks used to identify graphene by Raman spectroscopy. Adapted from [59]

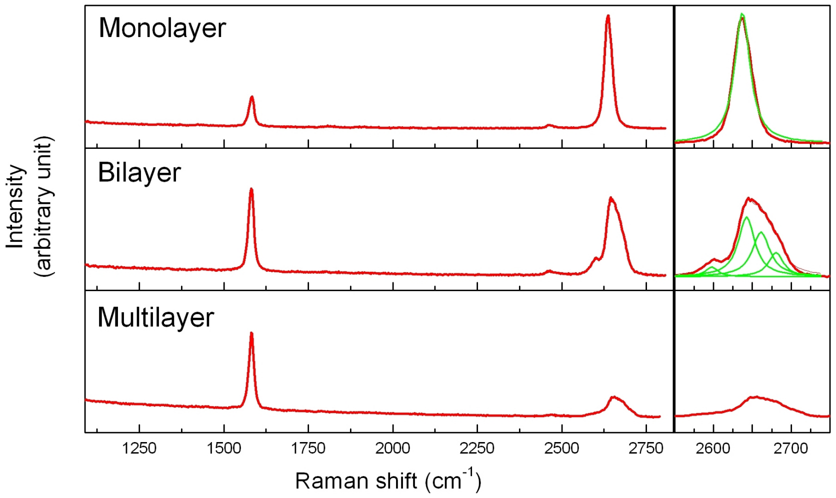

Figure 3.4: Typical Raman spectrums of a monolayer, a bilayer and a multilayer graphene sheets on top of a Si/SiO_2 substrate. The 2D peaks for monolayer and bilayer graphene are fit by a sum of respectively one and four Lorentz curves.

3.1.5 E-beam lithography and metal deposition

The contact deposition is made following a standard electron beam lithography and metal evaporation technique. A few drops of polymethyl methacrylate (PMMA) are deposited on top of the wafer. A spin-coater is then used, the rotation speed leading to the desired thickness. The PMMA resist used in this thesis is produced by All-Resist GmbH, and the target thickness was 200 nm. The sample is then backed to evaporate the solvent and get a solid resist layer. By using a SEM (scanning electron microscope), the resist can then be irradiated in some spots in order to be removed later on.

This lithography step has been performed either with a Leo 1530 SEM or with a Raith e-LiNE. A pattern file was previously designed, containing the geometry of both the graphene and the future lithography-produced parts. The markers pre-patterned on the wafer before any graphene deposition are now used to get the necessary coordinates and to perform an alignment before each irradiation step. After the lithography step, the sample is plunged into a solution of isopropanol/Methyl isobutyl ketone (MIBK) in order to be developed. The irradiated parts of the resists dissolve in this solution.

The deposited contacts are made of a short layer of titanium (5 nm) to assure both adhesion and good connection with the graphene, and a larger layer of aluminium (40 nm). The corresponding superconducting critical temperatures are respectively 0.38 K and 1.2 K. To ensure a good quality for the contacts, they are deposited in a ultra high vacuum device in which the pressure can go down to $\sim 10^{-10}$ mbar and at low temperature (the device is cooled down below -120 C by liquid nitrogen). The low temperature reduces the risk of formation of clusters and therefore the rugosity, especially for the aluminium layer.

The sample is then immersed into aceton to dissolve the resist left. Only the metal located in the previously developed area sticks to the wafer (or to the graphene sheet). The sample is then annealed for several hours at $T > 200$ °C. This can be done in air but this process is more efficient in high vacuum ($P \sim 10^{-6}$ mbar). This step improves the sample quality and removes the leftover resist.

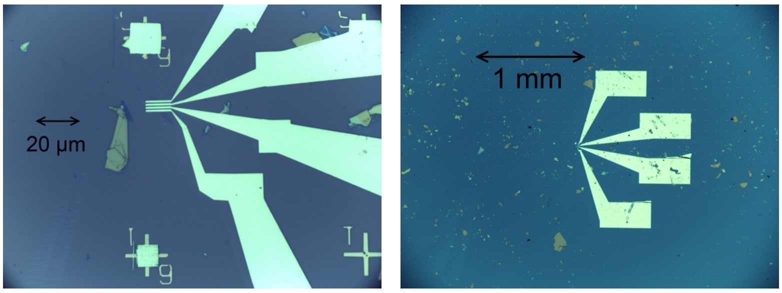

(a) **(b)**

Figure 3.5: Optical pictures of a connected graphene sample. The electrodes visible on (a) are linked to macroscopic pads visible on (b) that can be connected later on to measurement devices.

3.2 Ultra-short graphene junctions

To design really short metal-graphene-metal junctions, the lithography and metal deposition procedure described in the previous section can reveal its limits. Going below a distance of 100 nm between two contacts while keeping high aspect ratios is quite difficult. To solve this problem, one can use the technique known as shadow metal evaporation.

This technique is based on a improvement of the standard lithography/metal evaporation technique. We use a stack of two different resists: a rather thick one (800 nm) made of methyl methacryllate (MMA), and a thiner one (200 nm) made of PMMA on top.

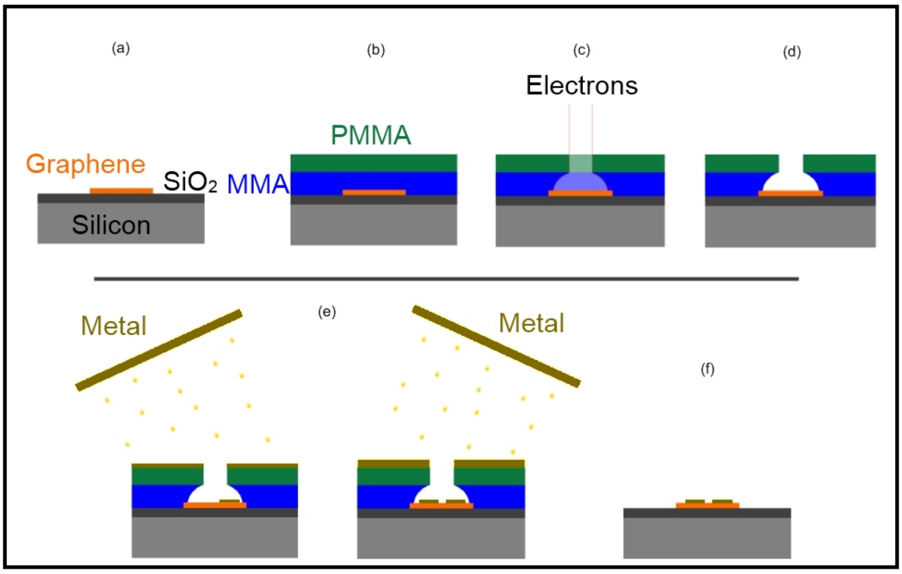

Figure 3.6: Schematic of the shadow evaporation technique. The two layers react differently to the lithography and development, leading to the creation of a cavity. This cavity is then exploited by multiple angles depositions.

Due to the different reaction of the two resist layers to electronic lithography (the MMA layer is basically more sensitive), it is possible to create a cavity. By using different angles during the metal deposition, we can then design and realize significantly more complex structures (figure 3.6). As it is possible to choose a different material for each deposition angle, this technique is the usual way to design tunnel and Josephson junctions. Another advantage is the possibility to make structures with a much higher aspect ratio, allowing the deposition of very close contacts (down to a few tens of nanometers). Figure 3.7 shows the pattern used to obtain short SGS junctions using two deposition angles, and the expected result. The details of the lithography and evaporation procedure are presented in appendix A. For the contacts, we use the same metals and thicknesses as in the previous section (5 nm of titanium, 40 nm of aluminium). Figures 3.8a and 3.8b show two AFM pictures of a graphene sample connected with this technique.

The main drawback of this technique is the precision it requires. The resulting structure is highly dependent on the angles, the thicknesses of the resist layers and on the dimensions of the lithographied area. Small mistakes can render the sample unusable. As an example, a lithography dose too high can lead to directly connected electrodes. In addition, as the contacts cross completely the graphene sheet, this sheet better be homogeneous and have a high aspect ratio in order to be able to put several contact pairs on it.

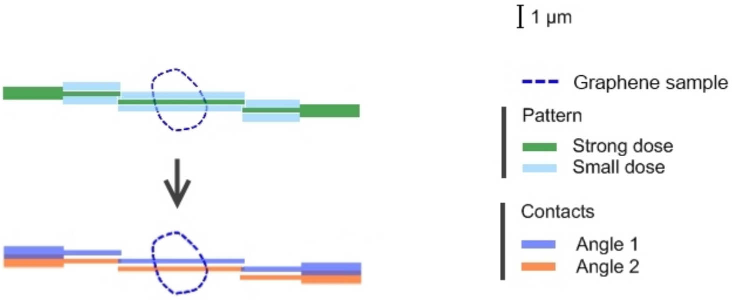

Figure 3.7: Scheme of the pattern used, and the expected result after the metal deposition.

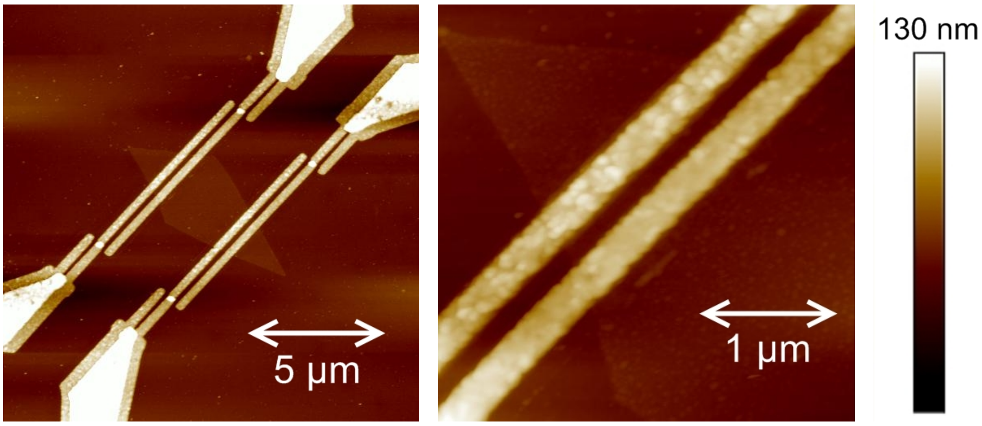

(a) (b)

Figure 3.8: Atomic force microscope pictures of a connected sheet, using the shadow evaporation technique.

3.3 Hexagonal boron nitride as a substrate for graphene

3.3.1 Interest of boron nitride substrates

Hexagonal boron nitride (hBN) is an insulating isomorph of graphite. A and B carbon atoms in graphite lattice are replaced with boron and nitrogen atoms respectively (figure 3.9). The in-plane bonds are ionic, and no delocalized electrons are present. Its lattice mismatch with graphite is small (1.7 %). The dielectric constant is close to that of silicon dioxide, $\epsilon = 3 - 4$, and the breakdown voltage is high enough to reach high charge carrier densities ($V_{breakdown} \approx 0.7$ V.nm^{-1}). The surface of an hexagonal boron nitride sheet is atomically flat and the material itself is very inert. Due to all of those properties, hBN is a material of choice as a substrate for graphene sheets.

Figure 3.9: Atomic structure of a single hexagonal boron nitride sheet. The distance between two neighboring atoms is $a = 1.44$ Å, which is a bit larger than in the graphene ($a = 1.42$ Å).

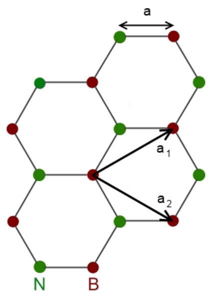

The first transport measurements onto a graphene sheet transferred onto a hBN substrate have been made by Dean *et al.* [60]. The measurements show a clear improvement of graphene's electronic properties. In particular, the carrier mobility might be improved by a factor of 10, and values up to $\sim$ 25 000 cm^2/Vs at room temperature have been reported. At low temperature, the mobility can reach $\sim$ 100 000 cm^2/Vs. Devices on hBN exhibit a significant temperature dependence that is usually not observed with graphene on oxidised silicon (on which the mobility is strongly limited by impurity scattering [61]). Prior to the realisation of samples on boron nitride, such a strong temperature dependence has been observed only for suspended graphene sheets. It has been shown furthermore that hexagonal boron nitride greatly reduces the presence of charge puddles in the graphene sheet, and that as expected its flatness is clearly improved [62].

Theoretical predictions made by Giovannetti *et al.* [63] showed that under certain conditions the boron nitride substrate could open a gap in the graphene band structure. Such a gap has not been observed experimentally so far. The non-ideal alignment conditions that cannot be avoided experimentally, in addition to the Moiré pattern generated by the lattice mismatch between the two sheets (not considered in the predictions) can explain the failure to observe a gap.

3.3.2 Transfer technique

To be able to use boron nitride as a substrate for graphene, we have to be able to transfer those micrometer size flakes. The sheets are first deposited on a resist layer spin-coated on a silicon wafer. This resist layer is removed and transferred onto the target wafer.

First, some pieces of silicon wafer are cleaned with a quite strong oxygen plasma ($P = 200$W). This will improve the wafer's flatness, and facilitate the removal of the resist. A layer of PMMA resist is then spin-coated on the wafer, but it should not be baked, otherwise the resist might be too difficult to remove later on. Boron nitride or graphene sheets are then deposited onto the resist layer by mechanical exfoliation, exactly as described in the "Graphene deposition" section. Hexagonal boron nitride crystals were supplied to our team by K. Watanabe and T. Tanaguchi from the National Institute for Materials Science (Tsukuba, Japan). Convenient sheets are then searched on the wafers and pictures are taken to memorize their location. Indeed, even if the wafer has markers they will become useless once the resist is removed from it. The edges of the PMMA layer are then scratched and the wafer is slowly put into water until the resist gets off the wafer. A metal holder is then put under the resist layer (held by a micro manipulator) while the water is slowly removed with a syringe. After drying, the metal holder is turned upside down and we proceed to the alignment with our transfer device in order to place the sheet above the desired location. This alignment is possible thanks to the transparency of the resist layer. We get the resist layer and the target wafer closer and closer while heating the target, in order to remove as much water as possible from the substrate. After a final alignment check, the resist layer is pushed to the wafer with a weak nitrogen gas flow and the heating is maintained in order to fix the PMMA to the new support. The wafer is then removed from our transfer device and put into aceton in order to dissolve the resist layer. The sample is then annealed to remove PMMA leftovers. The transfer procedure is summarized in picture 3.10.

3.3.3 Wafer preparation

In our study we have chosen to use a sapphire wafer instead of the usual Si/SiO$_2$ wafer. The ones we use are manufactured by Roditi International Corporation Ltd and have a C-plane orientation. Sapphire wafers ensure a good thermal conductance of the sample. With a resistivity of $10^{16}\Omega$.cm at room temperature, sapphire is an excellent insulator therefore local gates must be designed on the samples. Even if we do not take advantage of this aspect in this thesis, due to its high resistivity sapphire is a material of choice for measurements involving microwaves. We avoid this way charge and capacitance problems that can occur with a global gate. The non-conductive property of sapphire makes any lithography impossible if we do not add a conductive layer onto the resist. Before all lithography steps, we spin-coat a conductive polymer solution (Espacer 300Z) manufactured by Showa Denko K. K. The lithography is then performed as usual. The polymer simply has to be removed before the development, with distilled water.

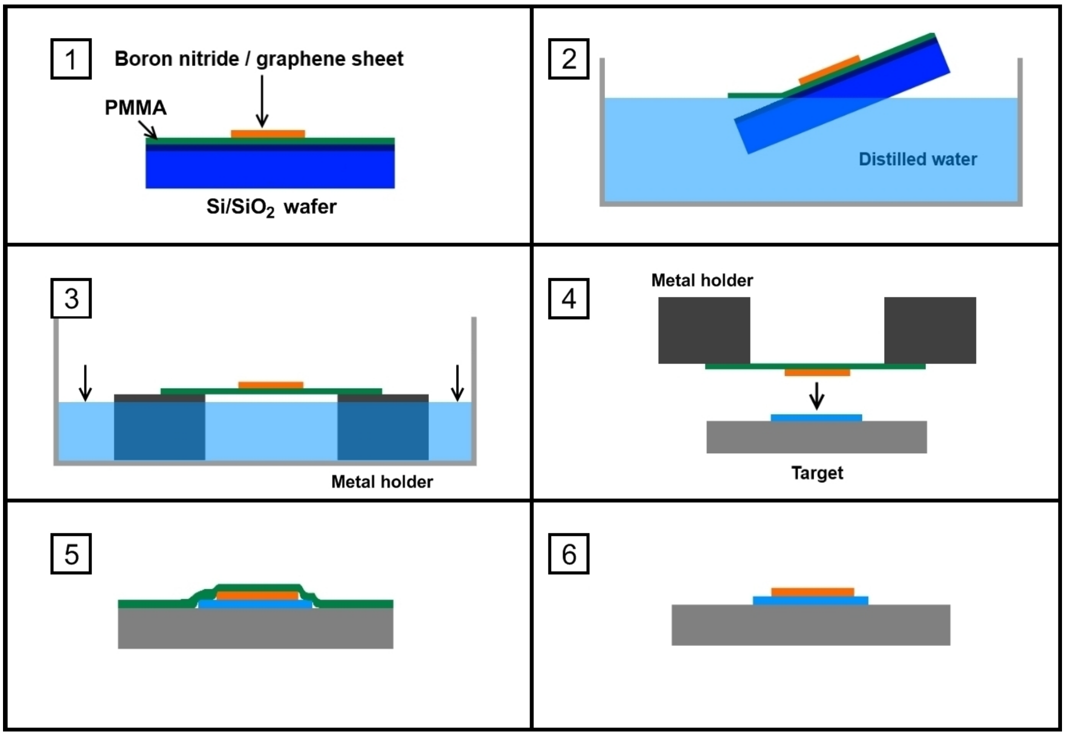

Figure 3.10: Transfer procedure step by step. 1: the graphene or boron nitride sheets are deposited on a layer of PMMA which spin-coated on a Si/SiO$_2$ wafer. 2: the wafer is slowly plunged into water, until the resist gets off. 3: the metal holder is placed under the floating resist layer, and the water is removed. 4: after drying, the metal holder is placed upside down and aligned to the target wafer. 5: the metal holder is bring closer to the target, and the resist layer is pushed to it with a weak nitrogen flow. 6: after dissolution in aceton, the transfer is done.

3.3.4 Back gate preparation

Unlike samples based on silicon wafers, sapphire cannot be used as a back gate, so an alternative must be sought. Two solutions are possible: we can pre-pattern lines of a few tens of micrometers width connected to sufficiently large pads that can be bonded to a sample holder, and perform a metal deposition. With this solution, the size of the gate can be tuned to be adequate with the typical size of a transferable boron nitride sheet, but the transfer will create a rather high step (several tens of nanometers) on the edges. This problem can be reduced by using thinner gates, but a minimum thickness is necessary to get a flat and homogeneous metal layer.

It is also possible to do a graphene deposition on the sapphire and look for a large enough few-layer graphite sheet that can play the role of the back gate. This way the "high step" problem is solved, and the atomically-flat nature of graphite sheets improves the gate's quality. The main drawbacks are the random sizes, geometries and environments of the obtained sheets, which can complicate further steps. The graphite sheet must not be too thin (so that the gate does tune the charge carrier density in the sample and not vice versa). The chosen sheet can then easily be connected in a further lithography step, usually the same step of the contact deposition.

Whatever the used solution is, we then have to transfer a boron nitride sheet on top of the metal layer or the graphite sheet. To perform this, we follow the procedure described in section 3.3.2. The typical linear dimension of used boron nitride sheets is around 50 µm, and the thickness ranges from 10 nm to 50 nm. The thickness of the boron nitride sheets is at first determined with their transparency, and measured later with an atomic force microscope.

3.3.5 Graphene transfer

A bilayer graphene sheet can be prepared on top of a PMMA layer as described in section 3.1.2 and be identified by Raman spectroscopy. Graphene is usually harder to find optically than on Si/SiO_2 wafers, the contrast is indeed significantly reduced by the additional resist thickness. However, Raman spectroscopy is as efficient, since the G and 2D peaks are not perturbed by the PMMA substrate. The sheet is then transferred on the top of the boron nitride substrate as described in section 3.3.2.

Because they are subject to bending during the process, the transferred graphene sheets are never perfectly flat: they usually exhibit some wrinkles and bubbles (figure 3.11a and 3.11b). Annealing the sample again can reduce those problems and increase the size of the flat domains (and clean the sheet from PMMA residues too). Even with this additional step, most of the flat domains have a relatively small size (up to a few micrometers). To connect the graphene sheet, we have to avoid those wrinkles (if there is a domain large enough) or to remove some parts of the sheet so that there is only a flat region left. This can be done with a soft oxygen plasma etching step ($P = 30$ W), by using PMMA resist as a protective layer. One simply has to proceed with lithography and develop the areas where the graphene has to be removed.

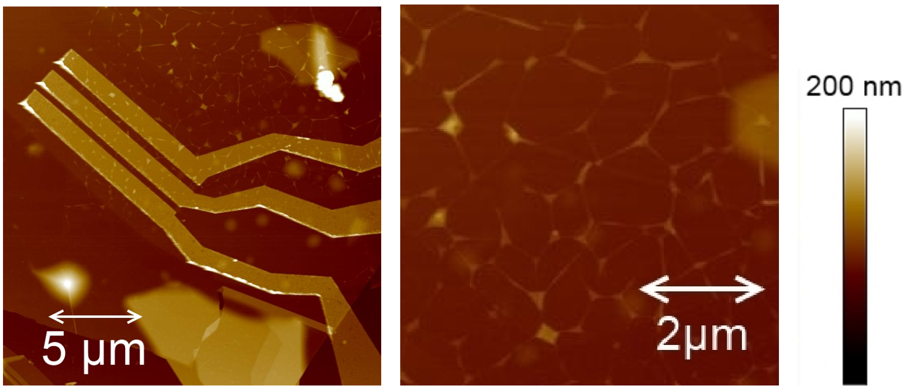

(a) (b)

Figure 3.11: (a) AFM picture of a connected bilayer graphene sheet transferred on top of a graphite type back gate (b) Zoom on the area where wrinkles and bubbles are present.

3.3.6 Electrode deposition

The electrodes are deposited with the procedure described in section 3.1.5. Depending on the thickness of the back gate, depositing more metal than the usual quantity can be necessary. Because the transfer technique was mainly used to produce double-gated bilayer graphene sheets, the design of the top gate must taken into consideration from the beginning. In this case, it is preferable not to have very close contacts in order to facilitate further alignment steps (especially in the case of local top gates). Contacts of 350 nm distance are then designed, which is short enough to observe an induced supercurrent. Figure 3.11a presents a connected bilayer graphene sheet, that has been transferred on top of a graphite/hBN back gate.

3.4 Top gates

In order to open a gap in the bilayer graphene samples, we have to design a top gate in addition to the already present back gate. Two procedures have been considered, the first one consists of transferring a second boron nitride sheet on top of the sample, and the second one consists of the growth of an oxide layer by an atomic layer deposition process.

3.4.1 Boron nitride sheet

One way to design a top gate is to transfer a boron nitride sheet on top of the sample by following the same procedure as previously. One drawback of this choice is that the hBN sheet might be partially suspended on top of the contacts. In addition, the boron nitride sheet thickness and geometry can not be precisely controlled. If some residues are present on the sheet, they might be trapped between the hBN and graphene sheets, inducing additional doping or scattering centers to the sample.

On the other hand, the transfer process is rather fast. Because hBN is a perfect crystal, relatively high voltage can be applied and the risk of leakage is rather low. If the sheet is in contact with the graphene we keep the benefits of its hexagonal structure.

3.4.2 Atomic layer deposition

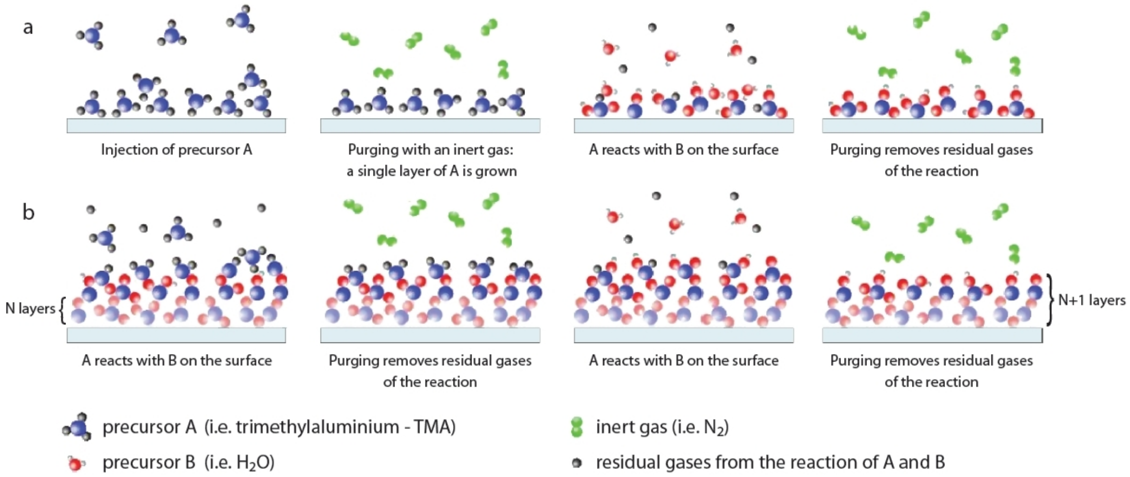

Figure 3.12: Summary of the ALD process. The first precursor (trimethylaluminium or TMA) is injected and adsorbed by the substrate surface. The residual molecules are then evacuated with an inert gas (N_2). The second precursor is injected (H_2O), reacting with the first one and leading to the generation of a layer of Al_2O_3. The chamber is evacuated again, and a new cycle can begin.

The other considered way is to deposit a layer of Al_2O_3 through an atomic layer deposition (ALD) process. First, a layer of PMMA resist is spin-coated on the sample.

The PMMA is then removed on the area around the sample with a standard electron-beam lithography. Unlike the boron nitride case, the target area can be precisely controlled. Because graphene is hydrophobic, starting the process from this point may not lead to a good-quality layer. A simple solution to this problem has been proposed by Kim *et al.* [64]. 2 nm of aluminium are then deposited on the wafer, by using the same UHV device as for the contacts. The aluminium is instantaneously oxidised when exposed to air. The resulting oxide layer will be used as a nucleation layer for the following reactions. The process consist then on a repetitive set of chemical reactions detailed on figure 3.12. The number of cycles determines the oxide's final thickness, which is then precisely controllable (theoretically to $\approx$ Å resolution).

The growth of an oxide layer is more likely to reduce the sample's quality than the transfer of a boron nitride sheet. The charge carrier mobility is usually significantly reduced. Losses of around 30% are regularly reported. The leakage risk is higher too, the resulting dielectric having a relatively low breakdown voltage.

3.4.3 Metal deposition

Whatever the chosen solution is, the top gate can then be lithographied over the boron nitride sheet or the aluminium oxide. To minimize the risk of leakage with the contacts, the top gate is placed between them if it is possible (in a fork structure when more than two contacts are available on the same graphene sheet). A scheme of a complete dual-gated bilayer graphene device is shown on figure 3.13.

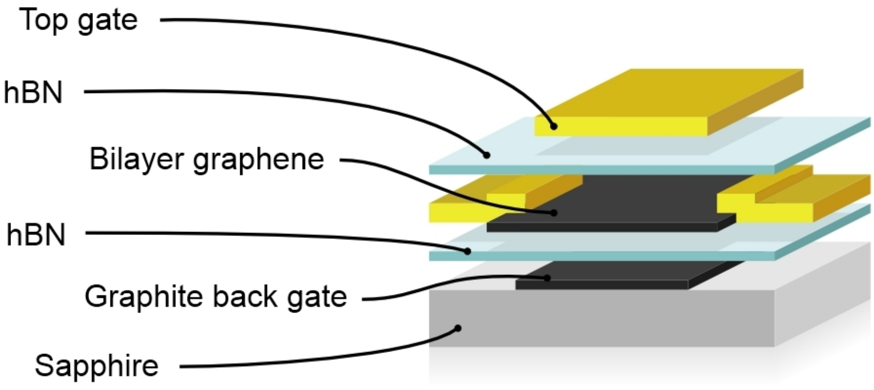

Figure 3.13: Final structure of a double-gated bilayer graphene sheet.

Chapter 4

Measurement techniques

Once the samples are designed, they have to be characterised in an appropriate experimental setup. Measurements are performed either at room temperature with a probe station, or at low temperature in a cryostat. These experimental setups are presented in a first section. As filtering is critical for measurements at cryogenic temperatures, the designs and characteristics of the filters used are detailed in a second section.

4.1 Experimental setups

4.1.1 Room temperature probe station

Before performing measurements at low temperature, it is necessary to check the resistance of the device at room temperature. These tests are performed after each fabrication step of the sample. This provides us a hint on its quality.

The gate voltage is set by a power supply (Keithley 2400 SourceMeter). The sample is firmly screwed to a copper plate. For silicon-based samples, this ensures a good connection between the copper and the conductive silicon. In this case the source meter just has to be connected to the copper plate. For sapphire-based samples, we have to use a metal tip to connect the source meter to the metallic gate. If the sample contains two gates, they are studied separately. The second gate is grounded with another metal tip to avoid any charging effect. The resistance is measured with two lock-ins (eg&g 5210 and SR830 manufactured respectively by Princeton Applied Research and Stanford Research Systems).

Lock-in amplification is based on a phase detection technique and can extract signals from a noisy environments. Let us consider the AC signal $A_D \cos(\omega_D t + \theta_D)$ that need to be detected. It is measured by a lock-in and multiplied by a carrier $A_R \cos(\omega_R t + \theta_R)$. The resulting signal is $\frac{A_R A_D}{2}[\cos((\omega_R - \omega_D)t + \theta_R - \theta_D) - \cos((\omega_R + \omega_D)t + \theta_R + \theta_D)$. The AC component of this signal is then removed by integration with a low-pass filter. The integration time is adjustable and must be significantly higher than the period of the carrier. A DC component $\frac{A_R A_D}{2} \cos(\theta_R - \theta_D)$ remains only if $\omega_R = \omega_D$. By taking the frequency of the signal that we want to measure as the reference, it is then possible to detect it even in a highly noisy environment.

One of the lock-ins provides an AC voltage at low frequency (a few tens of Hertz), which is reduced by passing through a voltage divider. The frequency of this voltage signal is used as a reference for the two lock-ins. The signal is then injected to the graphene sheet through two metal tips. The output current is preamplified and one of the lock-ins detects the AC current corresponding to the excitation frequency. Its amplitude corresponds to the differential current dI. Because of the voltage divider, the voltage drop across the sample is not the one setted on the lock-in providing the excitation. The effective differential voltage dV is then preamplified and measured as well by the second lock-in.

The measurement being made at zero bias (the AC voltage is applied without any DC component), $R = dV/dI$. A schema of the setup is presented on figure 4.1a. A typical measurement of the resistance of a graphene sample as a function of the gate voltage can be seen on figure 4.1b. Because the measurement is not made in vacuum, some molecules are adsorbed by the graphene sheet. This leads to an additional doping that shifts the voltage corresponding to the Dirac point away from $V = 0$. An hysteresis is present due to the polarisation of trapped charges in the substrate.

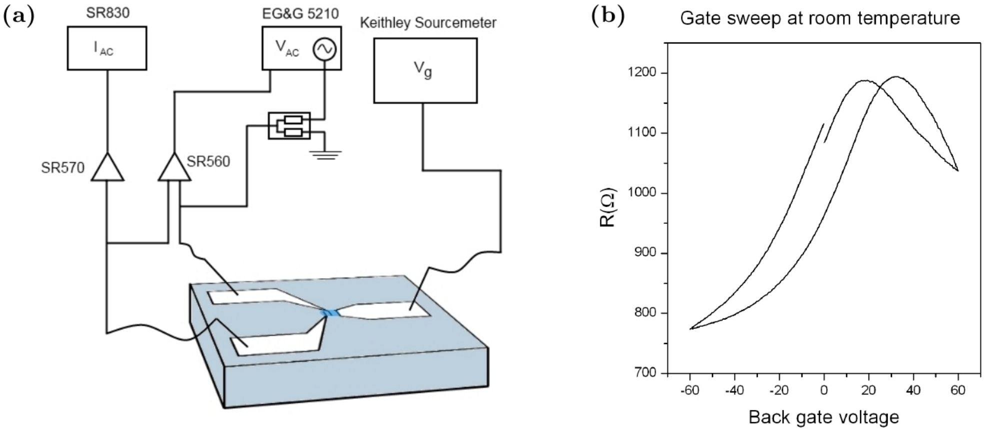

Figure 4.1: (a) The room temperature setup. An alternative excitation is injected to the sample, and the resulting dI and dV are read by the lock-ins after preamplification. A voltage sourcemeter controls the gate voltage. (b) Example of measurement performed on a silicon-based sample, at room temperature.

4.1.2 Measurements at cryogenic temperatures

The first measurements at low temperature of this thesis have been performed in the Kelvinox 100 cryostat of Dr. D. Beckmann's group (KIT - INT), manufactured by Oxford Instruments. In late 2012 our team acquired a LD250 dilution refrigerator manufactured by BlueFors (showed on figure 4.3b). As a consequence this section focuses on the measurement setup built around this cryostat.

Dilution cryostats are based on a property of ^{4}He/^{3}He mixtures. Figure 4.2 shows the corresponding phase diagram. Below 0.8 K (or less, depending on the ^{3}He concentration), the mixture divides into two phases: one ^{3}He rich phase (the concentrated phase), and one ^{3}He poor (the dilute phase). Because the enthalpy of ^{3}He is smaller in the concentrated phase than in the dilute phase, moving atoms from the first phase to the second requires energy. This energy can be heat from the environment.

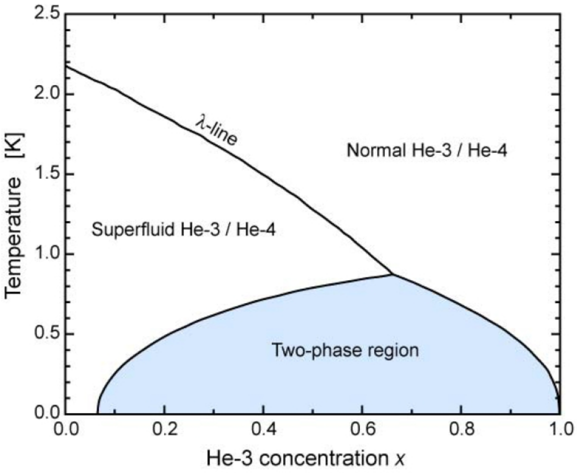

Figure 4.2: ^{3}He / ^{4}He phase diagram at low-temperature.

Figure 4.3a shows how this phenomenon is exploited in the dilution cryostat. A concentrated and pre-cooled ^{3}He/^{4}He mixture is injected into the system. At the output (the still), the mixture is pumped, resulting in an evaporative cooling. This step can reduce the temperature bellow 0.8 K. The two phases can then appear. The dilute phase being heavier, it moves to the bottom of the system. ^{3}He having a much higher partial pressure than ^{4}He, the evacuated vapor at the still is mainly pure ^{3}He. The pumped mixture is continuously reinjected, allowing ^{3}He atoms to move from the concentrated phase to the dilute phase. This cools down the mixing chamber as the phase separation is located there. A heat exchanger cools the injected ^{3}He, by transferring its heat to the upward-going, cold and dilute ^{3}He. This ensures that as much cooling power as possible is used to actually cool the mixing chamber. The cooling cycle can operates continuously, and the low temperature stage fixed to the mixing chamber (on which the samples are located) can reach a temperature of $T \sim 7$ mK.

Our cryostat is equipped with a pulse tube refrigerator able to cool the system down to a low enough temperature for the cycle described previously to begin. The system works in closed circuit and does not need to be refilled with helium unlike most dilution cryostats.

The sample is fixed on a sample holder with GE varnish which tolerate cryogenic temperatures. Bonding wires connect electrodes and gates to the sample holder. The sample holder itself has to be connected to the measurement instruments outside of the cryostat from the low-temperature stage. Twisted pairs of wires are employed to reduce electromagnetic interferences (EMI). The material used for these wires is

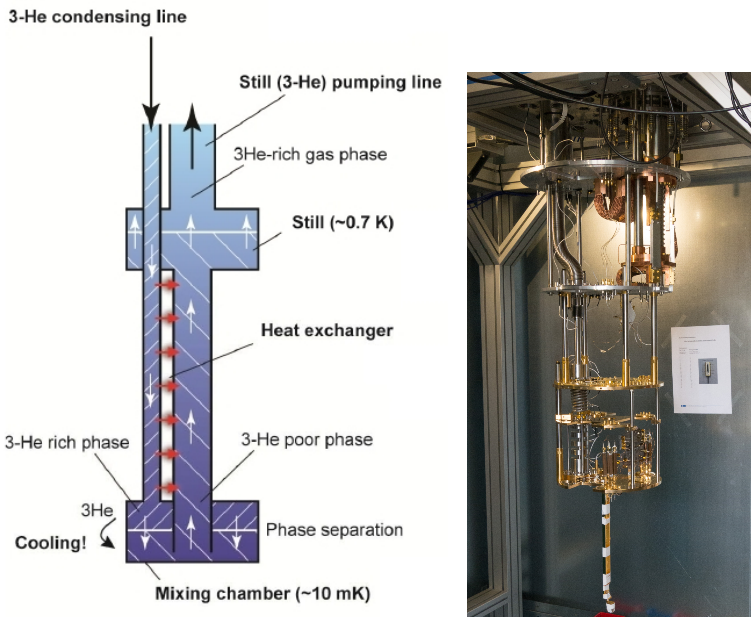

(a) **(b)**

Figure 4.3: (a) Schema of the cooling part of the BlueFors cryostat, adapted from the manual. (b) picture of the opened actual device.

a phosphor bronze alloy insuring both a sufficient electrical conductivity and a low thermal conductivity. Filters are placed before the sample holder to prevent the noise coming from the room temperature cables and devices to reach the samples through the wires. Their realisation is detailed in the next section. Radiation shields are present in the outer part of the cryostat and in a vacuum space to prevent heating from black body radiation and thermal conduction.

The instruments used for the measurements are two lock-ins SR830, a voltage preamplifier SR560 from Stanford Research Systems, a current preamplifier 1211 from DL Instruments, two multimeters 34410A from Agilent and a BILT BE2101 DC voltage source from iTest. As in the room temperature setup described in section 4.1.1, an AC voltage is provided by one of the lock-ins. A low-noise DC voltage provided by the Bilt source is added to this AC excitation signal, as presented on the diagram showed on figure 4.4. With this configuration, we can perform either DC only measurements (with the amplitude of the AC signal set to zero), measurements of the differential resistance at equilibrium (without any DC bias present), and measurements of the differential resistance out of equilibrium (if the sample is biased by a DC component in addition to the AC one).

The resulting current is injected to one of the sample's contact. The output current is preamplified and measured by a lock-in (for the AC component) and a multimeter (for the DC component). Two additional lines measure the voltage drop across the sample the same way. With this four point-like configuration we can get rid of the resistances of the wires and filters.

A superconducting magnet is placed at the bottom of the cryostat. The position of the sample is determined so that it coincides exactly with the center of the generated magnetic field. Two different magnets are available, and continuous magnetic fields up to 12T can be generated with the larger one (200 mT for the smaller one). For temperature dependence measurements, heating can be provided by a resistor. Tuning the current going through it changes the equilibrium temperature of the stage.

The devices are connected to a single computer through GPIB cables. To isolate electrically the computer from the measurement devices, an optical fiber is employed. Electrical devices are isolated from the network through transformers. Most of the measurement operations are automatised with scripts.

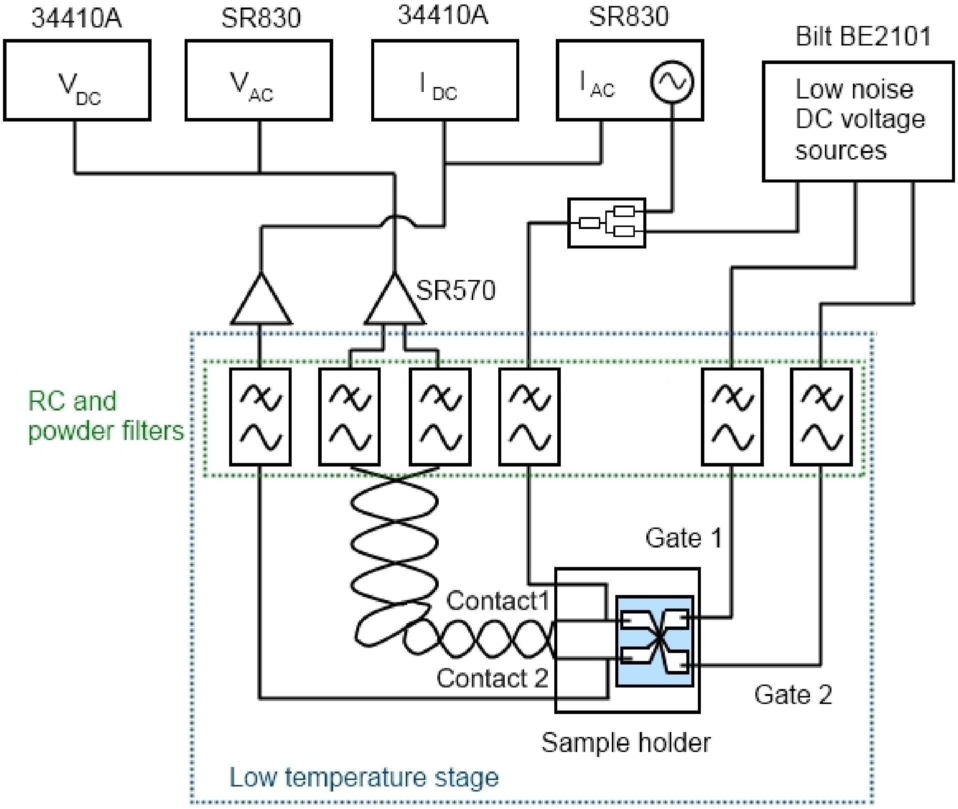

Figure 4.4: Schema of the circuit used for low-temperature measurements.

4.2 Filters

Without filtering, noise from the warmer cables and instruments outside of the cryostat can reach the sample through the measurement lines. This noise can increase the

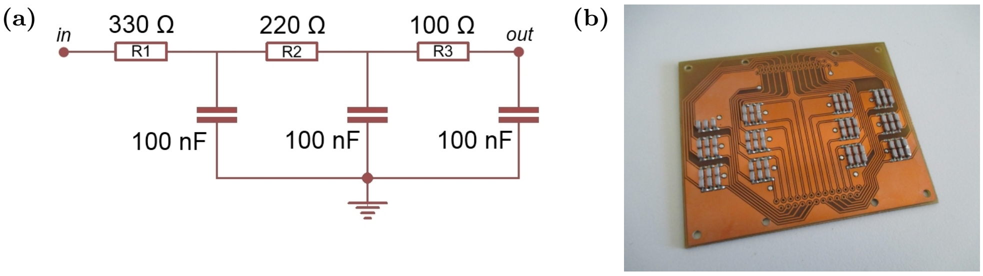

Figure 4.5: (a) Electric diagram of the triple-stage RC filters. The values are those indicated by the manufacturer and are temperature-dependant, especially for the resistors. (b) Picture of a populated printed circuit board (23 lines).

electronic temperature and in our case prevent the observation of an induced supercurrent. Higher frequencies than the ones used for the actual measurements should then be filtered. Different types of filters can be used. A non-exhaustive list of possible filters would include RC filters, LC filters, Thermocoax cables [65], shielded twisted pair filters [66, 67], metal powder filters [68], micro-filters on chip [69, 70], etc.

Each type of filter has its own domain of efficiency. If a large frequency spectrum has to be filtered, combination of several ones is usually employed. A comparison by Bladh *et al.* concluded that a combination of either RC, RCL or LC filters with either Thermocoax cables or metal powder filters covers a wide frequency spectrum and would be suitable for most cryogenic experiments [71].

We chose to use three-stage RC filters to filter the low frequencies ($f > 1$ KHz), and stainless steel powder filters for microwaves ($f > 1$ GHz). The twisted pair wires employed for the measurement lines are expected to filter intermediate frequencies (roughly after 100 MHz [67]), but in our measurement setup this has not been characterised so far.

4.2.1 Low pass RC filters

Our RC filters consists of a three-stage classic resistor and capacitor circuit. The electric diagram is shown on figure 4.5a. The transfer function of such a filter is:

$$H = \frac{1}{1 + Cjw\underline{Z_1} + (Cjw)^2\underline{Z_2} + (Cjw)^3 R_1 R_2 R_3} \tag{4.1}$$

With $\underline{Z_1} = 3R_1 + 2R_2 + R_3$ and $\underline{Z_2} = 2R_1R_2 + 2R_3R_1 + R_2R_3$. For our values, the theoretical cut-off frequency at -3 dB is 1 kHz. To minimize the space needed for those filters, surface mount components are used. At $T = 4.2$ K, the resistance of the used components increases from 20% to 30%. Preliminary measurements performed by Oliver Krömer and Lars Petzold from the Institute for Data Processing and Electronics (KIT) showed that only capacitors with NP0 (Negative-Positive zero) class dielectrics are suitable for cryogenic applications. At $T = 4.2$ K, the capacitance changes by less than 1%. The cutoff frequency at this temperature according to these measurements is about 880 Hz. The finished, populated printed circuit board (PCB) can be seen on picture 4.5b. Emplacements for connectors (norm MIL-C-83513) are present on each side of the board.

Figure 4.6a and 4.6b show the gain of the designed RC filters at room temperature and at 50 mK, measured respectively with a Bode 100 (manufactured by Omicron Lab) covering the low-frequency range and with another vector network analyzer manufactured by Rohde & Schwarz covering frequencies up to 6 GHz. At room temperature, the gain follows closely the theoretical one determined from equation 4.1 up to f = 150 kHz. The cutoff frequency at -3dB is 1050 Hz. To characterise the filters at low temperature, they are placed inside the cryostat. Additional attenuators are present in order to avoid radiations from room temperature to reach the filters. They affect the cutoff frequency and the initial gain. From room temperature to 50 mK the cutoff frequency (defined here by $G(f_c) = G(f_0) - 3$ dB, with f_0=10 Hz) is reduced by 38.1 % (from 5575 Hz to 3450 Hz). Applying this reduction as a rough approximation for the filter alone leads to a cutoff frequency of 650 Hz at 50 mK, which is lower than the calculated 880 Hz at 4 K but still from the same order of magnitude. For frequencies higher than ~ 5 MHz, the filter does not operate properly as it cannot stop high frequency radiation.

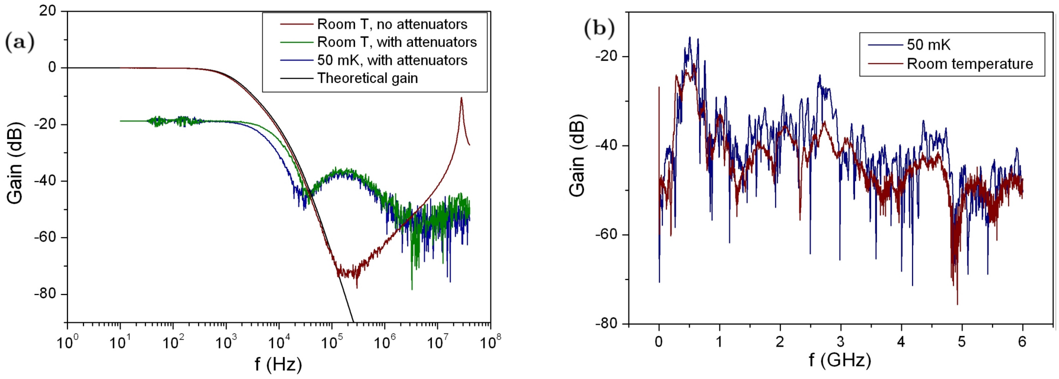

Figure 4.6: Characterisation of the RC filters at room temperature and at 50 mK from 10 Hz to 40 MHz (a) and from 9 kHz to 6 GHz (b).

In our experiments, the measurements are performed with lock-ins which use a low-frequency voltage as an excitation signal (as described in section 4.1.1). The working frequency f_L of the lock-ins must be set one or two orders of magnitude below the cut-off frequency of the RC filters, otherwise excitation and measured signals will be affected by the filtering. The other filters present in our system are efficient only at much higher frequencies and therefore do not affect the lock-in detection. This has an incidence on the measurement time: ideally the integration period of the lock-ins should be much higher than the period $1/f_L$ of the excitation signal. During our measurements at T=7 mK, a frequency of 7-8 Hz is used, with a measurement time of 300 or 1000 ms. At slightly higher frequencies (around 30 Hz), a non-negligible part of the signal is already out of phase.

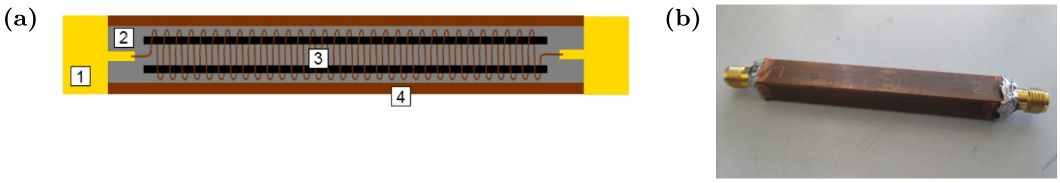

Figure 4.7: (a) Diagram of a single stainless steel powder filter, consisting of a long copper wire rolled around two Stycast rods into an infinite schema (3), connected to two SMA connectors (1) and placed into a copper case (4) filled with stainless steel powder (2). (b) Picture of a finished individual stainless steel powder filter.

4.2.2 Powder filters

To filter higher frequencies ($f > 1$ GHz), we employ powder filters. The first of its kind has been designed by Martinis *et al.* in 1987 [68]. Powder filters consist of a rolled wire going through a metal tube filled with metal powder, copper and stainless steel powder being the most employed ones. Bronze powder can be used too [72]. The attenuation is caused by skin-effect damping in individual grains. According to the literature, using stainless steel is more efficient [73, 71, 74]. This is believed to be due to the higher resistivity of the stainless steel grains. In this thesis, we use stainless steel powder provided by Alfa Aesar, of mesh -325 (which means that the diameter of the grains is below 44 µm). In order to avoid any trouble within the cryostat while using the magnet, magnetic materials should be avoided. As the powder used here is only slightly magnetic and as the location of the filters is several tens of centimeters away from the magnetic field center, we do not expect any problem. To ensure a good connectivity by reducing radiation at high frequency and to facilitate the characterisation of the filters with radio-frequency instruments, we use coaxial RF SMA connectors.

Our first powder filters are made inside copper square tubes of 7 cm length, with 4x4 mm^2 side space available inside. For each tube, a pair of rods made of a mixture of Stycast epoxy and stainless steel powder are realised. The wire (around 1.4 m) is rolled upon those two rods alternatively (like presented on figure 4.7a), in order to save space. A SMA connector is soldered to one side of the wire, and then the system is inserted into the copper tube. Some Stycast epoxy is used again to fix the SMA connector to the tube and to make the corresponding side impermeable to powder. Subsequently the tube is filled with stainless steel powder. During the process, the system is slightly shaken regularly and then pressed to the walls of an ultrasonic bath to optimize the filling of the tube with the powder and densify it. A few millimeters are left to fix the second SMA connector with Stycast, soldered previously to the second wire extremity. To properly ground the device, the external parts of the SMA connectors are soldered to the tube. Made this way, the filters are not exactly symmetric, usually more Stycast is used to fix the second SMA connector. A diagram and a picture of a filter are presented on figures 4.7a and 4.7b. The filters are then characterised with a vector network analyzer manufactured by Rohde & Schwarz.

For most of the filters produced, the signal reaches the floor noise of the measurement device at around 2.5 GHz at room temperature (figure 4.8). The reproducibility is rather good. The asymmetry is almost imperceptible and does not cause any problem for our utilisation. According to Fukushima *et al.*, the attenuation is normally less efficient at cryogenic temperatures (but stainless steel powder filters are less temperature dependant than copper powder ones though) [73]. The resistance of our individual powder filters is $R = 3,84 \pm 1.5\ \Omega$.

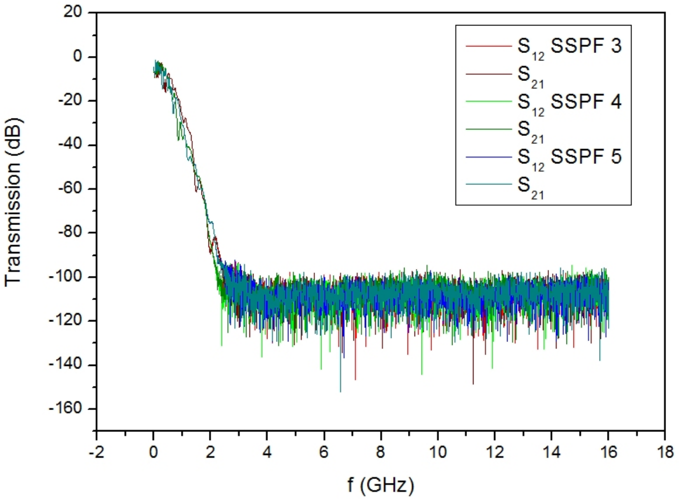

Figure 4.8: Characterisation of some individual stainless steel powder filters.

To be able to exploit a large number of lines, a second set of filters is designed, inspired by those made by Mueller *et al.* [75]. This time a PCB is used. Long lines playing the role of the wires are designed across the board. The lines are coupled to simulate a twisted pairs like behavior. 24 lines of 3 m length are supported on a 13x13 cm^2 board (figure 4.9). They are soldered to MIL-C-83513 connectors, so that the filters can be plugged directly before the RC filters. To be able to use both sides of the PCBs, the powder is mixed with Stycast (1/1 proportion in volume). The mixture is then deposited and baked on the two sides, one after the other. A large amount of lines being covered in a single step, this method of production is much less time-consuming than the previous one. The resistance of the powder filters designed on PCB is $R = 43 \pm 1\ \Omega$. This is higher than the resistance of the individual filters ($R = 3,84 \pm 1.5\ \Omega$) but the reproducibility is better.

A filter is then characterised with a vector network analyzer at room temperature and at 50 mK. The same attenuators used for the characterisation of the RC filters are present. Their attenuation (-27 dB) is added to the filter one during the measurement. As the noise floor of the measurement device is located at $\sim$ -100 dB, the effective attenuation from the filter can be measured down to -70 dB only. Figure 4.10 shows the deducted gain. We notice that up to 2 GHz the performance of the filters is slightly reduced at low temperature. This can be attributed to the lower resistivity of the stainless steel grain. An attenuation around -70 dB is achieved at $f > 3$ GHz at

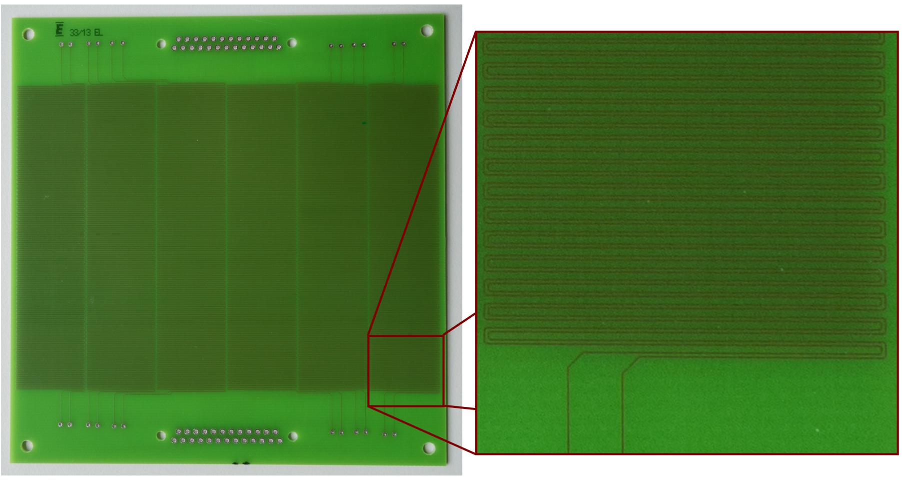

Figure 4.9: Optical picture of the PCB designed for stainless steel powder filters. The lines play the role of the wires in the previous filters.

50 mK. The real attenuation is probably higher but can't be measured as explained previously.

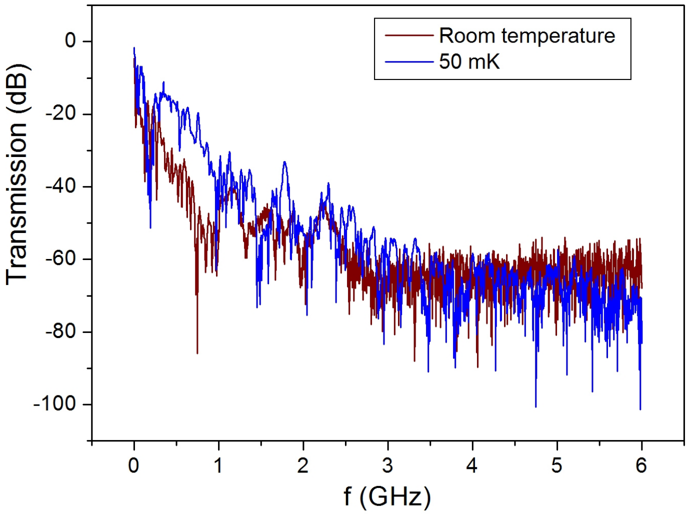

Figure 4.10: Characterisation of the stainless steel powder filters designed on PCB, at 50 mK and at room temperature.

Chapter 5

Short superconductor-graphene-superconductor junction

This chapter presents the study of a superconductor-graphene-superconductor junction with a short length L designed by shadow evaporation. The objective is to observe an induced supercurrent in graphene in the ballistic regime.

5.1 Introduction

Even though several experiments have already been done in superconductor-graphene-superconductor (SGS) junctions, the possibility to observe a ballistic regime in such junctions is still under debate. According to the theoretical predictions of Titov *et al.* [38], a ballistic regime would be characterised by a critical current linearly dependent on the Fermi energy away from the Dirac point:

$$I_c = 1.22\frac{e\Delta_0}{\hbar}\frac{E_f W}{\pi\hbar\nu} \tag{5.1}$$

with Δ_0 the gap of the superconductor, ν the Fermi velocity in graphene and W the width of the junction. The product of the critical current with the normal resistance of the junction, I_cR_N, is expected to evolve from $2.08\Delta_0/e$ around the Dirac point to $2.44\Delta_0/e$ away from it.

In the first study of a SGS junction reported by Heersche *et al.* [43], an I_cR_N product $\sim \Delta_0/e$ has been observed which is already of the right order of magnitude but still lower than the expected value for a ballistic junction. In reference [45] the junction was clearly identified as diffusive, as the extracted mean free path is one order of magnitude smaller than the junction length and the I_cR_N product three times lower than the ballistic value. In the experiment [49], where PbIn was used for the superconducting electrodes, the I_cR_N was as low as $0.23\Delta_0/e$. More generally, most of the experiments performed on silicon wafers agree only qualitatively with the theoretical predictions and lead to a product of at best two times lower than the ballistic limit.

Mizuno *et al.* [56] investigated a suspended graphene Josephson junction and claimed that it is in the ballistic regime. This assumption is mainly based on the linearity of the measured critical current relatively to the Fermi energy at high charge-carrier density. The $I_c R_N \sim \frac{1}{3}\frac{\Delta}{e}$ product is still below the expected value though. This result is attributed to imperfections in the superconductor-graphene interfaces and to the sample geometry, which poorly satisfies the condition $L \ll W$.

Another way to get closer to the ballistic regime would be to design shorter junctions. From a classical point of view, the mean free path of the electrons l may thus get larger than the junction length L.

Here, we try to design ultra-short superconductor-graphene-superconductor junctions by using the shadow evaporation technique described in section 3.2.

5.2 Device characterization

The measurements are performed on the top contact pair of the sample visible in figure 5.1a. The graphene sheet is connected to Ti/Al (5 nm/40 nm) electrodes, on top of a Si/SiO$_2$ wafer used as a back gate. The junction length is $L = 120$ nm, its width W is 3 µm long. The geometry satisfies then the condition $W/L \gg 1$ with a ratio of 25. With the thickness of the gate dielectric $d = 300$ nm, we have a ratio L/d of 0.4. As the gate dielectric thickness is not negligible compared to the junction length, it is not possible to use the parallel plate capacitor approximation which requires $L \gg d$. Because there is no straightforward way to calculate analytically the gate capacitance without this approximation, we use numerical calculations. By modelling the junction in the software COMSOL Multiphysics, a gate capacitance per surface area of 11.6 µF.m^{-2} is evaluated. The contacts strongly suppress the effect of the gate as the theoretical value in the parallel plate approximation is 112 µF.m^{-2}.

Figure 5.1b shows the resistance of the sample as a function of the back gate voltage at room temperature and at 4.2 K. We notice that the Dirac peak of the resistance is slight sharper at 4.2 K.

5.3 Induced supercurrent

The next measurements are done at 50 mK while the sample is driven out of equilibrium with a current bias to the electrodes. Figure 5.2 shows some *I*-*V* curves recorded at various back gate voltages. We notice that the current flows without resistance below a critical current I_c: this is a direct observation of the proximity induced superconductivity.

Figure 5.3a shows a differential resistance map as a function of the gate voltage and the current bias. For comparison, figure 5.3b shows a similar measurement extracted from reference [43]. At low current bias, the differential resistance is null. We notice that at I=57 nA, the sample switches to a resistive state. This happens independently

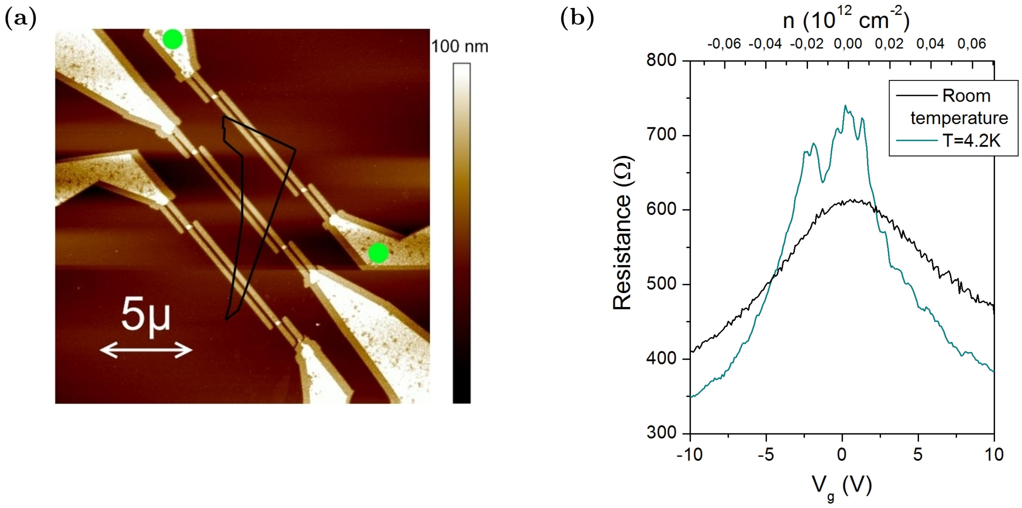

Figure 5.1: (a) Atomic force microscope picture of the sample. The position of the graphene sheet is highlighted. Green dots are added on the measured contact pair. (b) Resistance of the sample as a function of the gate voltage, at room temperature and at 4.2 K. Aperiodic conductance fluctuations due to random quantum interference of electron waves can be observed.

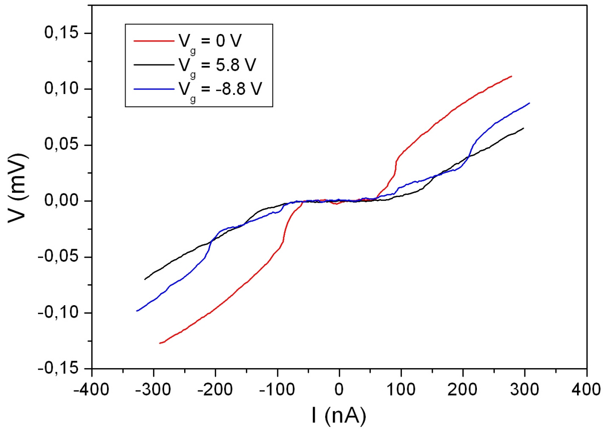

Figure 5.2: $I - V$ curves, measured at T=50mK.

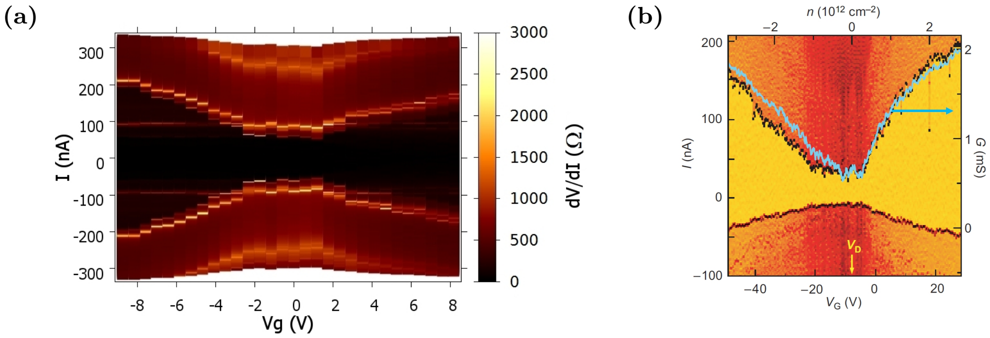

Figure 5.3: (a) Differential resistance as a function of the gate voltage and current bias. The black area corresponds to the superconducting state. (b) Analogous measurement of [43], for comparison. The yellow area corresponds to the superconducting state.

from the gate voltage. The differential resistance of the device between I=57 nA and the sharper jump present at higher current bias is independent of the gate voltage as well. It is in addition way lower than the expected normal state resistance of the junction. The origin of this premature switching to resistive state is unclear, but the gate independence and the low resistance suggest that this finite differential resistance is not due to a current flowing through the graphene sheet.

Figure 5.4a shows the critical current of the SGS junction as a function of the gate voltage, defined by the sharper differential resistance jump visible on figure 5.3a. The gate voltage has a strong effect on the measured critical current. At higher charge carrier density a larger supercurrent can flow through the graphene sheet before the SGS junction switches to a resistive state. The critical current stays finite while we tune the gate voltage from negative to positive values: not only can the supercurrent be carried by both hole or electron Cooper pairs, but it even does exist when the Fermi energy reaches the Dirac point where the density of states vanishes. The presence of a finite supercurrent at the Dirac point has been theoretically predicted in reference [38] and observed in most of the reported experiments involving SGS junctions.

Figure 5.4b shows the temperature dependence of the critical current at $V_g = -2.6$ V. As the superconducting gap Δ decreases with the temperature, the critical current is reduced. The results are fitted with a Kulik-Omel'yanchuk model in the dirty limit (described in section 2.2.1.5). The superconducting gap parameter used is $\Delta = 67$ µeV. This value is consistent with the superconducting gaps measured by other groups with similar Ti/Al electrodes on graphene (from 55 to 125 µeV in references [44, 43, 47, 45])

Figure 5.5a shows the differential resistance as a function of the voltage bias applied to the electrodes for various values of the back gate voltage, and figure 5.5b shows the differential conductance as a function of the bias voltage V. We expect to see conductance peaks at $2\Delta/ne$ bias voltage due to the multiple Andreev reflection, independent of the gate voltage. The structure that we observe is not gate-independent. This is due to the premature switching to the resistive state observed previously on figure 5.3a:

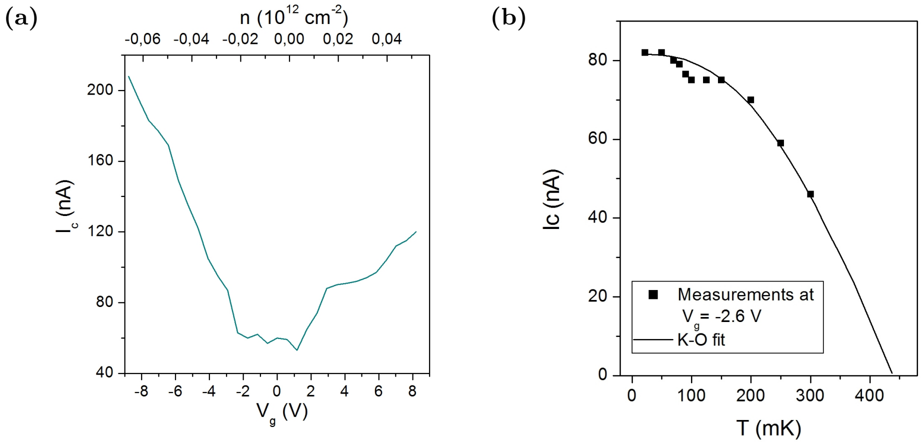

Figure 5.4: (a) Critical current of the junction as a function of the gate voltage. (b) Temperature dependence of the critical current, for $V_g = -2.6$ V.

from I=57 nA to $I = I_c$, a slight resistance is present. The voltage difference is increased on this interval, shifting the bias voltage position of the features observed at $I > I_c$. As I_c is gate-dependant but not the current at which this switching occurs, the voltage shift is gate-dependent. As a consequence the multiple Andreev reflection structure cannot be identified properly.

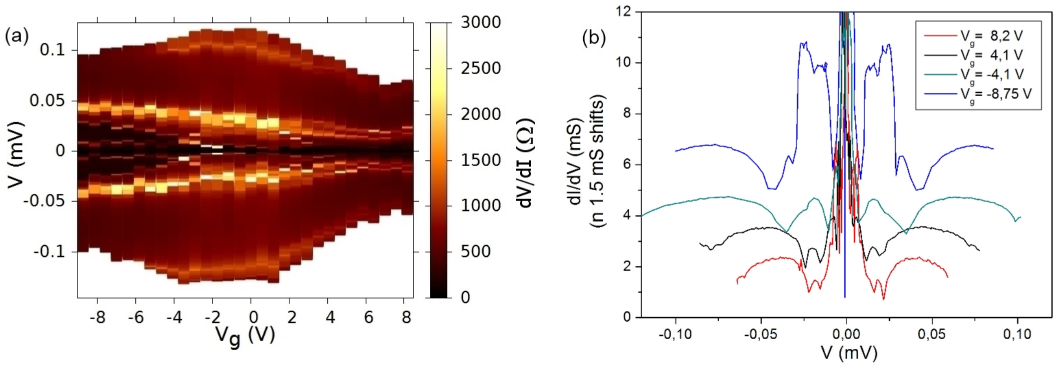

Figure 5.5: (a) Differential resistance as a function of the bias voltage V and the gate voltage V_g. (b) Differential conductance as a function of the bias voltage V for various values of the gate voltage V_g.

5.4 Fraunhofer pattern

Figure 5.6 shows a differential resistance map as a function of the magnetic field and the current bias. As the sample consists of a rectangular and homogeneous junction, we expect to observe a Fraunhofer pattern as described in section 2.2.1.4 with a periodicity of $\Phi_0/WL = 5.74$ mT for the oscillations according to the sample's geometry. The oscillations are barely visible, yet darker spots are present at B=9.5 mT, 14.5 mT and 20 mT. This leads to an average period of 6.7 mT which is in a relatively correct agreement with the expected value. The fact that the proximity induced supercurrent is properly established only for the first oscillations can be attributed again to the premature switching to resistive state observed previously.

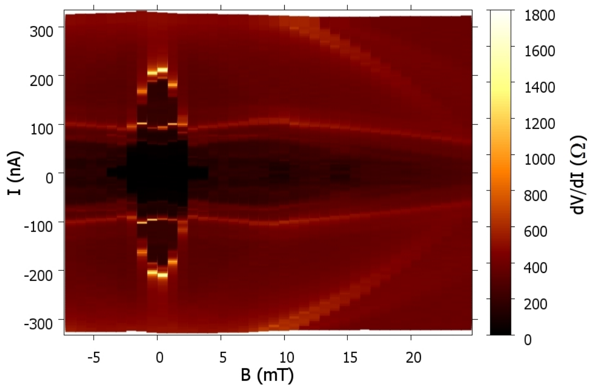

Figure 5.6: Differential resistance versus magnetic field (step : 0.8 mT) and current bias, at $V_g = -8$ V.

5.5 Regime

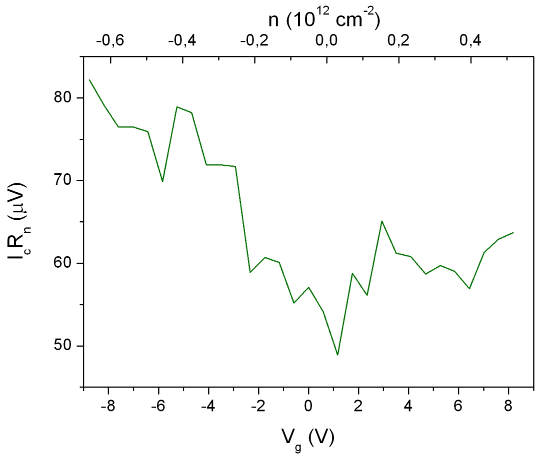

Figure 5.7: I_cR_N product as a function of the gate voltage.

The normal state resistance of the sample is measured in the presence of a 100 mT magnetic field perpendicular to the graphene sheet and for several back gate voltages. The resulting product I_cR_N is presented on figure 5.7. It varies from 50 µeV around the Dirac point to 80 µeV at high charge carrier density. If we consider the value of Δ extracted from the temperature dependence, it leads respectively to $I_cR_N = 0.75\ \Delta_0/e$ and $1.19\Delta_0/e$. These values are two time lower than the expected ballistic ones $2.08\Delta_0/e$ $2.44\Delta_0/e$. The junction is then unlikely to be in the ballistic regime.

5.6 Conclusion of chapter 5

We successfully observed an induced supercurrent in a graphene sheet connected with superconducting Al electrodes. Unfortunately, a premature switching to the resistive state perturbs the measurements. Especially, the expected multiple Andreev reflection structure is not identified. Despite the shortness of the junction, the ballistic regime is not reached as the I_cR_N product does not correspond to the expected ballistic value, or at least is not higher than what has already been reported. The length of the junction might then not be the most decisive parameter. To identify formally the ballistic regime, measurements performed on suspended graphene or on graphene transferred on top of an atomically flat substrate such as hexagonal boron nitride may give better results. This way, one would get rid of the scattering from charged impurities inherent to SiO_2 substrates [61].

Chapter 6

Proximity-induced superconductivity in dual-gated bilayer graphene sheet

6.1 Introduction

As discussed in section 2.4, a comprehensive experimental work on proximity induced superconductivity in graphene has already been done. So far, only monolayer graphene has been considered though. In a sample consisting of a simple bilayer graphene sheet connected with superconducting electrodes, induced supercurrent and Andreev reflection are not expected to show dramatic differences compared to the monolayer case. A specific feature of bilayer graphene is the possibility to open a band gap by breaking the symmetry between the two layers. This is usually achieved by designing a top gate in a addition to the usual back gate (as described in section 1.2.3). In a device consisting of a dual-gated bilayer graphene sheet connected with superconducting electrodes, it should be theoretically possible to observe a transition from a superconducting state (in which the bilayer graphene carries a dissipationless current) to an insulating state. The other common ways to open a gap in the band structure of a graphene sheet, such as the design of nanoribbon structures, do not allow an easy tuning of the amplitude of this gap. Dual-gated bilayer graphene sheets are then the best devices so far to observe such a transition.

6.2 Theoretical predictions

Proximity-induced superconductivity in bilayer graphene has not raised as much interest as the monolayer case. Some theoretical predictions are available though. Ludwig *et al.* predicted that specular Andreev reflection can occur in bilayer graphene as well [76]. Muñoz *et al.* performed numerical calculations based on a tight-binding model [77]. Their results show that a potential difference between the two layers can suppress the induced supercurrent in the bilayer graphene sheet, as the gap in the bilayer band structure can overtake the superconducting gap from the electrodes. This is valid if the length L of the sample is larger than the Fermi wavelength λ_F. In the regime $L < \lambda_F$ the supercurrent is enhanced, but this regime is unlikely to be observed experimentally. At a constant potential difference between the two layers, increasing the chemical potential can reactivate the induced supercurrent (figure 6.1). Calculations of the supercurrent distribution in the bilayer graphene sheet show that the current is not homogeneously distributed in the two layers. To satisfy the current conservation, an interlayer current is present (figure 6.2). According to the simulations, the relation between the critical current and the chemical potential is quite close to that of the monolayer case.

This last result seems to contradict analytical calculations by Takane *et al.* in the quasiclassical approximation. The authors calculated the critical current for both monolayer and bilayer SGS junctions [78] [79]. These calculations lead to a linear dependence of the critical current on the chemical potential μ in the monolayer case (which is consistent with the results of reference [38]), but a $\sqrt{\mu}$ dependence for the bilayer case. The possibility to open a gap is not considered in those calculations.

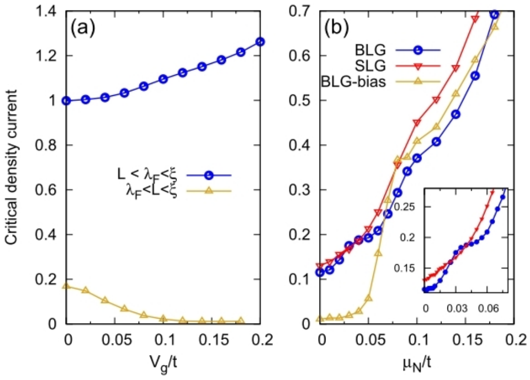

Figure 6.1: Results from tight-binding model calculations, adapted from [77]. (a) Critical density current as a function of the potential difference V_{bg} between the two layers, in the two regimes $\lambda_F < L < \xi$ and $L < \lambda_F < \xi$. (b) Critical density current as a function of the chemical potential, for a monolayer, a bilayer and a bilayer with a broken symmetry between the two graphene layers.

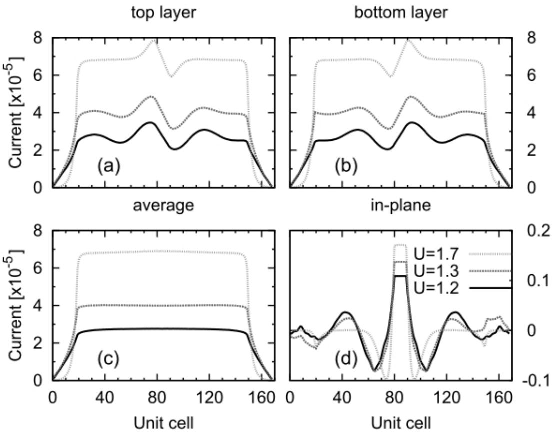

Figure 6.2: Distribution of the supercurrent in the (a) top and (b) bottom layer of a bilayer graphene sheet. (c) shows the average current and (d) the interlayer current. The current distribution in inhomogeneous, and an interlayer current is present. The results are plotted for various pairing potentials. Adapted from [77].

6.3 Sample geometry

We present here the measurements performed on a dual-gated bilayer graphene sheet at low temperature (down to 7 mK). The bilayer is sandwiched between two hexagonal boron nitride (hBN) sheets. The design of such a sample requires to employ the transfer technique presented in section 3.3. A graphite sheet is used a the back gate, to improve the sample's flatness. The bilayer is connected to Ti/Al (5 nm/40 nm) electrodes, deposited in a ultra-high vacuum device.

Figure 6.3a is an optical picture of the sample after the contact deposition. The sample's length and width (for the considered contact pair) are $L = 310$ nm, 6.75 µm. Our device satisfies $W/L \gg 1$ with a ratio of 21.8. The top-gate consists of a global Ti/Al layer deposited on top of another boron nitride sheet. Because the hBN sheet was not homogeneously flat at the extremities of the contacts, it was not safe to design a local top gate only between the contacts. An AFM picture of the finished sample is presented on figure 6.3b.

The thicknesses of the boron nitride sheets are 15 nm for the back gate and 23 nm for the top gate. A diagram of the sample structure is shown on figure 3.13. Our sample is a good example of a Van der Waals heterostructure, which are devices consisting of a stack of different atomically thin materials assembled in a desired order [80].

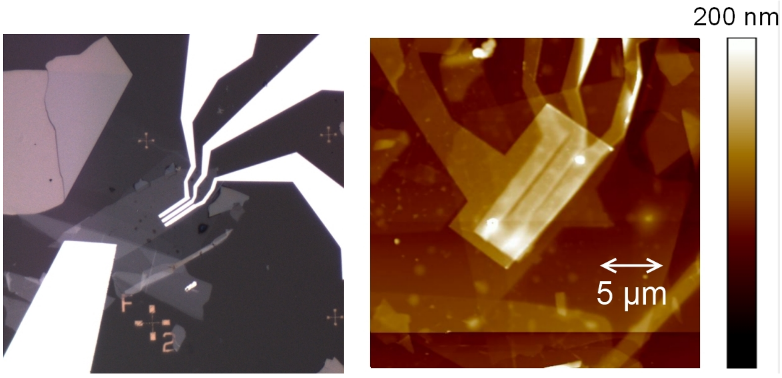

(a) **(b)**

Figure 6.3: (a) Optical picture of the sample after the deposition of the contacts. (b) AFM picture of the finished sample, after the transfer of the second boron nitride sheet on top of the electrode and the deposition of the global top gate.

6.4 Measurements with the back gate only

6.4.1 Device characterization

The sample is measured with the setup described in Chapter 4. Except when indicated, all measurements are done at $T = 7$ mK and with the top gate voltage $V_{tg} = 0$.

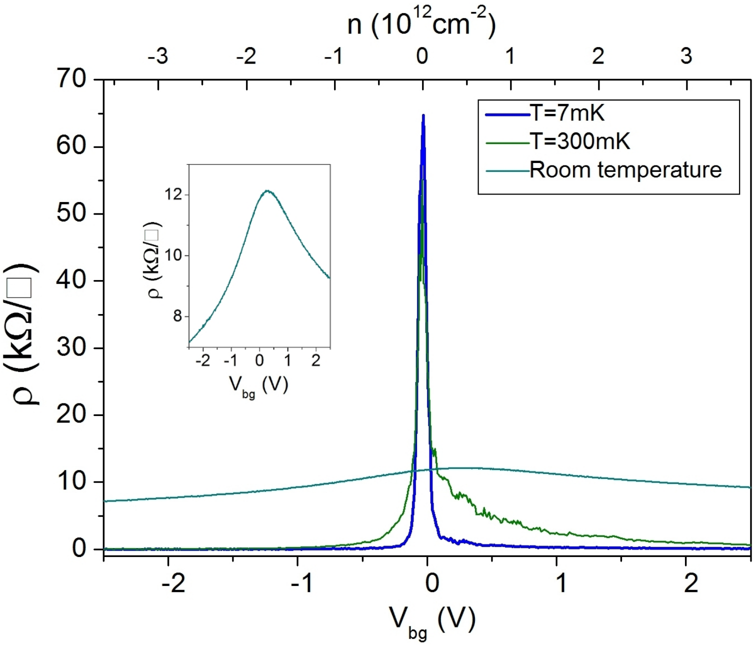

Figure 6.4: Measurement of the resistivity as a function of the back gate voltage at room temperature, 300 mK and 7 mK. Inset : measurement at room temperature.

Figure 6.4 shows the resistivity versus back gate voltage V_{bg}, with unbiased contacts and for several different temperatures. The back gate voltage tunes the charge carrier density via the equation $n = \alpha(V_{bg} - V_D)$, with $\alpha = \frac{1}{e}\frac{\epsilon_0 \epsilon_r}{d} = 1.47 \times 10^{12}.\text{cm}^{-2}.\text{V}^{-1}$ and V_D the gate voltage corresponding to the Dirac point. A much sharper Dirac peak than at room temperature is observed at 7 mK for $V_{bg} = -0.035$ V. This reflects a strong improvement of the sample's mobility. At 7 mK the resistance vanishes away from the Dirac point, which is a sign that the sample can carry a supercurrent. At 300 mK, a higher charge carrier density is required to reach this superconducting state. This behavior is different from most of the results present in the literature. Almost all similar experiments with a monolayer graphene sheet reported that the supecurrent still exists at the Dirac point. Only reference [53] reported a transition from superconducting to resistive state by tuning the gate voltage. In this reference the switching to the resistive state is attributed to the length of the junction (1.2 µm) leading to the emergence of charge puddles breaking the supercurrent coherence. This is unlikely to be the case here as our junction is both short and had been positioned on a substrate reducing the presence of charge puddles [62]. In our case, the absence of an induced supercurrent around the Dirac point as well as the high resistivity observed (up to 65 kΩ/□) can be explained by the presence of a gap in the band structure of the bilayer. This will be investigated in section 6.4.5.

Figures 6.5 shows the same measurement with an additional magnetic field of 20 mT, applied perpendicularly to the graphene sheet. As expected, the superconductivity is suppressed and the resistance reaches its normal state value, even at high charge carrier

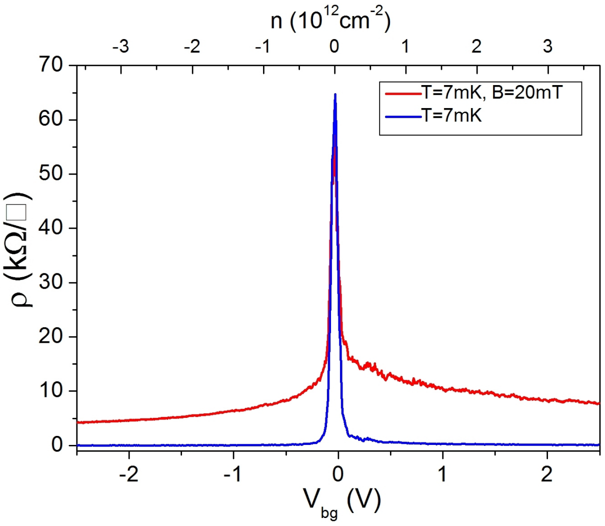

Figure 6.5: Resistivity versus back gate sweep in the presence of a 20 mT magnetic field perpendicular to the graphene sheet. The same measurement at zero magnetic field is added for comparison.

density. Around the charge neutrality point, the resistance is close to that measured without any magnetic field. An asymmetry is noticeable. At high charge carrier density the resistivity reaches 4350 Ω/□ in the hole side and 7600 Ω/□ in the electron side. This asymmetry is usually attributed to the invasive nature of the electrodes (crossing the whole graphene sheet), leading to the presence of a $p-n$ junction under the metal for one of the branches [81]. Our contacts are hence not totally transparent.

From the measurement in the normal state, we can calculate the field effect mobility defined by $\mu_{FE} = (1/C)d\sigma/dV_{bg}$ with $C = \epsilon_0\epsilon_r/d$ the unit-area gate capacitance of the back gate. We find a mobility of 5000 cm^2/Vs around the Dirac point. This can be considered at first sight as relatively small, as mobilities higher than 80.000 cm^2/Vs have been reported in bilayer graphene sheets on hexagonal boron nitride substrate [60]. This apparently low mobility can be attributed to the fact that we perform two-terminal measurements only: the contact resistance is added to the total measured resistance. The short length of the junction reinforces the importance of this contribution. Similar low mobilities have been reported in other superconductor-graphene-superconductor measurements involving short junctions as well (in references [48, 47, 82]).

6.4.2 Measurement of the induced supercurrent

For the next measurements, we set a constant back gate voltage and we put the sample out of equilibrium by setting a current bias through the electrodes. Figure 6.6 presents the resulting $I-V$ curves for a few V_{bg}. Away from the Dirac point the current flows without resistance up to a finite critical current I_c. As expected according to the previous measurements, the induced supercurrent vanishes around the charge neutrality

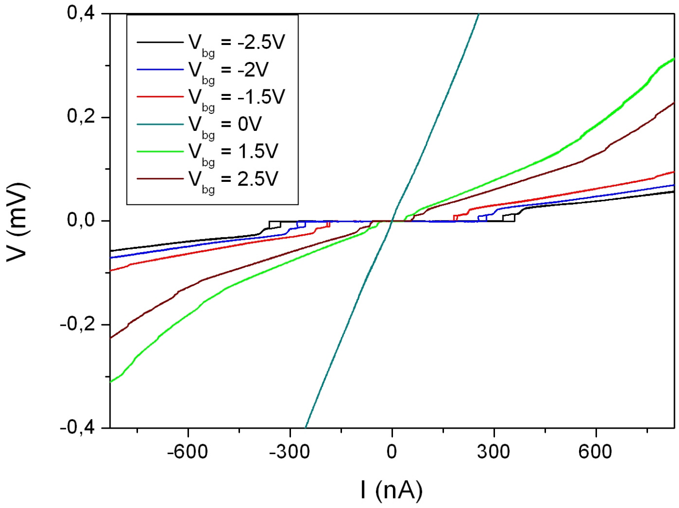

Figure 6.6: *I*-*V* curves for various back gate voltages. The absence of voltage up to $I = I_c$ proves that a supercurrent had been flowing through the graphene sheet. The critical current varies with the charge carrier density. It decreases and vanishes around the charge neutrality point. A hysteresis is visible for high negative back gate voltage.

point.

The critical current can be extracted from the $I-V$ curves. Figure 6.7a shows the measured critical current as a function of the gate voltage. A noticeable asymmetry is present between the hole and electron sides: the critical current is much higher in the branch where the current is carried by holes. This is consistent with the higher normal state resistance previously measured in the electron branch. There is no supercurrent around the Dirac point, and the critical current rises linearly with the gate voltage. In two-dimensional systems, $k_F = \sqrt{4\pi n/g_s g_v}$ and in bilayer graphene $E_F = \hbar^2 k_F^2/2m^*$ so $E_F \propto n$. In our device, the critical current is then proportional to the Fermi energy.

Figure 6.7b shows the critical current as a function of the temperature for two values of the back gate voltage. The critical current decreases due to the reduction of the superconducting gap Δ_0 in the electrodes. The measurement is fitted with a Kulik-Omel'yanchuk model in the dirty limit, in which the mean free path and the superconducting coherence length satisfy $l \ll L \ll \xi$ (described in section 2.2.1.5). The observed temperature dependence corresponds to a gap of $\Delta_0(T = 0) \approx 56$ µeV (or a critical temperature of ~ 370 mK as in the BCS theory $\Delta_{BCS} = 1.76 k_B T_c$ [27]). The measured critical current at $T \sim 0$ does not reach the expected value in this model ($2.07\Delta_0/eR_N \approx 560$ nA for $V_{bg} = -2.5$ V). This can be attributed to imperfect interfaces between the electrodes and the graphene sheet.

A hysteresis is visible for high negative back gate voltages. The difference between the critical current and the retrapping current (which correspond to the transition from resistive state to superconducting state) is relatively small, and vanishes at the density $n \sim -1.4 \times 10^{12}$ cm^2. The hysteresis does not reappear at high positive gate

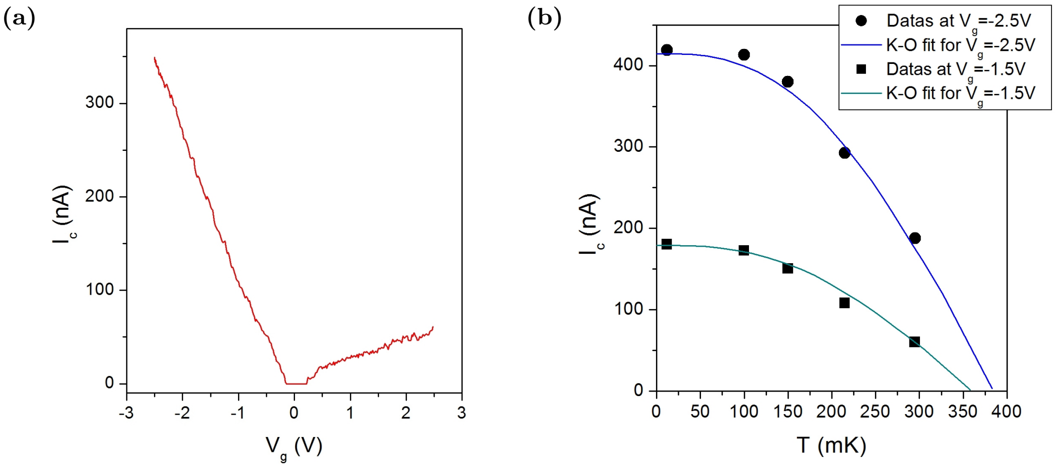

Figure 6.7: (a) Measurement of the critical current I_c of the junction as a function of the back gate voltage. (b) Temperature dependence of the critical current I_c for different back gate voltages.

voltages, confirming the electron-hole asymmetry. Within the RCSJ model (described in section 2.2.1.2), this hysteresis is attributed to the presence of a finite capacitor. Our results can be compared with their equivalent RCSJ model. The parameters are directly extracted from the measurements (normal state resistance and critical current), except the capacitance which is adjusted until the hysteresis matches the observed one. The quality factor Q of the junction is then defined by $Q = w_p RC$, with $w_p = \sqrt{\frac{2eI_c}{\hbar C}}$ its plasma frequency. As the hysteresis (characteristic underdamped junctions) vanishes for charge carrier density above $\sim -1.4 \times 10^{12}$ cm^{-2}, we observe an underdamped-to-overdamped transition. Figure 6.8 shows a simulated RCSJ model with the parameters calculated for $V_{bg} = -2.5$ V, and a comparison with the actual measurement. As the model does not take in account all the features such as multiple Andreev reflection, the two curves differ immediately after the hysteresis and are parallel only at high bias, where the normal state resistance is reached. For $V_{bg} = -2,5$ V, the plasma frequency is $w_p = 1.82 \times 10^{11}$ Hz, the capacitance is $C = 3.29 \times 10^{-14}$ F and the quality factor is $Q = 1.16$. The value of Q corresponds to a underdamped junction as expected.

6.4.3 Multiple Andreev reflection

In addition to the supercurrent, features coming from multiple Andreev reflection (MAR) are expected in our measurements. They are usually slightly visible in the current-voltage curves, and appear more clearly in the form of minima present at $2\Delta_0/en$ voltages in the differential resistance versus bias voltage across the junction measurements.

In our case, a much more complicated structure is present. Figure 6.9 shows an example of differential resistance measurement, performed at high charge carrier density. Sharp differential resistance peaks are present, and their structure and position on the

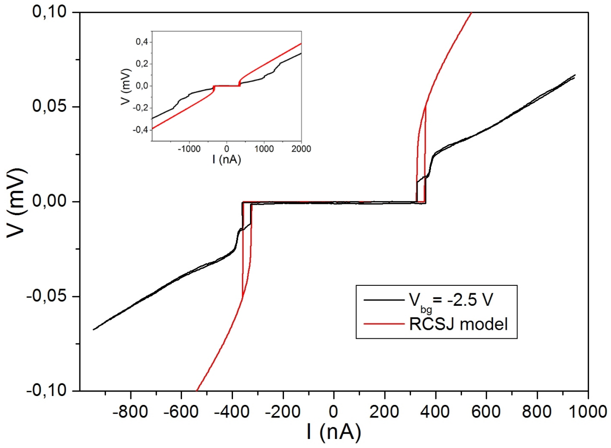

Figure 6.8: Comparison of a simulation from the RCSJ model with an actual measurement for $V_{bg} = -2.5$ V.

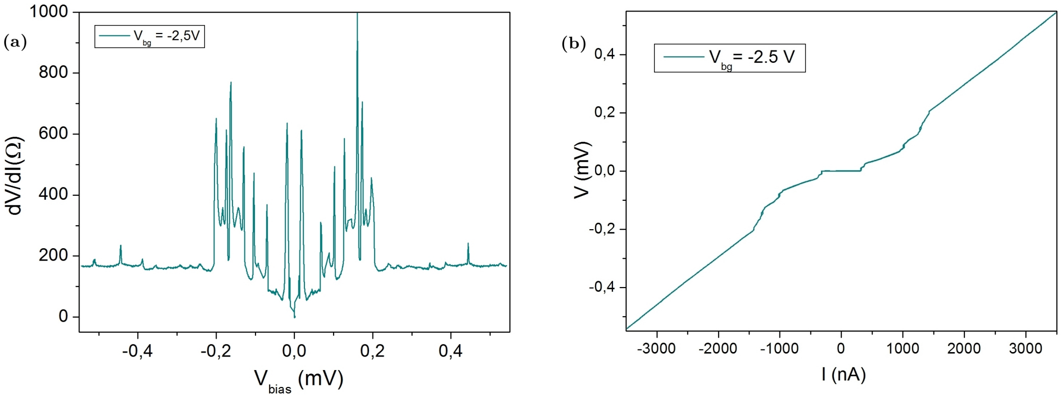

Figure 6.9: Differential resistance dV/dI as a function of the bias voltage V_{bias} (a) and I-V curve (b) for $V_{bg} = -2.5$ V.

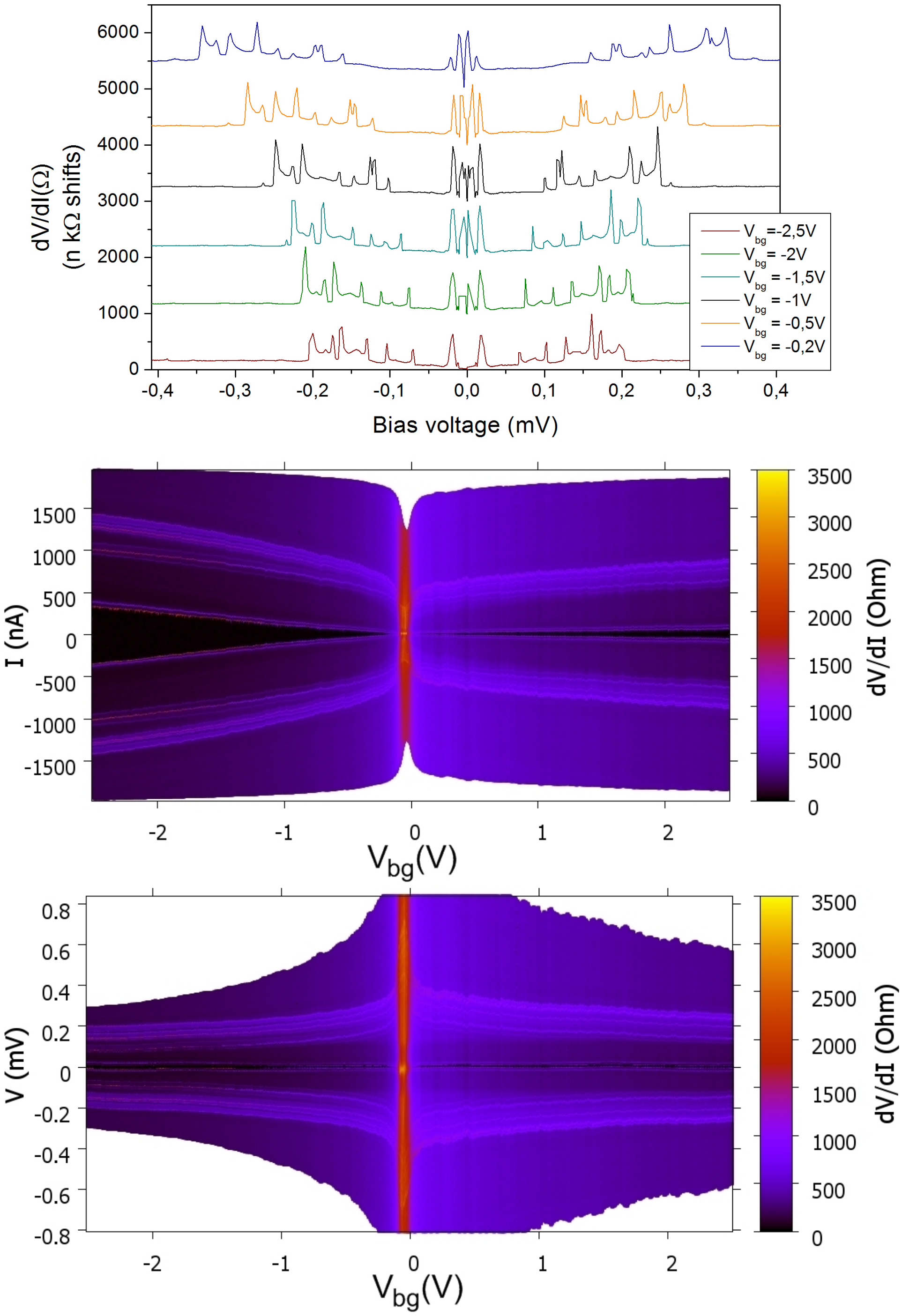

Figure 6.10: Top: differential resistance measurements as a function of the voltage bias, for various back gate voltages. Middle and bottom: color plot of the differential resistance dV/dI as a function of the back gate voltage V_{bg} and the bias current I (middle) and voltage V (bottom).

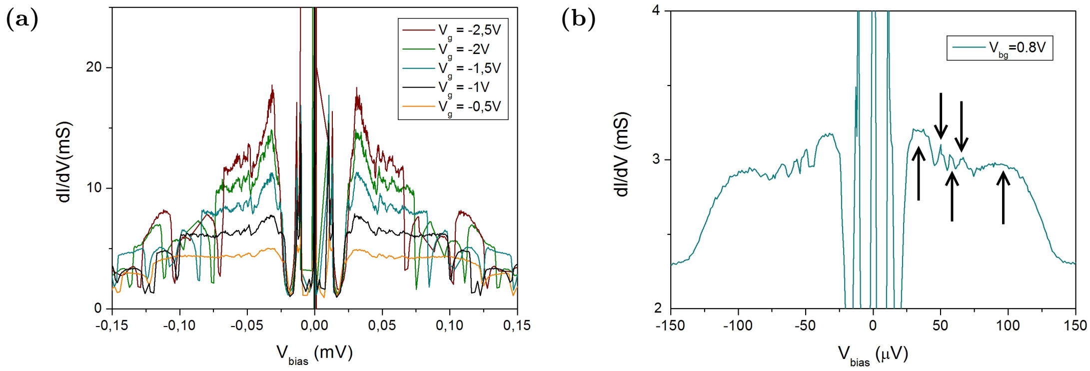

Figure 6.11: (a) Differential conductance as a function of the bias voltage for various gate voltages. A serie of conductance peaks independent of the gate voltage is visible. (b) Single differential conductance measurement on which the conductance peaks are indicated.

bias voltage axis does not correspond to the expected MAR. Figure 6.10 represents a back gate mapping of the differential resistance, as a function of the current and voltage respectively. The positions of these high resistance peaks are not constant. As we get closer to the charge neutrality point, they occur at higher bias voltages. This can be observed on the cascade plot of figure 6.10. As the MAR structure is expected to be gate-independent, these peaks cannot be attributed to MAR.

A closer look at lower voltage bias shows conductance peaks that may correspond to the actual MAR features. They are visible at $V = 34$ µV, $V = 48$ µV, $V = 58$ µV, $V = 67$ µV, $V = 96$ µV 6.11a. Their positions are independent of the gate voltage. They are sharper away from the Dirac point and their intensity is reduced close to it (while the high resistance peaks are still visible). This is consistent with the disappearance of the induced supercurrent around this point. Unfortunately at high charge carrier density the sharp resistance peaks get closer to these smaller resistance dips and prevent their observation. As a consequence we can not get all the conductivity peaks sharp and visible in the same measurement. A superconducting gap value of $\Delta_0 \approx 50$ µeV is consistent with three of the observed conductivity peaks (figure 6.11b) and with the gap previously evaluated with the temperature dependence of the critical current. This value is in agreement with the Δ_0 measured by other groups with similar Ti/Al electrodes (from 55 to 125 µeV in references [44, 43, 47, 45]).

6.4.4 Diffusive or ballistic regime ?

With the superconducting gap Δ_0 determined in the previous section, we can evaluate the superconducting coherence length in the graphene layer, defined by $\xi = \sqrt{\hbar D/\Delta_0}$ with $D = 0.02$ m^2/s the diffusion constant in the sample calculated from the mobility. We find $\xi = 572$ nm, which is of the same order of magnitude as the junction length ($L = 310$ nm) but still almost two times higher. The device is thus in the short-junction regime ($L \ll \xi$) rather than in the long one ($L \gtrsim \xi$), in which the Josephson effect is weaker.

In Josephson junctions the critical current is correlated with the normal state resistance R_N. The I_cR_N product is highly dependent on the diffusive or ballistic nature of the junction. In a ballistic monolayer graphene junction, the I_cR_N product is expected to be equal to $2.44\Delta_0/e$ away from the Dirac point [38]. To our knowledge no similar prediction is available so far for bilayer graphene. We can still consider some theoretical expressions of the critical current in bilayer graphene.

According to Muñoz *et al.*, bilayer and monolayer Josephson junctions with the same Fermi energy should have a similar critical current as long as no gap is present in the band structure of the bilayer graphene [77]. This is visible on figure 6.1. A first approximation of the critical current in a bilayer graphene junction can then be the equation of the critical current in monolayer graphene. From reference [38], for a ballistic junction we have:

$$I_c = 1.22\frac{e\Delta_0}{\hbar}\frac{E_F W}{\pi\hbar v_{F,m}} \tag{6.1}$$

A second theoretical expression was given by Takane *et al.* for the critical current in a ballistic bilayer graphene junction [79]:

$$I_c = e\frac{2W\sqrt{\gamma_1 E_F}}{\pi v_{F,m}\hbar^2}\frac{\Gamma\Delta_0/2}{\Delta_0 + \Gamma/2} \tag{6.2}$$

Here $v_{F,m}$ represents the Fermi velocity in monolayer graphene, γ_1 is the interlayer coupling energy and Γ characterises the coupling strength between the bilayer graphene sheet and the superconductors. In the strong coupling limit, $\Gamma \gg \Delta_0$ and the critical current is maximised. These two equations are not valid close to the Dirac point. Calculated values of the critical current from equations 6.1 and 6.2 are shown on figure 6.12a. For the equation 6.2, the parameter Γ used is 0.889 µeV. We notice that the linear behavior does not correspond to the critical current calculated from equation 6.2. It agrees better with the theoretical critical current in a monolayer graphene junction, despite the factor 20 between the measured and theoretical values for the hole branch. This difference can be attributed to the imperfect interfaces between the bilayer graphene sheet and the electrodes which are not considered in the theoretical prediction (no corresponding parameter can be adjusted in equation 6.1).

The normal-state resistance is extracted from the measurement shown in figure 6.5. Figure 6.12b shows the measured I_cR_N product as a function of the back gate voltage. Two additional curves represent the measured normal-state resistance multiplied by the calculated critical current from equations 6.1 ($I_{c,m}R_N$) and 6.2 ($I_{c,b}R_N$). As we multiply the previously calculated critical currents with the same resistance, again the calculated $I_{c,m}R_N$ from equation 6.1 fits more the behavior of the measured product, with the same factor of 20 between the two in the hole branch. Despite this factor, if we compare the measured product with the superconducting Δ_0 evaluated previously we find $I_cR_N = 1.31\Delta_0/e$ which is of the same order of magnitude as the theoretical ballistic value $2.44\Delta_0/e$ for monolayer graphene junctions.

The critical current and I_cR_N behaviors in our device correspond at high charge carrier density to the expected ones in a monolayer graphene Josephson junction close to the ballistic regime. This corroborates the results of Muñoz *et al.* which predicted similar properties for both monolayer and bilayer graphene as long as no asymmetry is present in the bilayer case [77]. The linear E_F dependence of the critical current is not consistent with the theoretical predictions of Takane *et al.* which give a $\propto \sqrt{E_F}$ dependency.

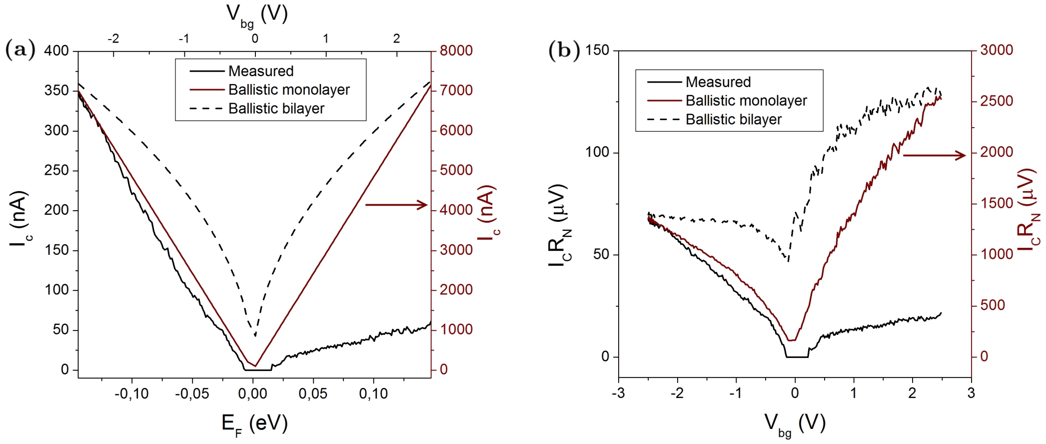

Figure 6.12: (a) Measurement of the critical current I_c of the junction as a function of the back gate voltage and the Fermi energy, and theoretical predictions in the monolayer and bilayer case in the ballistic regime. (b) Measured I_cR_N and calculated $(I_{c,m}R_N)$, $(I_{c,b}R_N)$ product of the sample as a function of the back gate voltage. For both (a) and (b) the theoretical predictions are not valid close to the Dirac point and the theoretical curve for the monolayer case uses a different scale.

6.4.5 Evidences of the superconducting to insulating transition

Figure 6.13a shows $I-V$ curves at low bias, for various back gate voltages. In addition to the vanishing of the supercurrent, we notice a non-linearity when the Fermi energy is set near the Dirac point. By getting closer to this point we observe a transition from the superconducting state (step at $V = 0$) to a gapped state (emergence of a step at $I = 0$). Figure 6.13b shows the differential conductance as a function of the voltage bias at the Dirac point. The presence of a non-linearity is more visible in the dI/dV versus V curve than in the $I-V$ curves. From figure 6.13b we can determine the voltage bias scale on which the non-linearity occurs. At the charge neutrality point, we find this scale to around 20 µV by considering the full width at half maximum. This value is two orders of magnitude lower than what has been measured by other groups at large displacement field (2.2 mV in reference [20]). As we obtain this result without tuning the top-gate, our device presents a spontaneous but relatively low broken symmetry, leading to this transport gap. This asymmetry suppresses the induced supercurrent which can be reactivated at higher Fermi energy, as predicted by reference [77] (figure 6.1).

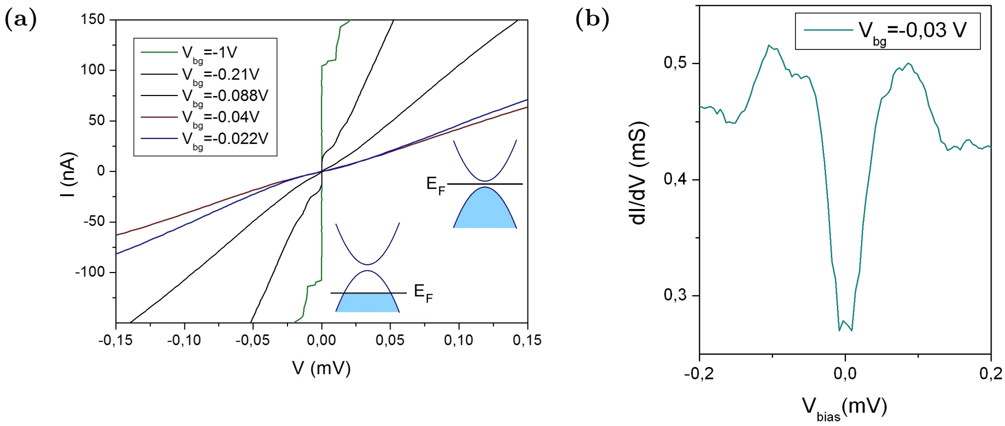

Figure 6.13: (a) I-V curve of the junction for various gate voltages, zoomed at low biases. Schematic diagrams of the corresponding band structures are added. Due to an asymmetry between the two layers, a transport gap is present and the supercurrent vanishes at the Dirac point. At high charge carrier density the supercurrent is activated. (b) Differential conductance at low bias and at the Dirac point. The non-linearity is clearly visible.

According to density-functional-theory calculations performed by Padilha *et al.* [83], a spontaneous gap can emerge in the band structure of a bilayer graphene sheet deposited on an hBN substrate. As in the similar theoretical prediction [63] for monolayer graphene sheet, these calculations assume alignment conditions between the bilayer graphene and hBN sheets that are unlikely to be met in our device, and neglect the lattice mismatch. So far no such spontaneous gap has been reported in bilayer graphene sheet deposited on hBN substrate.

Another way to have an asymmetry in a bilayer graphene sheet would be to apply different strains on the two layers [16]. The bottom layer of our bilayer is subject to the crystal orientation of the hexagonal boron nitride sheet underneath and the top one is either subject to a different crystal orientation or to nothing at all (as the top gate might be suspended between the contacts). This may lead to an asymmetry. The lattice mismatch between bilayer graphene and hBN is 1.7%. In the limiting case where the carbon atoms of the bottom layer align with the hBN lattice but the atoms of the top layer retain their position, a gap of 18.4 meV in the band structure of the bilayer graphene has been predicted [16]. A more reasonable mismatch may then explain the gap observed in our sample.

The presence of a spontaneous broken symmetry (and therefore the opening of a gap in the band structure) has been theoretically predicted in ultra-clean bilayer graphene sheets [84, 85]. Such spontaneous gaps have been reported so far only in transport measurements involving suspended bilayer graphene sheets [86, 87, 88, 23]. The observed gap of 20 µeV in our sample is two orders of magnitude lower than the values obtained in these suspended devices (up to 3 meV). It is therefore unlikely that the gap has the same origin.

6.4.6 Fraunhofer pattern

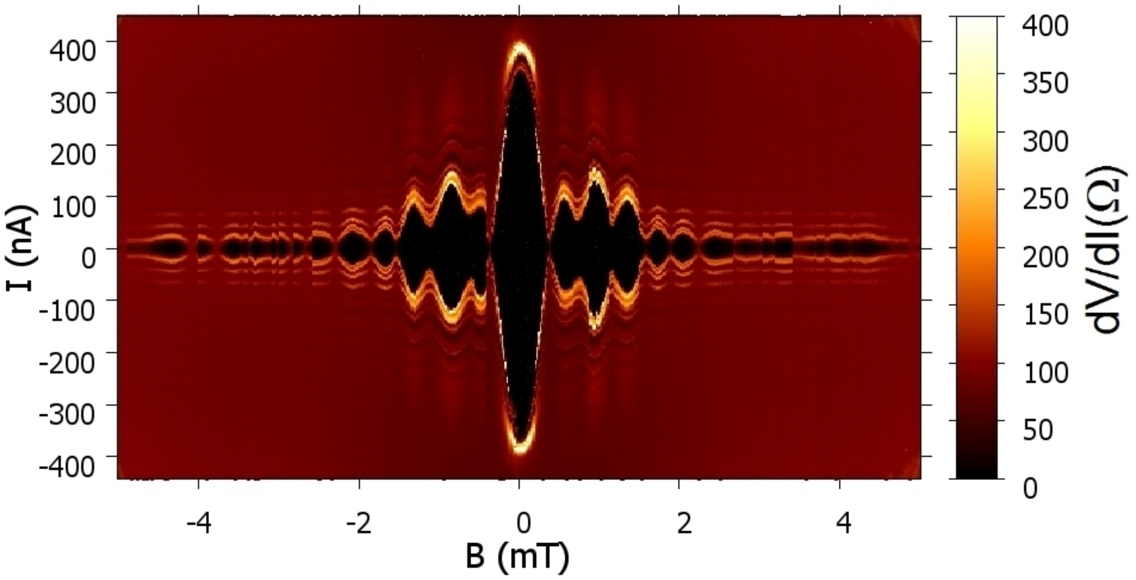

Figure 6.14: Color plot of the differential resistance dV/dI as a function of the magnetic field B and the current I, at high charge carrier density.

The Fraunhofer pattern has been recorded at $V_{bg} = -2,5$ V (and with V_{tg} still at 0 V) in order to have a large supercurrent. The magnetic field is swept from $B = -5$ mT to $B = 5$ mT. For each value of B, a current sweep is performed and the differential resistance is recorded.

Figure 6.14 shows the first Fraunhofer pattern recorded. The measured periodicity is 0.42 mT if we take into account all the peaks. We notice that the amplitude of the second oscillation is smaller than that of the third one. This is different from the results reported with superconductor-graphene-superconductor junctions, in which the the oscillation amplitudes decrease monotonically (as detailed in section 2.2.1.4). As we do not get the Fraunhofer pattern expected for a rectangular Josephson junction, we can conclude that the supercurrent is not homogeneously distributed along our junction. This might be caused by an inhomogeneous supercurrent distribution between the two layers of the bilayer graphene sheet. Such inhomogeneities have been predicted in reference [77]. This hypothesis can be reinforced by the fact that in our device the charge carriers are injected to the top layer only (while in reference [77] the bilayer is considered as sandwiched between the electrodes).

We tried to fit the obtained pattern with a model consisting of two Josephson junctions with different areas and critical currents in parallel but no satisfying solution has been found. As the obtained pattern does not correspond to the expected one, comparing the measured periodicity with the theoretical value for a rectangular junction $\Phi_0/WL = 0.99$ mT determined from the device geometry may not make much sense at first. It is still worth mentioning that if we do not take in account the second oscillation (which can be justified by the fact that this oscillation is smaller than the next one), we find a periodicity of 0.84 mT. This value would match the theoretical one. The presence of the second oscillation would have then to be discussed.

In order to study the behavior of the features observed in the differential resistance curves, the measurement is extended to higher bias. Figure 6.15 shows that the amplitude of the high resistance peaks decreases regularly when we increase the magnetic field. They occur at smaller current biases too. At $B = 10$ mT most of them are vanished. As a magnetic field from the same order of magnitude is required for the supercurrent to vanish as well, the high resistance peaks are likely linked with the induced superconductivity. Their structure is not preserved: as we increase B the peaks frequently cross and mix with each others, which complicates the interpretation.

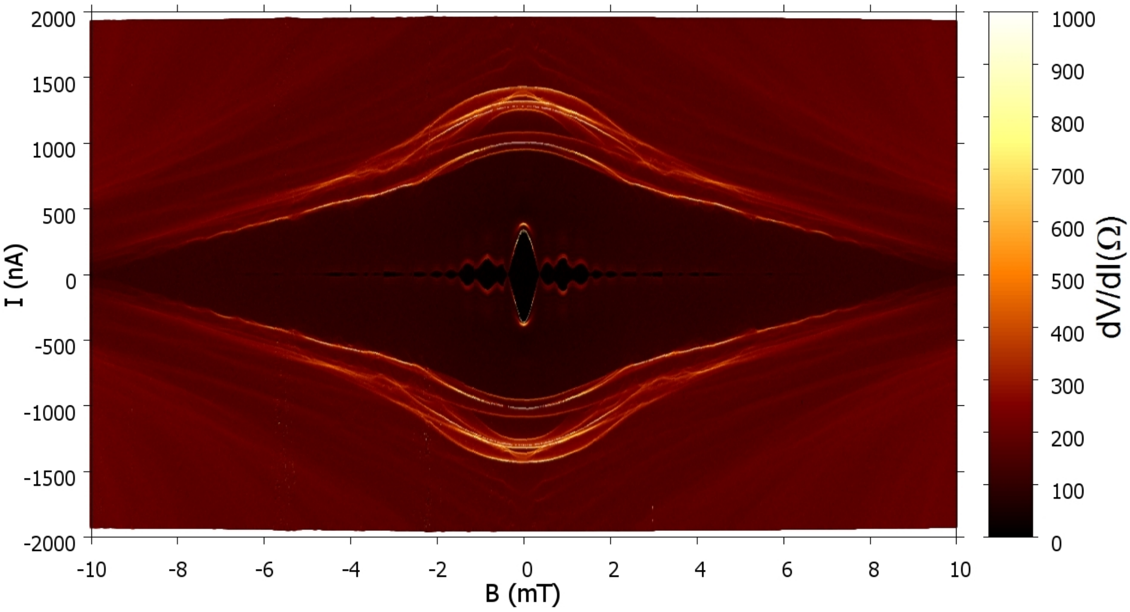

Figure 6.15: Extension of the measurement of the Fraunhofer pattern to higher biases, in order to observe the behavior of the high resistance peaks noticed previously. The differential resistance dV/dI is plotted both as a function of the bias current I and the magnetic field B.

6.4.7 Hypothesises for the high resistance peaks

As seen previously, the high resistance peaks observed in the differential resistance measurements do not correspond to multiple Andreev reflection. Their behavior in the presence of a magnetic field suggests that they are still related to superconductivity.

High resistance peaks in a superconductor-graphene-superconductor junction have been reported in reference [82]. They are attributed to self-induced Shapiro steps, due to the enclosing of the sample in a metal box. Shapiro steps lead to voltage steps ΔV

of amplitude $\hbar\omega/2e$ in the $I - V$ curves of a junction (figure 6.16). It is unlikely that the high resistance peaks that we observe are due to this effect. First of all, while the voltage step ΔV between the peaks is supposed to be constant and a function of the frequency only, it is not constant when the back gate voltage is tuned. The voltage step ΔV are actually not constant even in a single measurement. In addition, the sample was not enclosed in an environment likely to support standing waves.

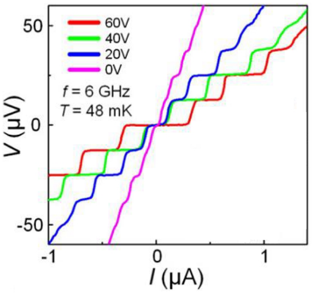

Figure 6.16: Typical Shapiro steps measured in a superconductor-graphene-superconductor junction. I-Vs are plotted for various values of the gate voltage. Unlike what is observed in our sample, here the voltage steps ΔV are independent of the gate voltage. Adapted from [49].

Choi *et al.* observed an unusual conductance jump at high bias, attributed to an increase of the electronic temperature [47]. As this jump occurs only one time and not periodically, this is unlikely to correspond to the resistance peaks that we observe.

Another hypothesis to be considered is the McMillan-Rowell oscillation (described in section 2.2.2.2). The high resistance peaks would theoretically occur at the voltage biases given by:

$$eV_m = eV_0 + \frac{mhv_F^N}{4L_N} \tag{6.3}$$

with m an integer, v_F^N the Fermi velocity in the bilayer graphene, and L_N its length. According to this equation, the voltage bias steps ΔV between the peaks should increase when the Fermi level is tuned away from the Dirac point. We observe the opposite in our junction: the steps ΔV are smaller away from the Dirac point. In addition, the ΔV between the peaks is not constant.

The last considered hypothesis involve Tomasch resonances. The high resistance peaks would theoretically occur at the voltage biases given by:

$$eV_m = \pm\sqrt{\Delta_0^2 + \left(\frac{mhv_F^S}{2L_S}\right)^2} \tag{6.4}$$

with m an integer, v_F^N the Fermi velocity in the superconducting area, and L_S its length. This equation does not explain the increase of the voltage bias steps ΔV between the peaks when the Fermi level is tuned close to the Dirac point. In addition, in a single differential resistance measurement the voltage steps ΔV should be slightly decreasing while higher biases are reached. This is not what we observe in our sample.

6.5 Measurement with the top gate only

Figure 6.17 shows a resistance versus top-gate measurement at $V_{bg} = 0$ V, with and without a B=20 mT magnetic field. The capacitive coupling between the bilayer and the top gate is clearly weaker than with the back gate, even though the hexagonal boron nitride sheets used as dielectrics have relatively close thicknesses. This can be easily explained by the fact that the sheet might be partly suspended between the contacts. The maximum at the Dirac point is not as sharp as with the back-gate, and several local minima of resistivity are observed. Because the top gate is likely to be suspended between the contacts, it probably does not affect the whole bilayer graphene sheet homogeneously.

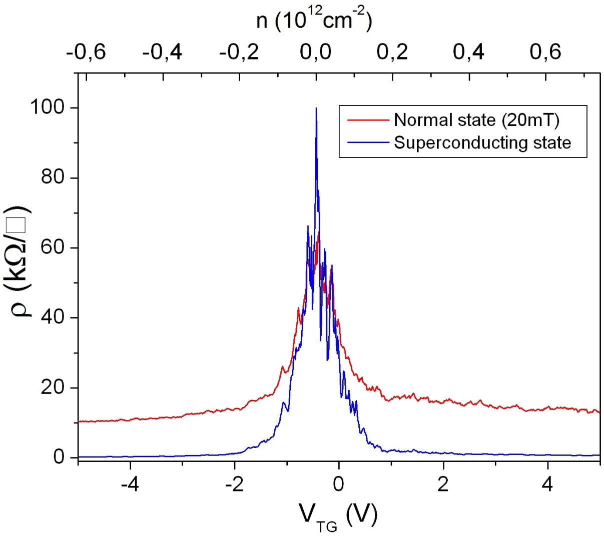

Figure 6.17: Resistivity versus top gate voltage measurement, with the back gate set at 0 V.

6.6 Tuning of the displacement field

We noticed in section 6.4.5 that a transport gap is spontaneously present in our device. For the next measurements, the two gates are used simultaneously, in order to tune the displacement field through the bilayer graphene sheet.

6.6.1 Normal state

Figure 6.18a shows the resistivity of the sample in the normal state (in the presence of a 20 mT magnetic field) as a function of the two gate voltages. The difference of efficiency between the two gates is clearly visible. Figure 6.19a shows back gate voltage sweeps for different top gate voltages. By extracting the gate voltages corresponding to the resistance maxima, we can determine the equation followed by the charge neutrality

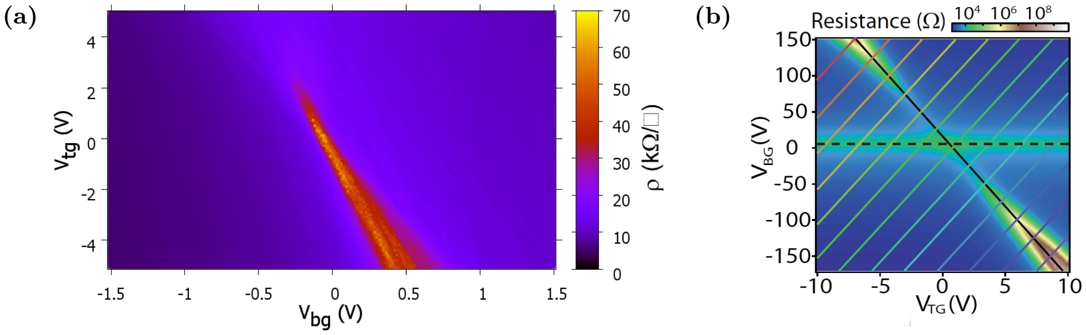

Figure 6.18: (a) Color plot of the resistivity as a function of the top and back gate voltage, in the presence of a magnetic field of 20 mT. (b) For comparison purpose, resistance measurement of a dual-gated bilayer graphene sheet as a function of the top and back gate voltages, extracted from reference [20]. The solid black line represents the charge neutrality line, and the colored lines represent constant displacement fields.

line (on which $n = 0$). We find $V_{tg}(V) = -10.77V_{bg} - 0,38$ V (figure 6.19b). The additional $-0,38$ V can be attributed to the residual doping of the sample. As the top gate is likely suspended, from the previous equation we assume that $C_{bg} = 10,77C_{tg}$ in order to model the top gate as two capacitances in serial (one of boron nitride, one of vacuum). We have then

$$\frac{1}{C_{bg}} = \frac{d_v}{\epsilon_0} + \frac{d_{hBN}}{\epsilon_0 \epsilon_{r,hBN}} \tag{6.5}$$

with d_v the distance between the bilayer graphene and the boron nitride sheet of the top gate, and d_{hBN} its thickness. We calculate $d_v \approx 35$ nm. This is consistent with the thickness of the contacts (around 40 nm). 35 nm is an average value coming from the fact that we model the top gate with plate capacitors: on our device it is likely that the top gate is closer to the graphene sheet in the middle of the junction. For simplification, we can model the top gate as equivalent to a single hBN sheet of thickness 10.77×15 nm ≈ 162 nm too.

To analyse the effects of the two gates, we use the convention from reference [21] and define the displacement field by $D = (D_{bg} + D_{tg})/2$, with $D_{bg} = \varepsilon_{r,hBN}(V_{bg} - V_{bg}^0)/d_{bg}$ and $D_{tg} = -\varepsilon_{r,hBN}(V_{tg} - V_{tg}^0)/d_{tg}$. Here d_{bg} and d_{tg} are the thicknesses of the boron nitride sheets and ε_{hBN} their relative permittivity. Voltage offsets are present to compensate the environment-induced doping. Usually the origin is set to the point of the charge neutrality line where no effective displacement field is present. This point can be determined from the symmetry of the measurement, like on figure 6.18b. As this symmetry is not observed in our measurement, we choose arbitrarily the point ($V_{bg} = 0\ V; V_{tg} = -0.38$ V) as the origin (which is consistent with the equation of the charge neutrality line $V_{tg}(V) = -10.77V_{bg} - 0.38$ V). Our calculated displacement field corresponds then only to the one induced by the gates given by

$$D = (D_{BG} + D_{TG})/2 = \frac{1}{2}\left(\frac{\varepsilon_{r,hBN}V_{bg}}{15\ nm} - \frac{\varepsilon_{r,hBN}(V_{tg} + 0.38V)}{162\ nm}\right) \tag{6.6}$$

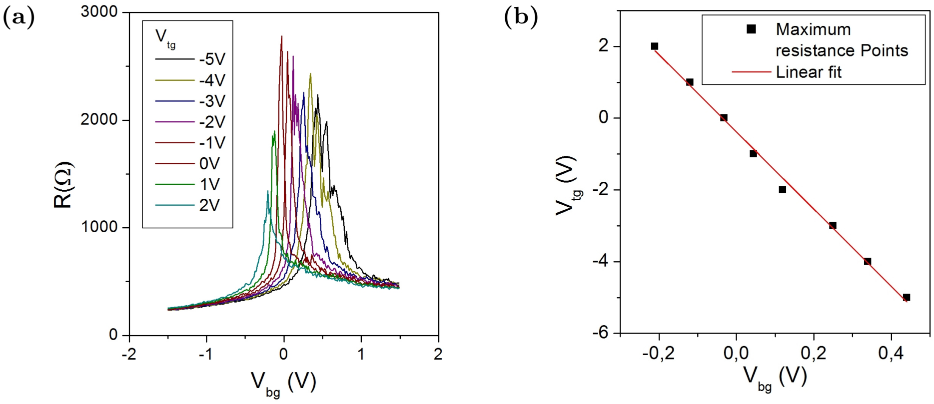

Figure 6.19: (a) Resistance versus back gate voltage plot, for various values of the top gate voltage. The Dirac points are extracted to determine the charge neutrality line. (b) Back and top gate voltages corresponding to the maximum resistances extracted from figure 6.19a. An equation for the charge neutrality line is deduced by a linear regression: $V_{tg}(V) = -10,77V_{bg} - 0,38$ V.

With the two gates, we can tune the Fermi energy and the displacement field. Along the charge neutrality line, the Fermi energy is maintained at zero and the gap in the band structure of the bilayer is tuned by the induced displacement field. Alternatively, it is also possible to maintain a constant displacement field D and to tune the position of the Fermi energy in the conduction or valence band. Figure 6.20 illustrates these two possibilities.

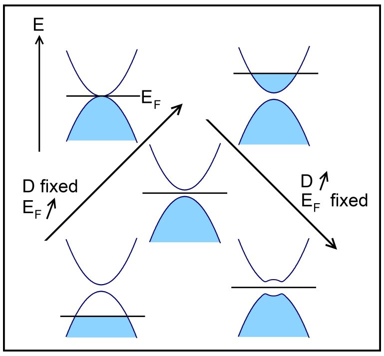

Figure 6.20: Scheme of the band structure of the bilayer graphene sheet and its occupation as a function of the displacement field D and the Fermi energy E_F. With the two gates, it is possible to tune the two values.

We expect by tuning the two gate voltages to have a relatively low resistance at the origin (V_{bg} and $V_{tg} \sim 0$ V) which strongly increases when the two gates are tuned away from 0 V by following the charge neutrality line, due to the opening of a gap. This can be observed on figure 6.18b, which shows the result obtained by Taychatanapat *et al.* with a dual-gated bilayer graphene sheet. In our measurement, the resistivity is already high around the origin and decreases in one of the directions of the charge neutrality line. This difference can be explained by the presence of the spontaneously broken symmetry in our bilayer graphene sheet already noticed in section 6.4.5. Figure 6.21a shows the resistance of the sample along the charge neutrality line and at various

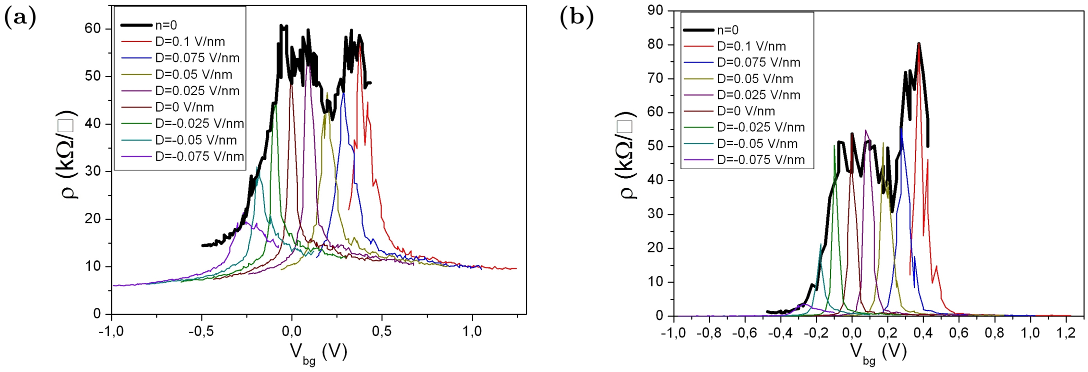

Figure 6.21: Resistivity versus back gate voltage measurement along the charge neutrality line (where n=0) and for various constant displacement fields, with (a) and without (b) a magnetic field of 20 mT. To maintain a constant displacement field, V_{bg} and V_{tg} satisfy the equation 6.6.

constant displacement fields, still in the normal state. Due to the presence of an intrinsic asymmetry in the bilayer, along the charge neutrality line the resistance increases only from negative to positive displacement fields. At constant displacement field, we observe the usual dependence of the resistance as a function of the charge carrier density. Up to $D = 0$, the higher the displacement field, the higher the resistance is at the charge neutrality point. This is consistent with the behavior expected from figure 6.20. The resistance does not reach higher values afterwards, while it is expected to keep rising.

The resistivity increases up to around 55 kΩ/□. This is more than five times higher than the theoretical maximum of resistivity in bilayer graphene $\rho_{min} = \pi^2\hbar/4e^2 \approx$ 10 kΩ/□ [89]. Still, this resistivity is several orders of magnitude lower than the one observed by other groups at large displacement field (up to $\sim$ 10 MΩ/□ in references [19, 22, 88]). This can be explained by the low displacement field reached in our experiment. Due to the weak capacitive coupling between the top gate and the bilayer graphene sheet, D is tuned in an interval of only 0.25 V/nm while in references [20] it reaches values from -2.3 to +1.8 V/nm at least, and the dramatic rise in resistivity starts at $D \sim |0.8|$ V/nm. As a consequence, in our device the energy gap in the band structure of the bilayer graphene stays relatively small and no insulating state is observed.

6.6.2 Superconducting state

Figure 6.22 shows the resistance of the sample as a function of the two gates, but without any magnetic field. Away from the charge neutrality line, the resistance is reduced to zero and a supercurrent can flow. This is consistent with the calculations of reference [77] predicting that in the presence of an asymmetry between the two layers the induced supercurrent vanishes only around the Dirac point and can be reactivated at higher Fermi energy (figure 6.1). The Fermi energy required depends on the displacement field. The shape of the resistive domain on figure 6.22 illustrates it. Along the

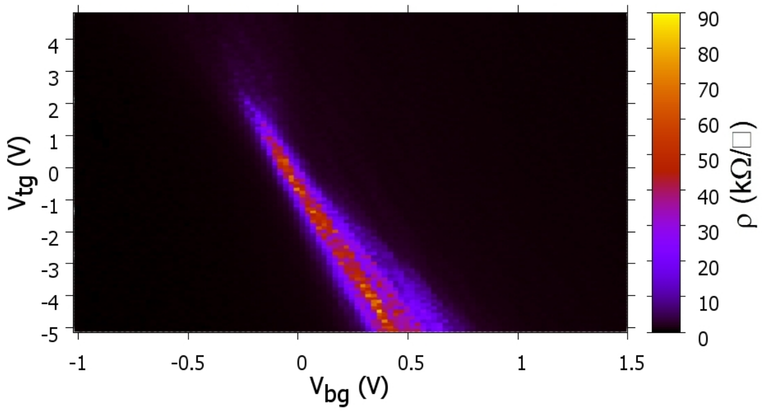

Figure 6.22: Color plot of the resistance as a function of the top and back gate voltages in the superconducting state.

charge neutrality line and from negative to positive values of the displacement field the resistance increases. In the other direction, the resistance goes down to around 50 Ω. This is more clearly shown on figure 6.21b, which represents the resistance of the sample along the charge neutrality line and at various constant displacement fields. This can be interpreted as a compensation of the spontaneous asymmetry by the displacement field induced by the gates. The energy gap in the band structure of the bilayer is suppressed or reduced sufficiently for a supercurrent to flow even at the charge neutrality point. At high displacement field the resistance reaches higher values than in the presence of a magnetic field, up to 3.5 kΩ. This leads to a square resistance of 77 kΩ/□, almost one order of magnitude higher than the theoretical maximum in bilayer graphene $\pi^2\hbar/4e^2$ [89].

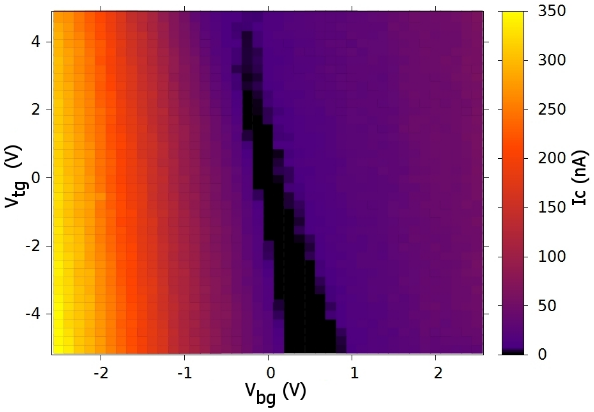

Figure 6.23: Measurement of the critical current as a function of the top and back gate voltages.

The critical current is mapped relatively to the two gate voltages on figure 6.23. The amplitude of the critical current can be slightly increased by tuning the top gate

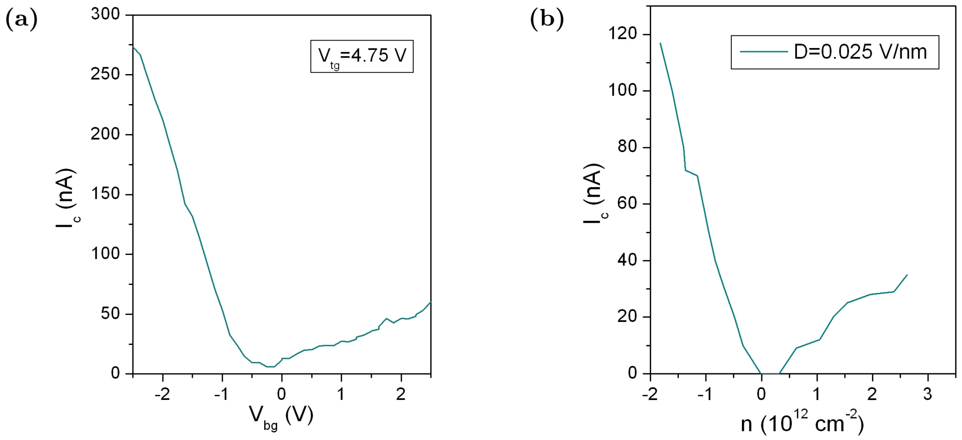

Figure 6.24: (a) Critical current as a function of the back gate voltage for $V_{tg} = 4.75\ V$. (b) Critical current as a function of the charge carrier density for D=0.025 V/nm.

voltage. For sufficiently high top gate voltages, a supercurrent is present for any value of the back gate voltage. Figure 6.24a shows the critical current as a function of the back gate voltage for V_{tg} = 4.75 V. An induced supercurrent is present even at the charge neutrality point. Figure 6.24b shows the critical current as a function of the charge carrier density for a fixed value of the displacement field D. At high density the amplitude of the critical current evolves still linearly with the charge carrier density and therefore with the Fermi energy, as noticed in section 6.4.4. The I_cR_N product is shown on figure 6.25 as a function of the two gate voltages. The normal-resistance state is extracted from the measurement corresponding to figure 6.18a. Like the critical current, the product I_cR_N increases when the sample is tuned away from the charge neutrality line and reaches a finite value at the displacement field $D \sim -0.091$ V/nm along the charge neutrality line. Tuning the top gate voltage can slightly increase or decrease its value. The order of magnitude discussed in section 6.4.4 is therefore maintained.

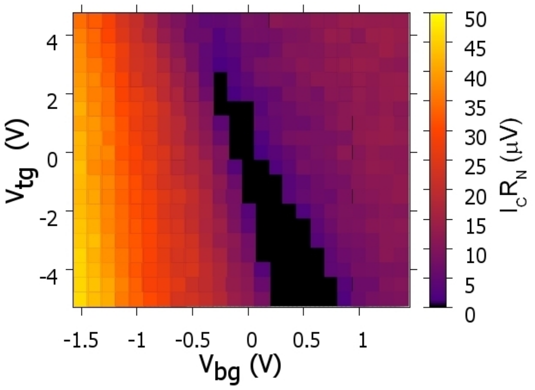

Figure 6.25: I_cR_N product as a function of the two gate voltages.

6.7 Conclusion of chapter 6

A dual-gated bilayer graphene sheet connected with superconducting electrodes has been successfully designed. We measured induced supercurrent, with an amplitude going up to 350 nA. Especially, we noticed that the critical current evolves linearly with the Fermi energy. Our device seems to be close to the ballistic regime. A transition from superconductive to highly resistive state by the opening of a gap has been observed by tuning the voltages of the two gates. In order to observe a complete superconducting-to-insulating state transition, the quality of the sample needs still to be improved: especially, attention must be given to the capacitive coupling between the top gate and the bilayer. Having a thinner or less suspended hBN sheet as the top-gate dielectric should help to reach higher displacement fields. Using atomic layer deposition (described in section 3.4.2) to grow an Al_2O_3 dielectric instead of transferring a second hBN sheet may solve this problem, despite the usual degradation of the sample's mobility resulting from this process. This solution has been considered with several samples, unfortunately none made it to the low temperature measurements. Several new features can be observed in our results, such as the high resistance peaks in the differential resistance measurements and the anomalous Fraunhofer pattern.

Conclusion

In this work, we investigated the properties of induced superconductivity in graphene and bilayer graphene. The measurements were performed down to a temperature of around 7 mK. Home-made filters have been designed and characterised in order to prevent the noise from the room-temperature measurement devices and cables to reach the samples. Especially, a recently developed technique to design metal powder filters on a printed circuit board has been successfully reproduced. This allows the production of filters for a large number of lines in a single step.

In a first experiment, we used a shadow evaporation technique to produce ultra-short superconductor-graphene-superconductor junctions with a single graphene layer. An induced supercurrent has been observed in a 120 nm length SGS junction. The attempt to reach a ballistic regime did not prove successful as we measured a $I_cR_N = 1.19\Delta_0/e$ product below the theoretical ballistic value. The I_cR_N value was not significantly higher than obtained by other groups with comparable junctions.

The most important part of this work focused on the proximity induced superconductivity in bilayer graphene. The sample studied consisted of a van der Waals heterostructure with the graphene bilayer sandwiched between two hexagonal boron nitride sheets used as substrate and gate dielectric. We have been able to observe an induced supercurrent vanishing close to the charge neutrality point, at which the onset of a superconductor-insulator transition was observed. Tuning the displacement field induced in the bilayer with the gates showed that a spontaneous gap was present in its band structure. The origin of this gap is unclear. By tuning both gates, it was possible to compensate this spontaneous gap. A supercurrent was then observable even at the charge neutrality point. This demonstrates that when the Fermi energy is tuned close to this point, the possibility to observe an induced supercurrent depends on the presence of a gap in the band structure of the bilayer. At high charge carrier density, the critical current I_c exhibited a linear dependence on Fermi energy E_F of the bilayer graphene sheet. A similar dependence is expected in ballistic monolayer graphene junctions. By tuning the displacement field, a resistivity of 80 $\mathrm{k}\Omega/\square$ has been measured.

Several unexpected features have been observed during the measurements. Among them, high resistance peaks were present in the differential resistance measured out of equilibrium. These peaks cannot be attributed to the presence of multiple Andreev reflection but are nonetheless linked to superconductivity as they vanish in the presence of a small magnetic field. The measured Fraunhofer pattern is different from that expected for a rectangular Josephson junction. Further work, both theoretical and experimental, is necessary to explain these results. To this purpose, discussions have been engaged with theorists. With these new features and the possibility to fully control the induced supercurrent, we hope to have demonstrated that the proximity induced superconductivity in bilayer graphene deserves as much attention as the monolayer case.

Appendix A

Shadow evaporation for ultra-short junctions

Here we detail the design of ultra-short junctions

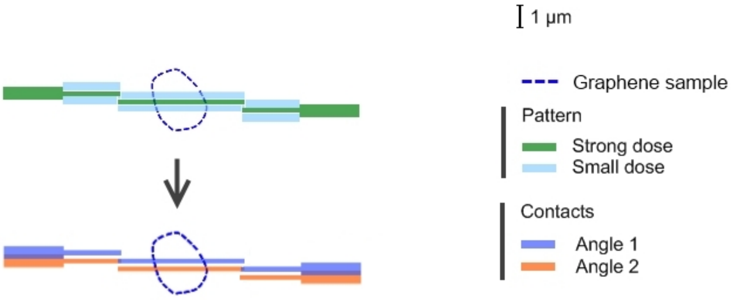

Figure A.1: Schema of the pattern used, and the expected result after the metal deposition.

To design ultra-short junctions, we use a stack of two different resists: a rather thick one (800 nm) made of methyl methacrylate (MMA), and a thiner one (200 nm) made of PMMA on top of the previous one. The rotation speeds employed during the spin-coating are respectively 1500 rpm and 6000 rpm. Figure A.1 shows the pattern used and the expected result.

As the structure is small, attention must be given to the lithography parameters. We use the doses 390 μAs/cm^2 for the elements labelled "strong dose" and 125 μAs/cm^2 for the elements labelled "small dose". A Monte-Carlo simulation is used to correct the dose by taking in account the proximity effect. This effect arises from the fact that during the lithography some electrons reflected from the substrate irradiate neighbouring areas from the one targeted. It results in a reduced effective dose for small elements (typically below a few hundreds of nanometers). Figure A.2 shows the dose factors corresponding to each element of the pattern. The dose selected in the lithography software is multiplied by this factor. As an example, the effective dose for the central rectangle is 1.970 × 390 µAs/cm^2.

Once the lithography is done, the sample must be developed 10 seconds in a isopropanol/methyl isobutyl ketone (MIBK) solution (one dose of MIBK for three doses of isopropanol). The development has to be controlled with an optical microscope. The undercuts should be visible by tuning the focal length of the microscope.

During the metal deposition, the sample holder is rotated around the x axis. The two angles used for this design are -11.3° and 11.3°, with 0° corresponding to the normal incidence relatively to the metal source. We proceed first with the deposition of the titanium layers for the two angles, then with the deposition of the two aluminium layers.

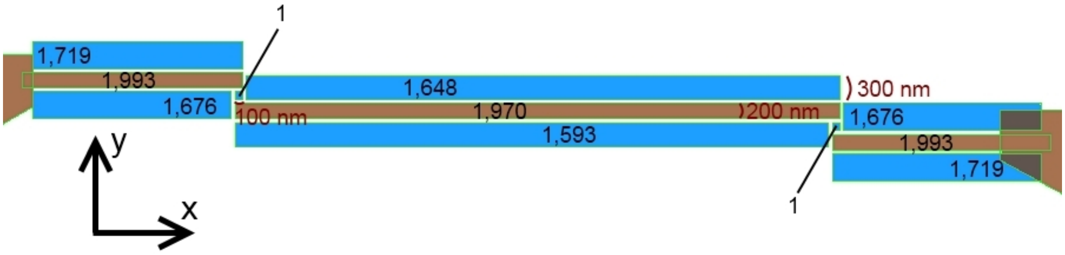

Figure A.2: Pattern used to design ultra-short junctions. The black numbers are the dose factors of the corresponding pattern elements. The width of the main elements are indicated in red. The distance between two consecutive ones is always 50 nm.

Appendix B

C++ code for RCSJ model

This program generates a file containing the I-V datas of a Josephson junction described with the RCSJ model. The current is described by the equation:

$$I = I_c sin\varphi + \frac{\hbar}{2eR}\frac{d\varphi}{dt} + \frac{\hbar C}{2e}\frac{d^2\varphi}{dt^2} \tag{B.1}$$

By defining the plasma frequency of the junction $\omega_p = \sqrt{2eI_c/\hbar C}$, $\tau = \omega_p t$ and the quality factor $Q = \omega_p RC$, we get:

$$\frac{I}{Ic} = sin\varphi + \frac{1}{Q}\frac{d\varphi}{d\tau} + \frac{d^2\varphi}{d\tau^2} \tag{B.2}$$

We turn this differential equation into a finite difference equation ($d\tau \to \Delta\tau$) in order to solve it numerically.

$$\varphi_{n+1} = (\frac{I}{Ic} - sin\varphi_n)\Delta\tau^2 - \frac{1}{Q}(\varphi_n - \varphi_{n-1})\Delta\tau + 2\varphi_n - \varphi_{n-1} \tag{B.3}$$

The initial φ_0 and φ_1 are defined arbitrary. A certain number of iterations are calculated, then the DC voltage is determined with:

$$V = \frac{\hbar}{2e}\left\langle \frac{d\varphi}{dt} \right\rangle = \frac{\hbar\omega_p}{2e}\left\langle \frac{\varphi_n - \varphi_{n-1}}{\Delta\tau} \right\rangle \tag{B.4}$$

The current is then set to the next value. To observe the hysteresis, the phases must not be reset.

```
#include <iostream>
#include <fstream>
#include <cmath>

using namespace std;

int main()
```

```
{
        // Physical constants
    double e=1.602176565E-19;
    double hb=1.054571726E-34;

        // Constants of the junction
        double R=200;
    double C=3E-13;
    double Ic=400E-9;

    double wp=sqrt(2*e*Ic/(hb*C));
    double Q=wp*R*C;

        // Maximum current considered
        double Imax =2000E-9;

        // Number of iterations for each current
        int nmax=1E6;
        // Last iterations considered to calculate the voltage
        int nlast=nmax/10;
        // Value of the delta steps
        double delta = 0.001;

        double I;
        double Itab[4000];
        int x;
    for (x=0;x<1000;x++)
    {
        Itab[x]=-Imax+x*Imax/500;
    }
    for (x=1000;x<2000;x++)
    {
        Itab[x]=Imax-(x-1000)*Imax/500;
    }

    ofstream file("RCSJ.dat", ios::out | ios::trunc);

    if(file)
    {
                double Inorm;

        long double total;
        int ntotal;
```

```
int ntemp=0;

long double phynm1=0;
long double phyn=0;
long double phynp1=0;

long double average;
long double voltage;

cout << "#Ic␣:␣" << Ic << endl;
cout << "#R␣:␣" << R << endl;
cout << "#C␣:␣" << C << endl;
cout << "#Q␣:␣" << Q << endl;
cout << "#wp␣:␣" << wp << endl;
cout << "#delta␣:␣" << delta << endl;

file << "Current(A)␣Voltage(V)" << endl;

for (x=0;x<2000;x++)
{
    I=Itab[x];
    total=0;
    ntotal=0;
    Inorm=I/Ic;
    average=0;

    for (double ij =0;ij<nmax;ij++)
    {
        phynm1=phyn;
        phyn=phynp1;
        phynp1=(Inorm-sin(phyn))*delta*delta-(1/Q)*(
           phyn-phynm1)*delta+2*phyn-phynm1;

        if (ij>nmax-nlast)
        {
            average=(average*ntotal+(phyn-phynm1)/(
               delta))/(ntotal+1);
            ntotal++;
        }
    }

          voltage = wp*average*hb/(2*e);
          file << I << "␣" << voltage << endl;
```

```
        }

        file << "#Ic␣:␣" << Ic << endl;
        file << "#R␣:␣" << R << endl;
        file << "#C␣:␣" << C << endl;
        file << "#Q␣:␣" << Q << endl;
        file << "#wp␣:␣" << wp << endl;
        file << "#delta␣:␣" << delta << endl;
    }
    file.close();
    return 0;
}
```

Acknowledgements

Here I would like to thank all the persons who supported me during my PhD and made the completion of this work possible.

I would like to thank particularly Prof. Dr. Hilbert von Löhneysen for giving me the opportunity to work on this project. I would like to thank as well Prof. Dr. Wulf Wulfhekel for his work as a secondary referee.

I owe my deepest gratitude to my advisor Dr. Romain Danneau for all that I learned and his guidance during these years.

I am very grateful to Detlef Beckman, Florian Hübler and Michael Wolf for their help with our first measurements at cryogenic temperatures, and to Lars Petzold for the realisation of numerous PCBs.

I would like to thank my colleagues Christian Benz, Jens Mohrmann, Renjun Du, Joachim Schönle, Julian Winter and Fan Wu for their support and help. I would like to salute as well all the former members of the team and all the INT members I've been in touch with.

Finally, I would like to thank my family and my friends for their encouragements and support.

Bibliography

[1] K. S. Novoselov, A. K. Geim, S. V. Morozov, Y. Zhang D. Jiang, S. V. Dubonos, I. V. Grigorieva, and A. A. Firsov. Electric field effect in atomically thin carbon films. *Science*, 307:666–669, 2004.

[2] K. S. Novoselov, A. K. Geim, S. V. Morozov, D. Jiang, M. I. Katsnelson, I. V. Grigorieva, S. V. Dubonos, and A. A. Firsov. Two-dimensional gas of massless Dirac fermions in graphene. *Nature*, 438:197–200, 2005.

[3] Y. Zhang, Y. W. Tan, H. L. Stormer, and P. Kim. Experimental observation of the quantum Hall effect and Berry's phase in graphene. *Nature*, 438:201–204, 2005.

[4] K. Geim and K. S. Novoselov. The rise of graphene. *Nature Materials*, 6:183 – 191, 2007.

[5] A. H. Castro Neto, F. Guinea, N. M. R. Peres, K. S. Novoselov, and A. K. Geim. The electronic properties of graphene. *Review of Modern Physics*, 81:109, 2009.

[6] M. I. Katsnelson. *Graphene - Carbon in Two Dimensions*. Cambridge University Press, 2012.

[7] P. R. Wallace. The band theory of graphite. *Physical Review*, 71:622, 1947.

[8] G. W. Semenoff. Condensed-matter simulation of a three-dimensional anomaly. *Physical Review Letters*, 53:2449–2452, 1984.

[9] S. D. Sarma. Electronic transport in two-dimensional graphene. *Review of Modern Physics*, 83:407–470, 2011.

[10] E. H. Hwang and S. Das Sarma. Single-particle relaxation time versus transport scattering time in a two-dimensional graphene layer. *Physical Review B*, 77:195412, 2008.

[11] P. M. Ostrovsky, I. V. Gornyi, and A. D. Mirlin. Electron transport in disordered graphene. *Physical Review B*, 74:235443, 2006.

[12] J. Tworzydło, B. Trauzettel, M. Titov, A. Rycerz, and C. W. J. Beenakker. Sub-poissonian shot noise in graphene. *Physical Review Letters*, 96:246802, 2006.

[13] M. I. Katsnelson. Zitterbewegung, chirality, and minimal conductivity in graphene. *The European Physical Journal B*, 51:157–160, 2006.

[14] E. McCann. Asymmetry gap in the electronic band structure of bilayer graphene. *Physical Review B*, 74:161403, 2006.

[15] H. Min, B. Sahu, S. K. Banerjee, and A. H. MacDonald. Ab initio theory of gate induced gaps in graphene bilayers. *Physical Review B*, 75:155115, 2007.

[16] S. M. Choi, S. H. Jhi, and Y. W. Son. Controlling energy gap of bilayer graphene by strain. *Nano Letters*, 10:3486–3489, 2010.

[17] M. Mucha-Kruczyński, I. L. Aleiner, and V. I. Fal'ko. Strained bilayer graphene: Band structure topology and landau level spectrum. *Physical Review B*, 84:041404, 2011.

[18] B. Verberck, B. Partoens, F. M. Peeters, and B. Trauzettel. Strain-induced band gaps in bilayer graphene. *Physical Review B*, 85:125403, 2012.

[19] J. B. Oostinga, H. B. Heersche, X. Liu, A. F. Morpurgo, and L. M. K. Vandersypen. Gate-induced insulating state in bilayer graphene devices. *Nature Materials*, 7:151–157, 2007.

[20] T. Taychatanapat and P. Jarillo-Herrero. Electronic transport in dual-gated bilayer graphene at large displacement fields. *Physical Review Letters*, 105:166601, 2010.

[21] Y. Zhang, T. T. Tang, C. Girit, Z. Hao, M. C. Martin, A. Zettl, M. F. Crommie, Y. R. Shen, and F. Wang. Direct observation of a widely tunable bandgap in bilayer graphene. *Nature*, 459:820–823, 2009.

[22] R. T. Weitz, M. T. Allen, B. E. Feldman, J. Martin, and A. Yacoby. Broken-symmetry states in doubly gated suspended bilayer graphene. *Science*, 330:812, 2010.

[23] J. Velasco Jr, L. Jing, W. Bao, Y. Lee, P. Kratz, V. Aji, M. Bockrath, C. N. Lau, C. Varma, R. Stillwell, D. Smirnov, Fan Zhang, J. Jung, and A. H. MacDonald. Transport spectroscopy of symmetry-broken insulating states in bilayer graphene. *Nature Nanotechnology*, 7:156–160, 2012.

[24] B. D. Josephson. Possible new effects in superconductive tunnelling. *Physics Letters*, 1:251, 1962.

[25] N. B. Kopnin. Theory of superconductivity (lecture). 2010.

[26] S. Shapiro. Josephson currents in superconducting tunneling: The effect of microwaves and other observations. *Physical Review Letters*, 11:80, 1963.

[27] M. Tinkham. *Introduction to Superconductivity.* Dover Publications, 2004.

[28] V. Ambegaokar and A. Baratoff. Tunneling between superconductors. *Physics Review Letters*, 10:486, 1963.

[29] K. K. Likharev. Superconducting weak links. *Reviews of Modern Physics*, 51:101–159, 1979.

[30] A. F. Andreev. Thermal conductivity of the intermediate state of superconductors. *Soviet Physics JETP*, 19:1228, 1964.

[31] T.M. Klapwijk, G.E. Blonder, and M. Tinkham. Explanation of subharmonic energy gap structure in superconducting contacts. *Physica 109 and 110B*, 97:1657–1664, 1982.

[32] M. Octavio, M. Tinkham, G.E. Blonder, and T.M. Klapwijk. Subharmonic energy-gap structure in superconducting constrictions. *Physical Review B*, 27:6739, 1983.

[33] M. Octavio, W.J. Skocpol, and M. Tinkham. Improved performance of tin variable-thickness superconducting microbridges. *IEEE Transactions on Magnetics*, 13:739–742, 1977.

[34] C. Visani, Z. Sefrioui, J. Tornos, C. Leon, J. Briatico, M. Bibes, A. Barthélémy, J. Santamaría, and Javier E. Villegas. Equal-spin Andreev reflection and long-range coherent transport in high-temperature superconductor/half-metallic ferromagnet junctions. *Nature Physics*, 8:539–543, 2012.

[35] J. M. Rowell and W. L. McMillan. Electron interference in a normal metal induced by superconducting contracts. *Physical Review Letters*, 16:453–456, 1966.

[36] W. J. Tomasch. Geometrical resonance in the tunneling characteristics of superconducting pb. *Physical Review Letters*, 15:672–675, 1965.

[37] W. L. McMillan and P. W. Anderson. Theory of geometrical resonances in the tunneling characteristics of thick films of superconductors. *Physical Review Letters*, 16:85–87, 1966.

[38] M. Titov and C. W. J. Beenakker. Josephson effect in ballistic graphene. *Physical Review B*, 74:041401, 2006.

[39] E. Sarvestani and S. A. Jafari. Josephson supercurrent in a graphene-superconductor junction. *Physical Review B*, 85:024513, 2012.

[40] C. W. J. Beenakker. Specular Andreev reflection in graphene. *Physical Review Letters*, 97:067007, 2006.

[41] C. W. J. Beenakker. Colloquium: Andreev reflection and Klein tunneling in graphene. *Review of Modern Physics*, 80:1337–1354, 2008.

[42] J. C. Cuevas and A. Levy Yeyati. Subharmonic gap structure in short ballistic graphene junctions. *Physical Review B*, 74:180501, 2006.

[43] H. B. Heersche, P. Jarillo-Herrero, J. B. Oostinga, L. M. K. Vandersypen, and A. F. Morpurgo. Bipolar supercurrent in graphene. *Nature*, 446:56–59, 2007.

[44] F. Miao, S. Wijeratne, Y. Zhang, U. C. Coskun, W. Bao, and C. N. Lau. Phase-coherent transport in graphene quantum billiards. *Science*, 317:1530–1533, 2007.

[45] Xu Du, Ivan Skachko, and Eva Y. Andrei. Josephson current and multiple Andreev reflections in graphene SNS junctions. *Physical Review B*, 77:184507, 2008.

[46] F. Miao, W. Bao, H. Zhang, and C. N. Lau. Premature switching in graphene Josephson transistors. *Solid State Communications*, 140:1046–1049, 2008.

[47] J. H. Choi, H. J. Lee, and Y. J. Doh. Above-gap conductance anomaly studied in superconductor-graphene-superconductor Josephson junctions. *Journal of the Korean Physical Society*, 59:149, 2011.

[48] C. M. Ojeda-Aristizàbal, M. Ferrier, and H. Bouchiat S. Guéron. Tuning the proximity effect in a superconductor-graphene-superconductor junction. *Physical Review B*, 79:165436, 2009.

[49] D. Jeong, J. H. Choi, G. H. Lee, S. Jo, Y. J. Doh, and H. J. Lee. Observation of supercurrent in pbin-graphene-pbin Josephson junction. *Physical Review B*, 83:094503, 2011.

[50] I. V. Borzenets, U. C. Coskun, S. J. Jones, and G. Finkelstein. Phase diffusion in graphene-based Josephson junctions. *Physical Review Letters*, 107:137005, 2011.

[51] J. Voutilainen, A. Fay, P. Häkkinen, J. K. Viljas, T. T. Heikkilä, and P. J. Hakonen. Energy relaxation in graphene and its measurement with supercurrent. *Physical Review B*, 84:045419, 2011.

[52] U. C. Coskun, M. Brenner, T. Hymel, V. Vakaryuk, A. Levchenko, and A. Bezryadin. Distribution of supercurrent switching in graphene under the proximity effect. *Physical Review Letters*, 108:097003, 2012.

[53] K. Komatsu, C. Li, S. Autier-Laurent, H. Bouchiat, and S. Guéron. Superconducting proximity effect in long superconductor/graphene/superconductor junctions: From specular Andreev reflection at zero field to the quantum Hall regime. *Physical Review B*, 86:115412, 2012.

[54] P. Rickhaus, M. Weiss, L. Marot, and C. Schönenberger. Quantum Hall effect in graphene with superconducting electrodes. *Nano Letters*, 12:1942, 2012.

[55] J. H. Choi, G. H. Lee, S. Park, D. Jeong, J.-O. Lee, H.-S. Sim, Y-J Doh, and H-J Lee. Complete gate control of supercurrent in graphene p–n junctions. *Nature Communications*, 4:2525, 2013.

[56] N. Mizuno, B. Nielsen, and X. Du. Ballistic-like supercurrent in suspended graphene Josephson weak links. *Nature Communications*, 4:2716, 2013.

[57] P. Blake, E. W. Hill, A. H. Castro Neto, K. S. Novoselov, D. Jiang, R. Yang, T. J. Booth, and A. K. Geim. Making graphene visible. *Applied Physics Letters*, 91:063124, 2007.

[58] A. C. Ferrari, J. C. Meyer, V. Scardaci, C. Casiraghi, M. Lazzeri, F. Mauri, S. Piscanec, D. Jiang, K. S. Novoselov, S. Roth, and A. K. Geim. Raman spectrum of graphene and graphene layers. *Physical Review Letters*, 97:187401, 2006.

[59] L. M. Malard, M. A. Pimenta, G. Dresselhaus, and M. S. Dresselhaus. Raman spectroscopy in graphene. *Physics Reports*, 473:51–87, 2009.

[60] C. R. Dean, A. F. Young, I. Meric, C. Lee, L. Wang, S. Sorgenfrei, K. Watanabe, T. Taniguchi, P. Kim, K. L. Shepard, and J. Hone. Boron nitride substrates for high-quality graphene electronics. *Nature Nanotechnology*, 5:722–726, 2010.

[61] J. H. Chen, C. Jang, S. Xiao, M. Ishigami, and M. S. Fuhrer. Intrinsic and extrinsic performance limits of graphene devices on sio2. *Nature Nanotechnology*, 3:206–209, 2008.

[62] R. Decker, Y. Wang, V. W. Brar, W. Regan, H. Z. Tsai, Q. Wu, W. Gannett, A. Zettl, and M. F. Crommie. Local electronic properties of graphene on a bn substrate via scanning tunneling microscopy. *Nano Letters*, 11(6), 2011.

[63] G. Giovannetti, P. A. Khomyakov, G. Brocks, P. J. Kelly, and J. v.d. Brink. Substrate-induced band gap in graphene on hexagonal boron nitride: Ab initio density functional calculations. *Physical Review B*, 76:073103, 2007.

[64] S. Kim, J. Nah, I. Jo, D. Shahrjerdi, L. Colombo, Z. Yao, E. Tutuc, and S. K. Banerjee. Realization of a high mobility dual-gated graphene field-effect transistor with al2o3 dielectric. *Applied Physics Letters*, 94:062107, 2009.

[65] A. B. Zorin. The thermocoax cable as the microwave frequency filter for single electron circuits. *Review of Scientific Instruments*, 66:4296, 1995.

[66] L. Spietz, J. Teufel, and R. J. Schoelkopf. A twisted pair cryogenic filter. *Arxiv*, cond-mat/0601316, 2006.

[67] W. Song, M. Rehman, Y. Chong, and S. W. Ryu. Transmission properties of cryogenic twisted pair filters. *Journal of the Korean Physical Society*, 57:1490–1493, 2010.

[68] J. M. Martinis, M. H. Devoret, and J. Clarke. Experimental tests for the quantum behavior of a macroscopic degree of freedom: The phase difference across a Josephson junction. *Physical Review B*, 35:4682–4698, 1987.

[69] D. Vion, P. F. Orfila, P. Joyez, D. Esteve, and M. H. Devoret. Miniature electrical filters for single electron devices. *Journal of Applied Physics*, 77:2519, 1995.

[70] H. le Sueur and P. Joyez. Microfabricated electromagnetic filters for millikelvin experiments. *Review of Scientific Instruments*, 77:115102, 2006.

[71] K. Bladh, D. Gunnarsson, E. Hürfeld, S. Devi, C. Kristoffersson, B. Smålander, S. Pehrson, T. Claeson, P. Delsing, and M. Taslakov. Comparison of cryogenic filters for use in single electronics experiments. *Review of Scientific Instruments*, 74:1323, 2003.

[72] F. P. Milliken, J. R Rozen, G. A. Keefe, and R. H. Koch. 50 ohms characteristic impedance low-pass metal powder filters. *Review of Scientific Instruments*, 78:024701, 2007.

[73] A. Fukushima, A. Sato, A. Iwasa, Y. Nakamura, T. Komatsuzaki, and Y. Sakamoto. Attenuation of microwave filters for single-electron tunneling experiments. *IEEE Transactions on Instrumentation and Measurement*, 46:289, 1997.

[74] W A. Lukashenko and A. V. Ustinov. Improved powder filters for qubit measurements. *Review of Scientific Instruments*, 79:014701, 2008.

[75] F. Mueller, R. N. Schouten, M. Brauns, T. Gang, W. H. Lim, N. S. Lai, A. S. Dzurak, W. G. van der Wiel, and F. A. Zwanenburg. Printed circuit board metal powder filters for low electron temperatures. *Review of Scientific Instruments*, 84:044706, 2013.

[76] T. Ludwig. Andreev reflection in bilayer graphene. *Physical Review B*, 75:195322, 2007.

[77] W. A. Muñoz, L. Covaci, and F. M. Peeters. Tight-binding study of bilayer graphene Josephson junctions. *Physical Review B*, 86:184505, 2012.

[78] Y. Takane and K. I. Imura. Josephson current through a planar junction of graphene. *Journal of the Physical Society of Japan*, 80:043702, 2011.

[79] Y. Takane and K. I. Imura. Quasiclassical theory of the Josephson effect in ballistic graphene junctions. *Journal of the Physical Society of Japan*, 81:094707, 2012.

[80] A. K. Geim and I. V. Grigorieva. Van der waals heterostructures. *Nature*, 499:419–425, 2013.

[81] B. Huard, N. Stander, J. A. Sulpizio, and D. Goldhaber-Gordon. Asymmetry gap in the electronic band structure of bilayer graphene. *Physical Review B*, 78:121402, 2008.

[82] M. Popinciuc, V. E. Calado, X. L. Liu, A. R. Akhmerov, T. M. Klapwijk, and L. M. K. Vandersypen. Zero-bias conductance peak and Josephson effect in graphene-nbtin junctions. 2012.

[83] Renato Borges Pontes José Eduardo Padilha and Adalberto Fazzio. Bilayer graphene on h-bn substrate: investigating the breakdown voltage and tuning the bandgap by electric field. *Journal of Physics: Condensed Matter*, 24:075301, 2012.

[84] F. Zhang, H. Min, M. Polini, and A. H. MacDonald. Spontaneous inversion symmetry breaking in graphene bilayers. *Physical Review B*, 81:041402, 2010.

[85] F. Zhang, J. Jung, G. A. Fiete, Q. N., and A. H. MacDonald. Spontaneous quantum Hall states in chirally stacked few-layer graphene systems. *Physical Review Letters*, 106:156801, 2011.

[86] F. Freitag, J. Trbovic, M. Weiss, and C. Schönenberger. Spontaneously gapped ground state in suspended bilayer graphene. *Physical Review Letters*, 108:076602, 2012.

[87] W. Baoa, J. Velasco, F. Zhangc, L. Jinga, B. Standleye, D. Smirnovf, M. Bockratha, A. H. MacDonaldc, and C. N. Laua. Evidence for a spontaneous gapped state in ultraclean bilayer graphene. *Proceedings of the National Academy of Sciences*, 109:10802–10805, 2012.

[88] A. Veligura, H. J. van Elferen, N. Tombros, J. C. Maan, U. Zeitler, and B. J. van Wees. Transport gap in suspended bilayer graphene at zero magnetic field. *Physical Review B*, 85:155412, 2012.

[89] E. McCann and M. Koshino. The electronic properties of bilayer graphene. *Reports on Progress in Physics*, 76:056503, 2013.